THÈSE

Pour obtenir le grade de

DOCTEUR DE L'UNIVERSITÉ GRENOBLE ALPES

École doctorale : PHYS - Physique
Spécialité : Nanophysique
Unité de recherche : Institut Néel

Imagerie de la dynamique des porteurs à l'échelle nanométrique grâce aux interactions lumière-électron-matière

Imaging carrier dynamics at the nanoscale thanks to light- and electron-matter interactions

Présentée par :

Pablo SÁENZ DE SANTA MARÍA MODROÑO

Direction de thèse :

Gwénolé JACOPIN CHARGE DE RECHERCHE HDR, CNRS DELEGATION ALPES	Directeur de thèse

Rapporteurs :

Bertrand BOUDART
PROFESSEUR DES UNIVERSITES, UNIVERSITE DE CAEN NORMANDIE
Bruno MASENELLI
PROFESSEUR DES UNIVERSITES, INSA DE LYON

Thèse soutenue publiquement le **2 décembre 2025**, devant le jury composé de :

Bertrand BOUDART, PROFESSEUR DES UNIVERSITES, UNIVERSITE DE CAEN NORMANDIE	Rapporteur
Bruno MASENELLI, PROFESSEUR DES UNIVERSITES, INSA DE LYON	Rapporteur
Jonas LäHNEMANN, SENIOR SCIENTIST, PAUL-DRUDE INSTITUT FUR FESTKORPERELEKTRONIK (PDI)	Examinateur
Julien PERNOT, PROFESSEUR DES UNIVERSITES, UNIVERSITE GRENOBLE ALPES	Président
Jean-Charles ARNAULT, DIRECTEUR DE RECHERCHE, CEA SACLAY	Examinateur
Amélie DUSSAIGNE, INGENIEURE DOCTEURE, CEA GRENOBLE	Examinatrice

Invités :

Névine ROCHAT
INGENIEURE, CEA Grenoble

Index

1 Introduction **7**

2 Motivation and underlying physics **10**

2.1 Band structure of diamond and nitride semiconductors 10

2.2 Semiconductor devices: A non extensive overview 12

2.2.1 Physical principles of Light-Emitting Diodes 12

2.2.2 High-electron-mobility transistors 15

2.3 Thermal issues at the microscale 15

2.3.1 µLED: Sidewall surface recombination 16

2.3.2 GaN HEMT : Self-heating issue at reduced scales 17

2.4 Temperature sensing at the nanoscale 18

2.4.1 Basics of nanothermometry 19

2.4.2 Nanothermometry state of the art 20

2.4.3 Optically detected magnetic resonance using NV- 21

2.5 Diamond-based cathodoluminescence nanothermometry 22

3 Experimental methods **25**

3.1 Field Emission Scanning Electron Microscope 25

3.2 Cathodoluminescence spectroscopy 27

3.3 Photoluminescence spectroscopy 32

3.4 Hanbury-Brown-Twiss interferometry 34

3.4.1 Beam blanker 36

3.5 Lifetime measurements . . . 37

3.6 Electroluminescence spectroscopy . . . 38

4 Emission Heterogeneity in InGaN/GaN Micro-Light-Emitting Diodes 40

4.1 LED sample structure . . . 41

4.2 LED sample measurements . . . 43

4.2.1 Photoluminescence measurements . . . 43

4.2.2 Spatially resolved CL-HBT measurements . . . 44

4.2.3 Substrate analysis . . . 51

4.2.4 Low temperature measurements . . . 52

4.3 Analysis of LED results . . . 54

4.3.1 Emission spectra and interference pattern . . . 54

4.3.2 V-pits as the source of µLED heterogeneity. . . . 56

4.4 Energy excitation efficiency . . . 61

4.5 Conclusions . . . 63

5 Cathodoluminescence temperature sensing in bulk diamond 65

5.1 Introduction . . . 65

5.2 Bulk diamond sample . . . 66

5.3 Cathodoluminescence spectroscopy results on bulk diamond . . . 67

5.3.1 389 nm peak . . . 68

5.3.2 440 nm radiation peak . . . 70

5.3.3 TR12 peak . . . 70

5.3.4 CVD peaks . . . 70
5.3.5 H4 band . . . 72
5.3.6 533 nm peak . . . 72
5.3.7 SiV peak . . . 73
5.4 The Nitrogen-Vacancy color center in diamond . . . 77
5.5 NV0 peak in bulk diamond . . . 80
5.6 Phonon-assisted exciton peaks . . . 86
5.7 Conclusion . . . 89

6 Nanodiamond cathodoluminescence spectral results for thermal sensing 92

6.1 Nanodiamond structure . . . 92
6.1.1 Physical characterization of nanodiamond samples . . . 92
6.1.2 Surface chemical characterization . . . 94
6.2 Nanodiamond photoluminescence . . . 95
6.2.1 Fluorolog Photoluminescence . . . 95
6.2.2 Simultaneous photoluminescence and cathodoluminescence . . . 98
6.3 Secondary peaks in nanodiamond cathodoluminescence spectra . . . 101
6.3.1 Phonon-assisted exciton peaks . . . 103
6.3.2 389 nm peak . . . 103
6.3.3 A band . . . 104
6.3.4 440 nm radiation peak . . . 104
6.3.5 H3 and H4 band . . . 105
6.4 Nitrogen-Vacancy center cathodoluminescence in nanodiamond . . . 105

6.4.1 Peak fitting in nanodiamond 106

6.4.2 Temperature evolution of NV0 112

6.4.3 Evolution of NV0 lifetime with temperature 117

6.4.4 Effect of ND size on NV0 emission 119

6.4.5 Effect of cluster morphology on NV0 emission 120

6.4.6 Using an InGaN LED substrate to study ND cluster depth 123

6.4.7 Nanodiamond surface chemistry as the source of model deviation 125

6.5 Thermal sensing on LED using nanodiamond 129

6.5.1 Joule heating measured from CL NV0 signal 129

6.5.2 Spatially resolved CL thermal sensing 132

6.5.3 Time resolved CL thermal sensing 135

6.6 Surface UV treatment on ND 138

6.7 Lifetime measurements of different surface chemistries 139

6.8 Conclusion 142

7 Conclusions and perspectives **143**

List of acronyms

Å	Angstrom (10^{-10} meters)
AFM	Atomic Force Microscopy
BOE	Buffered Oxide Etching
CCD	Charge-Coupled Device
CL	Cathodoluminescence
EH	Electron-Hole Pair
EQE	External Quantum Efficiency
EXE	Extraction Efficiency
FESEM	Field Effect Scanning Electron Microscope
FCC	Face Centered Cubic Bravais Lattice.
FWHM	Full Width at Half Maximum
g/mm	Grooves per millimeter
HBT	Hanbury-Brown-Twiss Interferometry
HEMT	High-Electron-Mobility Transistor
HPHT	High Pressure Hight Temperature Diamond
ICP-RIE	Inductively Coupled Plasma Reactive Ion Etching
IQE	Internal Quantum Efficiency
i-GaN	Intrinsic Gallium Nitride
LED	Light-Emitting Diode
MPECVD	Microwave Plasma-Enhanced Chemical Vapor Deposition
ND	Nanodiamond, Nanodiamonds

NOC	Number of counts
NV	Nitrogen-Vacancy Center
NV0	Neutrally Charged Nitrogen-Vacancy Center
NV-	Negatively Charged Nitrogen-Vacancy Center
n-GaN	Negatively Doped Gallium Nitride
ODMR	Optically Detected Magnetic Resonance
PEALD	Plasma Enhanced Atomic Layer Deposition
PL	Photoluminescence
PMT	PhotoMultiplier Tube
p-GaN	Positively Doped Gallium Nitride
p-n	Positive-negative junction
QW	Quantum Well, Quantum Wells
STED	Stimulated Emission-Depletion
STEM	Scanning Transmission Electron Microscopy
TOF-SIMS	Time Of Flight Secondary-Ion Mass Spectrometry
UL	Under Layer
3D	Three Dimensional, Three Dimensions

1 Introduction

The constant advances on the design and fabrication of electronic devices have resulted in progressively smaller designs, as reduced sizes lead to lower electric consumption, a wider range of potential applications, and reduced demand for rare materials. However, as electronic devices become smaller, measuring their core properties with an adequate spatial resolution becomes increasingly more challenging.

In particular, carrier behavior is modified on the smaller electronic devices, as new effects and issues unique to the nanoscale appear. Some of these novel effects will be discussed in chapter 2, alongside a brief discussion of the underlying physics involved in current transport. These unique behaviors represent a challenge to the proper study of small scale electronic devices. Hence, a high spatial resolution on the carrier characterization techniques employed when working with such samples becomes extremely valuable.

As is the case for carrier characterization, proper temperature characterization in micro and nano scaled electronic devices is even more important than in bulk scaled ones, as the smaller channels lead to larger current densities that cause very strong, very localized, Joule heating effects, even if the total current is smaller than in larger devices. This localization leads to extremely sharp temperature gradients during device operation, so in order to properly understand the effects of current and temperature on device performance, a very high spatial resolution is key.

Due to these reasons, our goal with this work is to develop a novel technique that allows for simultaneous carrier dynamics and temperature sensing of electronic devices, such as light-emitting diodes or transistors, with a focus on very high spatial resolution. Measuring device temperature and gradient under operation with an adequate spatial resolution would allow for better understanding of the mechanisms that currently limit performance.

In order to achieve this spatial resolution goal, our method will be based on cathodoluminescence, a measuring technique known for its nanometric applications. Cathodoluminescence is the study of photons emitted from a sample under electron bombardment. Despite the technique being based on the characterization of a light signal, cathodoluminescence itself is not diffraction limited, leading to a much higher potential spatial resolution than purely optical methods.

Cathodoluminescence and its general properties will be discussed in more detail in chapter 3, alongside the other experimental methods employed during this PhD.

Cathodoluminescence as a technique is already used to achieve carrier characterization in electronic devices, as will be shown in detail during chapter 4. In said chapter, we will show how the usage of this technique enabled us to study a microLED that displayed a strong local heterogeneity in brightness. Cathodoluminescence not only was able to detect this localized heterogeneity, but thanks to the high spatial resolution it gave us the tools to actually understand its origin. This in short led to novel results that became a published article [1].

Hence, our main innovation in this work will be to develop a thermal sensing method based on cathodoluminescence that can be performed simultaneously to standard characterization. In order to reach this objective, we will use the luminescence properties of nano-diamond. Diamond is one of the best thermal conductors in existence, causing any deposited nano-diamonds on top of sample to quickly thermalize to near the same temperature as the material they are in contact with. Diamond is also know for a very high stability, which is important when performing cathodoluminescence, as the electron bombardment can cause damage in more delicate materials.

Apart from these obvious advantages, diamond was chosen for thermal sensing due to a series of peaks present in its emission spectra that are know to be temperature dependent, in particular a series of peaks associated to nitrogen defects. Those peaks will be discussed in detail in chapter 5.

The particular sample chosen was a commercially available Sigma-Aldrich fluorescent nitrogen-doped nanodiamond powder. The sample, the results of its characterization, and the development of a thermal sensor based on it will be discussed in chapter 6, the final and most extensive chapter of this work. Said chapter will show the current limitations of our current approach, as well as the advances achieved in the goal of thermal and carrier sensing. We demonstrated the potential of this sample for thermal sensing in a second article [2], and this chapter will expand these results showing real temperature measurements on an electronic device, a LED in operation.

Nanodiamonds were chosen over larger samples due the large thermal conductivity of the

material, which causes each diamond sample to present a homogeneous temperature. Hence the nanodiamond size is the first factor to consider in order to achieve high spatial resolution.

As cathodoluminescence is based on irradiation from an electron beam, there exists another factor limiting the spatial resolution: The beam interaction volume, which as will be discussed in chapter 3 has a minimum lateral size of 14 nm. Meanwhile, the individual nanodiamond size, can go below even 10 nm, as will be discussed in chapter 6. Hence, we can consider the former to be the limiting factor for the spatial resolution of our method.

Nanodiamond size was studied by our collaborators from Universite-Paris Saclay: Hugues A. Girard and Jean-Charles Arnault, who performed physical and chemical characterization of the nanodiamonds, and provided their expertise in size-shorting, making their support invaluable for the development of this PhD.

The chemical characterization of the nanodiamond surface in particular turned out to be extremely relevant for our work, as will be shown in chapter 6. We observed that the emission properties of the nitrogen defects of the nanodiamond samples were very sensitive to both the size of the nanodiamond and its surface chemistry. This was an unexpected result, as nitrogen defects in diamond are known to cause a strong localization of carriers, meaning that the emission of these defects should not be affected by changes in the diamond surface.

However, we have found strong compelling evidence that the emission properties of the nanodiamond Nitrogen defects were in fact conditioned by the chemical properties of the surface. This supposes a setback when studying different samples, as nanodiamond deposited on different surfaces see their chemical properties altered and therefore the emission properties of the associated defect. This evidence will also be shown in chapter 6, alongside the techniques we used to mitigate this issue and still achieve thermal sensing using the nanodiamond cathodoluminescence signal.

2 Motivation and underlying physics

2.1 Band structure of diamond and nitride semiconductors

The types of samples that were the focus of our study during the development of this PhD were either diamonds or gallium-nitride based LEDs. Both of these samples are crystalline solid semiconductors, so it becomes necessary to introduce some basic properties of this type of material.

Crystalline solids are defined as materials whose atoms are organized according to the repeating structure of a Bravais lattice, usually denoted as Λ. From this structure, it can be demonstrated that all crystalline solids follow Bloch's Theorem [3], which dictates the core properties of their energy states. The theorem states that "solutions to the Schrödinger equation in a periodic potential take the form of a plane wave modulated by a periodic function", *i.e.*

$$\psi_{\mathbf{k}}(\mathbf{x}) = e^{i\mathbf{k}\cdot\mathbf{x}} u_{\mathbf{k}}(\mathbf{x}) \tag{1}$$

Where $\mathbf{k}$ is the crystal momentum, $\mathbf{x}$ the spatial coordinates, i the imaginary unit, and $u_{\mathbf{k}}(\mathbf{x})$ a function with the same periodicity as the Bravais lattice: $u_{\mathbf{k}}(\mathbf{x}+\mathbf{r}) = u_{\mathbf{k}}(\mathbf{x}) \quad \forall \mathbf{r} \in \Lambda$.

The Bloch theorem proves that the energy distribution of electrons in a Bravais lattice is closely related to their crystal momentum $\mathbf{k}$. This momentum exists in the reciprocal space, which for the case of a Bravais lattice is called a reciprocal lattice, the Fourier transform of the original lattice [4]. For a given Bravais lattice with vector base $\{\vec{a_i}\}$, its associated reciprocal lattice is the Bravais lattice whose vector base is $\{\vec{b_i}\}$, defined as being the unique vector base following:

$$\vec{a_i} \cdot \vec{b_j} = 2\pi\delta_{ij} \qquad \text{for all } i, j \tag{2}$$

where δ_{ij} represents a Kronecker delta.

The need for this reciprocal lattice arises due to a lack of uniqueness in the Bloch theorem: if we take the expression for $\psi_{\mathbf{k}}$ given in equation (1), and we take $\mathbf{q}$ a vector of the reciprocal lattice associated to the potential, we have:

$$\psi_{\mathbf{k}+\mathbf{q}}(\mathbf{x}) = e^{j\mathbf{k}\cdot\mathbf{x}} e^{j\mathbf{q}\cdot\mathbf{x}} u_{\mathbf{k}}(\mathbf{x}) = e^{j\mathbf{k}\cdot\mathbf{x}} u'_{\mathbf{k}}(\mathbf{x}), \quad \text{with } u'_{\mathbf{k}}(\mathbf{x}) = e^{j\mathbf{q}\cdot\mathbf{x}} u_{\mathbf{k}}(\mathbf{x}) \tag{3}$$

In this case $u'_{\mathbf{k}}(\mathbf{x})$ has the same periodicity as $u_{\mathbf{k}}(\mathbf{x})$ meaning that two states whose crystal momenta differs by a reciprocal vector can only be differentiated by their associated periodic function, which can not be readily accessed.

To avoid this issue, the crystal momentum is replaced by the reduced crystal momentum. This new magnitude is obtained by translating the original crystal momentum $\mathbf{k}$ by a reciprocal lattice vector $\mathbf{q}$ so $\mathbf{k}+\mathbf{q}$ is within the Wigner-Seitz cell of the reciprocal lattice, also known as the first Brillouin zone.

Reduced crystal momentum is normally used interchangeably with crystal momentum, and they are both normally referred with the same notation $\mathbf{k}$, despite the subtle differences between the two. The main consideration when using reduced crystal momentum is that states with the same $\mathbf{k}$ can have different electron energy. However, since the states are discrete, they can be sorted according to energy, and identified with two values: $\psi_{\mathbf{k},n}$ with $\mathbf{k}$ crystal momentum and n the energy position, with $n = 0$ the lowest energy state.

These state energies form what is called the band structure of the crystalline material. These bands are distributed in the entire 3-dimensional structure of the first Brillouin zone, but it is common to represent the energies alongside various 1-dimensional paths. As an example, figure 2 shows the diamond band structure.

These paths are defined by specific points in the Brillouin zone, which, thanks to their particular symmetry, usually lead to regime changes or critical points in the behavior of the energy bands. These points have standardized names given by crystallographic convention. For example, the Γ point is the origin of the reciprocal lattice.

Both of the materials studied during this PhD are semiconductors. In a semiconductor, the energy band structure has some energy regions with no associated energy states. These regions are called the band-gap of a semiconductor, and the energy states with higher and lower energy are called the conduction and valence bands respectively.

In order for the conductivity to be possible, either band must be partially filled. In a semiconductor, the Fermi level is within the bandgap, but by doping the material or applying a

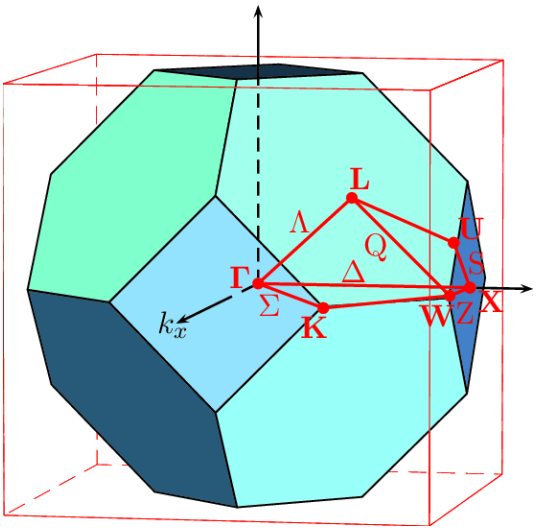


Figure 1: Structure of the Brillouin zone for an FCC lattice, and the labels of the different points in it, according to crystallographic convention. Source: [5].

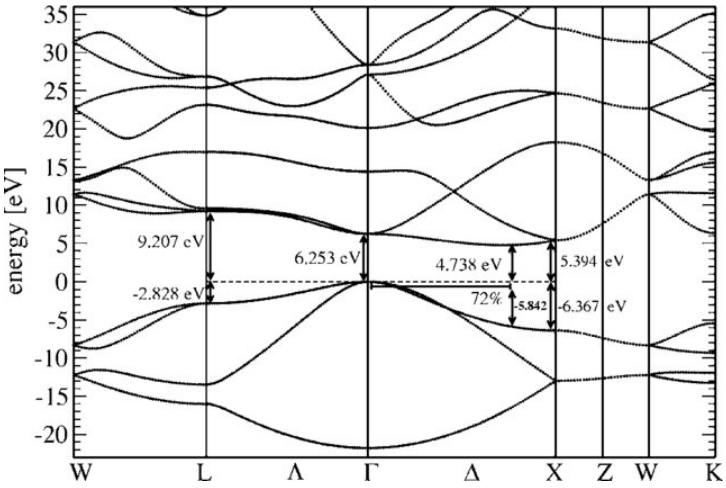


Figure 2: Band structure for diamond. The different lines represent the energies of different electrons as their crystal momentum traverses the Brillouin zone through different paths, represented in figure 1. Source: [6].

voltage, the Fermi level can be shifted closer to the conduction or valence bands. If the level is raised into the conduction band, the states of this band will be partially filled, and if the level is lowered into the valence band, the band levels will be partially filled with holes. In either case, the behavior of the material will switch from insulator to conductor.

2.2 Semiconductor devices: A non extensive overview

The unique properties of semiconductor materials enable the fabrication of a wide array of devices. Hence, a full review of all their potential applications would be out of the scope of this work. Nevertheless, we will give a short overview of some of these devices.

2.2.1 Physical principles of Light-Emitting Diodes

A Light-Emitting Diode, or LED, is, as the name indicates, a type of semiconductor device that only allows current to flow in one direction, and that produces light whenever current is flowing.

A LED has a positively (p) doped side and a negatively (n) doped side, forming a p-n junction,

leading to the diode behavior. Usually, between these two sides, one or several quantum wells (QW) are inserted. The QWs are a thin region, normally not more than a few nanometers, where the chemical composition of the material is changed in a way that leads to a narrowing of the bandgap.

Due to this lower bandgap, the QW will cause free carriers from both the p and n sides of the junction to accumulate inside it. The large presence of electrons and holes enhances radiative recombination, causing the emission of photons with the same energy as the energy difference of the confined hole and electron states in the QW.

In our particular case, the LEDs used where composed of group III metal elements (Al, Ga and In) and nitrogen atoms a group V element, in a 50/50 ratio between group III and V elements. These materials have two possible crystal structures, Zinc blende and wurtzite, but all the LEDs studied during this PhD were wurtzite structures, which is more common as it is the more energetically efficient ordering. The wurtzite phase follows a 3 dimensional hexagonal Bravais lattice with two atoms per unit cell, the III group element and nitrogen.

The QW of all of the LED studied in this PhD had a mixture of In and Ga for the group V element. As the bulk structure of the LEDs was GaN, the presence of indium in the QW lead to the desired reduction in bandgap, since wurtzite InN has a band gap of around 0.6 eV [7] versus the much larger 3.4 eV bandgap of wurtzite GaN [8].

Nitrides are often chosen for LED applications because they possess a direct band gap. As discussed in section 2.1, the bandgap is the region of energies with no associated states. The value of the bandgap is the difference between the highest energy state of the valence band and the lowest energy state of the conduction band. Carriers will concentrate on those extremes, as they are the most energetically efficient. Since these states exist in the 3-dimensional structure of the Brillouin zone, they both have an associated crystal momentum $\mathbf{k}$, which must be conserved in transitions. In direct bandgap materials the extremes of the valence and conduction band have the same $\mathbf{k}$, so e-h pairs can recombine very efficiently. In materials where this is not the case, recombination is still possible, but with lower efficiency, as will be discussed in chapter 5.

Under normal operation, the injection of electrons and holes is achieved by connecting the LED

to a circuit and flowing a current through it. However during the development of this PhD, we also used both cathodoluminescence and photoluminescence spectroscopy techniques to produce e-h pairs inside our LED samples in order to investigate the optical properties of the LED. These techniques will be introduced in chapter 3.

Two of the key numbers required to understand LED behavior are the internal quantum efficiency (IQE) and the external quantum efficiency (EQE). By definition, IQE is the fraction of electron-hole pairs that decay into a photon, whereas EQE is the ratio between photons that escape the sample and e-h pairs that have been created.

From these definitions, it is obvious that IQE is larger than EQE. The ratio between the two is the extraction efficiency (EXE), the fraction of photons that escape the sample. The main reason for photons to remain trapped inside the LED is reflection at an interface. Photons that fail to exit the LED structure will likely end reabsorbed as heat, which means a sample with low EXE will require strong cooling to function properly.

Another important magnitude in LEDs is the injection efficiency, the ratio of the number of e-h pairs injected into the LED to the number of e-h pairs supplied by the power source. By multiplying the injection efficiency by the EQE and the energy ratio between injected e-h pairs and emitted photons, we obtain the wall plug efficiency of the LED: The fraction of electrical energy that the LED converts to photon energy.

When studying a LED is important to consider the current regime under which the sample is operating. LEDs have three possible regimes: Low current, peak efficiency, and efficiency droop. The low current regime, as its name indicates, is achieved when the LED current per surface sit below a certain threshold. In the case of blue InGaN LEDs, this value is around 3.5 A / cm^2 [9]. Under the low current regime, efficiency grows with current. This regime has been observed to be more sensitive to sample aging [10].

When operating at higher currents, InGaN LEDs suffer a significant loss in efficiency, an effect referred to as the "efficiency droop regime" [11]. This efficiency droop is caused by Auger recombination, a nonradiative process in which the energy of a e-h recombination is absorbed by another carrier, either an electron or a hole [12]. High current also causes a blue-shift due to

the increased screening of polarization fields caused by the extra carriers. The screening causes the bandgap to broaden, and it is especially strong on thin quantum wells [13] such as those in our sample.

Between these two regimes, we have the peak efficiency regime, which is simply the maximum of efficiency with current for a given LED.

2.2.2 High-electron-mobility transistors

As the name suggests, high-electron-mobility transistors, or HEMTs, are a type of transistors designed specially for high-power applications. A transistor is a semiconductor electronic device that enables or disables current transport between a source and a drain based on the voltage applied to its gate. Transistors are arguably the most important electronic devices for modern applications, and their properties are closely tied to the bandgap of the semiconductors that compose them. In short, this change is conductivity is achieved by using the gate voltage to shift the Fermi level of the semiconductor, which as discussed in section 2.1, activates electronic states in the conduction band enabling current transport.

HEMTs in particular are transistors developed for situations in which large currents and voltages are involved. As such, these devices are designed to maximize electron mobility even in those extreme circumstances. Gallium Nitride is a good fit for HEMTs due to its wide bandgap, high critical breakdown electric field, high thermal conductivity, and high electronic saturation velocity. These characteristics enable the fabrication of HEMTs with high stability and performance. For these reasons, GaN dominates the market for HEMTs operating in the voltage range of 100 V to 1200 V [14].

2.3 Thermal issues at the microscale

Reducing the scale of electronic devices is far from a recent goal in both industry and research, as there is a long list of reasons that cause the strong demand in smaller and smaller semiconductor devices. Apart from the obvious savings in rare and expensive elements, smaller devices have

lower power consumption, and enable further applications. For example, micrometric III/V LEDs could replace OLEDs in phone screens, as their maximum potential efficiency is higher, and even enable new applications that demand higher resolution, such as virtual reality headsets.

However, reducing the size of these devices leads to a series of novel issues, which usually include enhanced heating. We will discuss the miniaturization issues that apply to the devices discussed in the previous section.

2.3.1 µLED: Sidewall surface recombination

From the properties of LEDs described in section 2.2.1 it is clear that in order for a device to achieve a good wall plug efficiency, both its IQE and EQE need to be as high as possible. This represents an issue when trying to reduce the scale of the device, as both of these magnitudes are severely affected by the size of the LED. This is quite relevant for our work, since as will be discussed in chapter 4, we worked with micrometric LEDs of multiple sizes and shapes. It has been observed that reducing the size of the µLEDs leads to a loss of EQE, but also to an increase in peak efficiency current density [15]. Both effects are extremely detrimental for commercial applications: The loss of EQE leads to a lower brightness, and the current increase causes higher Joule heating during operation. These two issues compound, as the extra heat can cause an emission wavelength shift and a decrease in EQE by itself.

The two effects have been attributed to sidewall surface recombination [16]. This effect is caused by sidewalls of the LED, which breaks crystal symmetry and creates new states within the bandgap. These surface states enable nonradiative e-h pair recombination, meaning the carrier decay enabled by these states does not produce light, with the energy dissipating as heat instead. As these new states also enable conductivity, they are the cause of the peak efficiency current density increase. Figure 3 a) shows a diagram of these effects.

The impact of the surface is much higher in smaller LEDs, as their surface-to-volume ratio is larger due to the square-cube law. The study of Woo Jin Baek *et al.* [17], shown in figure 3 b), illustrates how decreasing the lateral size of square InGaN LEDs leads to the expected increase in peak efficiency current density and decrease in EQE.

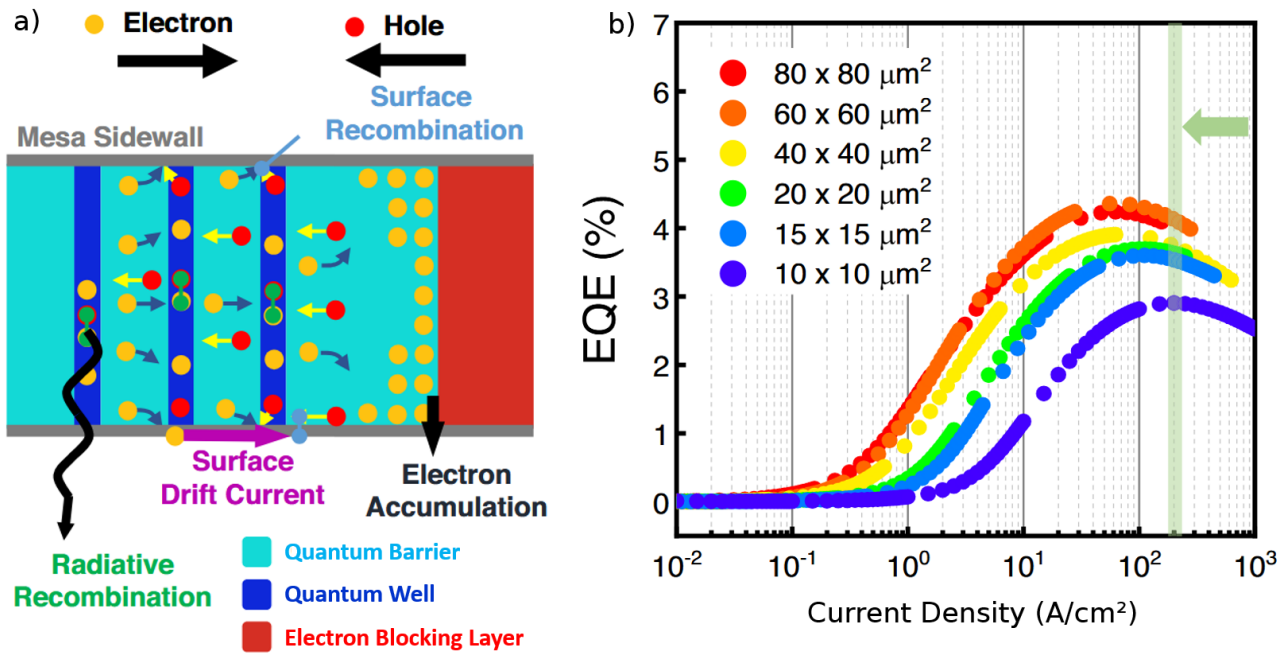


Figure 3: a) Schematic diagram of possible carrier transport processes in µLEDs under normal operation. The electrons drifting or tunneling throughout the active region can diffuse to the sidewall where the surface recombination can occur or drift through the surface leakage path. The drifted or tunneled electrons through the active region can also accumulate at the interface between the active region and the electron blocking layer, where a lateral diffusion can be significant. b) EQE-logarithmic current density curve for square µLEDs with lateral sizes ranging 80 × 80 µm^2 to 10 × 10 µm^2. The green line shows the point where 10 × 10 µm^2 device is at its maximum EQE. Source [17]

The expected extra heating of smaller samples was one of the reasons we chose LEDs for our study, as a larger change in temperature would be easier to measure. Accessing the temperature of LED samples with a high spatial resolution would also help demonstrate the effect of surface recombination, and the different properties of the surface versus the interior of the sample.

2.3.2 GaN HEMT : Self-heating issue at reduced scales

As discussed in section 2.2.2, HEMTs need to work under extreme conditions of current and voltage, which will naturally lead to enhanced Joule heating, making thermal management an important aspect of the design of these devices.

The thermal management aspect of these devices becomes even more critical as their size is

reduced, as GaN HEMT with smaller length scales at higher voltages have been observed lead to excessively high channel temperatures. This harms performance and can have detrimental effects on device reliability [18]. The source of this extra temperature appears to be the extra Joule heating due to the increase in short-channel effects, which occur when the channel length is comparable to that of the depletion regions of the source and drain junctions.

Short channel effects are varied in nature and origin, but in short, all reduce the ability of the transistor gate voltage to control the current flow, which severely hampers the utility of the device. It has been observed that short channel effects can be reduced in GaN HEMT by preserving the aspect ratio between gate length and barrier thickness, but with the caveat that this type of design causes gate leakage current to increase and output current to degrade due to a lower conductivity of electrons [19].

These negative effect of scale reduction are compounded by the fact that self-heating effects are particularly strong in GaN HEMTs because of the dominant polar optical phonon scattering [20]. Furthermore, GaN HEMTs are usually fabricated on top of Si substrates, due to their lower cost and their integrability with Si metal-oxide semiconductor processes [21, 22]. However, due to the low thermal conductivity of Si, self-heating effects are enhanced in these HEMTs, leading to a focus on the study of their heat diffusion [19].

2.4 Temperature sensing at the nanoscale

As has been shown from the previous examples, the process of fabricating micrometric electronic devices leads to issues with both carrier and temperature management, due to novel dynamics specific to the microscale. Hence, the goal of this PhD will be to develop a new characterization technique for high spatial resolution temperature sensing, that also enables the study of carrier dynamics. Our focus will be on achieving high spatial resolution, which is necessary to access the properties of devices at this scale.

In order to properly understand the characteristics such a measurement technique would need to provide, we need to understand the broader context of current nanothermometry characterization techniques, which will be the focus of this section.

2.4.1 Basics of nanothermometry

The term "nanothermometry" refers to a large collection of techniques that enable the measurement of temperature at the nanoscale, as the name may suggest. The broad nature of the techniques classified under the nanothermometry umbrella stems from the variety of requirements that the potential samples may impose. Different techniques will be used when, for example, characterizing the temperature change of the organelles of a living cell versus studying the heat transfer in a metallic nanotube.

As a side note, we should point out that the concept of temperature is fundamentally a statistical one, and therefore starts to break down when close to the quantum level, requiring careful analysis and a reinterpretation of classical thermodynamics [23, 24]. For our particular work, we aim to achieve a spatial resolution of 14 nm, which corresponds to the lateral dimension of the smallest interaction volume that can be obtained for our range of acceleration voltages. As the materials used (diamond and nitride semiconductors) have an interatomic distance of less than 2 Å[25], we will always work above the quantum level. Hence, the quantum meaning of temperature and the study of quantum thermodynamics are outside the scope of this PhD and will not be further discussed.

The particular focus of the technique developed during this PhD is the detection of local defects in nitride semiconductors used in microscale electronic devices. These local defects can cause a large increase in electrical resistance, and due to Joule heating, lead to malfunctions or even device failure. If detected, these "hot spots" can be fixed, hence the importance of techniques to measure temperature with high spatial precision [26].

Our study has revealed that local defects are particularly critical in the very small (below 2 µm) micrometric devices [1]. As their scale is reduced, the number of hotspots in these devices also becomes smaller, which means the variance in the total amount of hotspots becomes larger, which leads to changes in behavior from device to device. These results will be discussed in chapter 4.

Due to the nature of the defects we seek to characterize, our technique not only requires a high spatial resolution, but since the aim is to study a full structure with said high resolution, speed

and simplicity become also important parameters to take into account.

Beyond the detection of defects, nanothermometry is a useful tool for characterizing all manner of nitride-based semiconductor devices. The focus of this PhD will be photonic devices, particularly LEDs, were key optical parameters are strongly dependent on temperature. These factors include refractive index [27], absorption coefficient [28], Internal Quantum Efficiency [29], and photon energy [30].

2.4.2 Nanothermometry state of the art

Current nanothermometry developments have a strong focus on all-optical nanothermometry [31], since those techniques allow temperature measurements on living organisms without causing tissue damage. This is essential in biology and medicine, fields were temperature mappings have lots of applications, from studying biological processes inside living cells [32] to cancer detection [33]. These all-optical techniques are based on fluorescent nanoparticles, usually lanthanide-doped ones [34]. Due to their optical nature, their spatial resolution is conditioned by the diffraction limit. Although there exist all-optical techniques that can bypass the diffraction limit, such as differential confocal microscopy [35] or stimulated emission depletion [36], the spatial resolution is between 50 and 100 nm, depending on the orientation.

Notably, nitrogen-doped nanodiamonds similar to those used in this study are already being used as optical nanothermometry probes. In particular, the PL signal of the negatively charged Nitrogen-Vacancy center, commonly referred to as NV-, can be used as a thermal probe with an accuracy of up to 10 mK by using a technique know as optically detected magnetic resonance [37]. This technique is discussed in more detail in section 2.4.3, and the nitrogen vacancy center is discussed in more detail in section 5.4. Since there are a series of similarities between photoluminescence and cathodoluminescence spectroscopy, which will be discussed in chapter 3, these Nitrogen-doped nanodiamonds appear to be good candidates to achieve cathodoluminescence nanothermometry, hence why they were chosen.

Another nanothermometry technique is scanning thermal microscopy [38]. This technique is based on scanning probe microscopy, using similar principles: A temperature sensitive prove

is placed on a Atomic Force Microscope (AFM), and then used to scan the sample. Because this procedure requires the sample to be approached with a relatively large probe, thermal exchange between the sample and the tip will occur. Hence, results need to be carefully analyzed, considering the conductivity of the materials involved.

Depending on the probe, the scanning thermal microscopy can be performed in contact mode (which allows for simultaneous AFM mapping) or non contact mode. Contact mode allows for better thermalization, but also causes enhanced heat exchange, which can distort the results even further.

Scanning thermal microscopy techniques share limitations with AFM, most notably a somewhat low spatial resolution (usually on the order of <100 nm). The probe is only capable of working on samples compatible with AFM, which means roughly flat surfaces, although these techniques have been used successfully in liquids [39]. Advantages include high temporal resolution, in the range of microseconds [40], and a thermal resolution of up to 0.2 K [41].

2.4.3 Optically detected magnetic resonance using NV-

As mentioned above, optically detected magnetic resonance, or ODMR is a technique that uses the properties of the energy levels in the NV- diamond defect to enable high precision thermal and magnetic sensing. Here, we will describe the underlying principles that enable ODMR.

The NV- is divided into two states, ground and excited, both residing inside the diamond bandgap. The separation between the two states is roughly 1.95 eV. More details about these two states will be discussed in section 5.4.

The technique is based on the transition between these ground and excited states. A laser with a wavelength between 460 and 580 nm enables the excitation between the ground and excited state [37], with one caveat: The ground state is a triplet, with three spin magnetic quantum number states $m_s = 0$ and $m_s = \pm 1$. The $m_s = \pm 1$ states both have an energy roughly 12 µeV higher than that of $m_s = 0$. However, this energy difference is highly dependent on temperature.

The key to ODMR is the fact that the laser only enables the transition between the ground $m_s = 0$ and the excited states, but not between the ground $m_s = \pm 1$ and the exited states. Hence, if the NV- is simultaneously irradiated by a laser and a microwave with an energy corresponding to the $m_s = 0$ to $m_s = \pm 1$ transition, the ground $m_s = 0$ state may switch to $m_s = \pm 1$ instead of to the excited state. Hence, the microwave frequency corresponding to the transition will lead to a decrease in PL intensity when compared to other frequencies. As this resonant frequency is temperature dependent, it can be used for thermal sensing.

The magnetometry part of this technique stems from the two $m_s = \pm 1$ states. Their energy is the same under no magnetic field, but under a parallel magnetic field, they will split according to the field strength. This will lead to two resonant frequencies that cause a decrease in PL intensity, and the information on the parallel component of the magnetic field will be obtainable from the energy difference between the two.

Figure 4 a) shows the energy states and transitions in NV- during ODMR, and figure 4 b) shows an experimental example on the evolution of NV- PL intensity under different microwave frequencies, and the two resonant frequencies caused by the presence of a magnetic field.

ODRM has achieved magnetic accuracy of 170 $\mathrm{pT}/\sqrt{\mathrm{Hz}}$ [42], and a thermal accuracy of 5 $\mathrm{mK}/\sqrt{\mathrm{Hz}}$ [37]. The main limitations of this technique are the spot sizes of laser excitation, due to the diffraction limit, and the complexity of the experimental setup, requiring both PL and a microwave antenna. However, ODMR is incompatible with cathodoluminescence, as the NV- state can not be excited with electron radiation [43]. Hence, we will need to develop a different method to measure the temperature.

2.5 Diamond-based cathodoluminescence nanothermometry

As observed from the issues discussed in section 2.3, a good understanding of carrier dynamics and thermal properties is required for the proper design and improvement of microelectronic devices. And due to the strong localization of the effects involved, spatial resolution becomes a top priority.

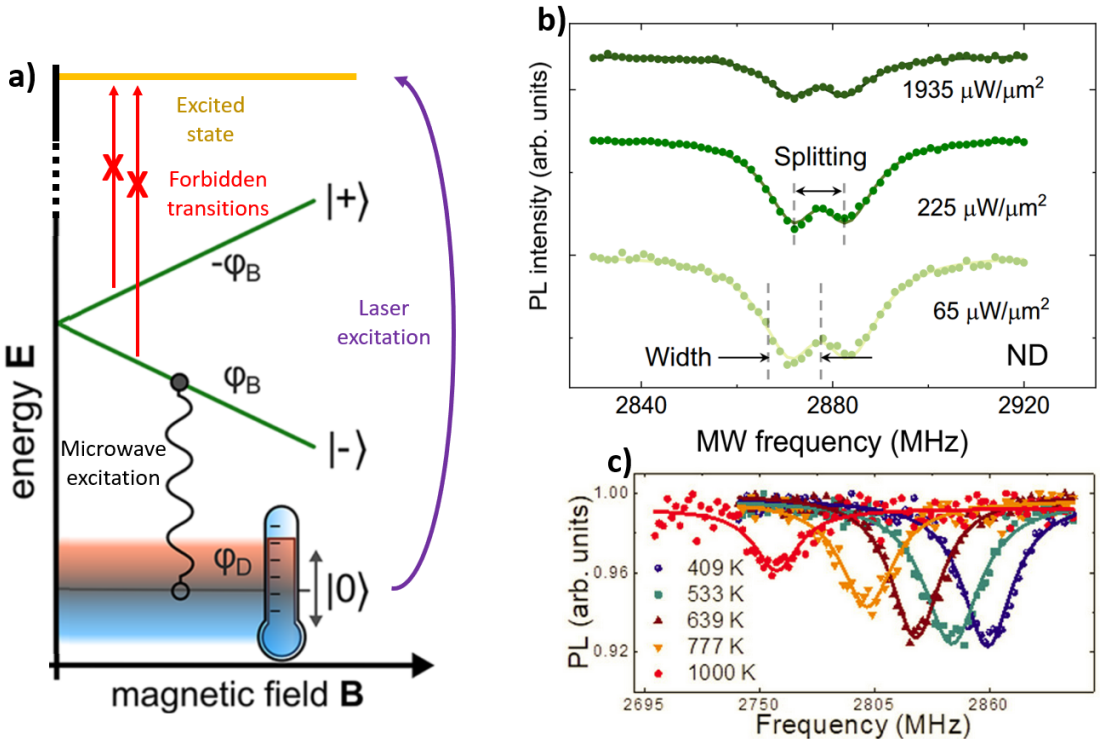


Figure 4: a) Diagram of energy levels in the NV- center during ODMR. Source: [37]. b) Experimental results of resonance splitting in NV- fluorescence under a magnetic field. Source [44]. c) ODMR spectra of NV ensembles in nanodiamond at elevated temperature, showing the energy shift with temperature. Source [45].

Hence, the goal of this PhD will be to develop a hybrid technique that enables the simultaneous study of carrier dynamics and temperature at the nanoscale. In particular, we will study the potential to employ cathodoluminescence for temperature sensing. Cathodoluminescence, or CL, is a technique that already enables carrier characterization, and is not diffraction limited, which means it can achieve a very high spatial resolution without the complex setups of STED. CL will be discussed in detail in section 3.2.

In order to actually achieve temperature sensing using CL, a probe will be used, similarly to PL techniques. The particular probe chosen was nanodiamond, as they have already been proven to work as PL thermal probes. Many of the reasons that make nanodiamonds great thermal probes translate directly to CL probes: The high chemical and physical stability not only make them useful on a diverse range of potential samples, but also make them resilient to the potential damage of the electron bombardment used in CL. The high thermal conductivity of diamond which enables quick thermalization is equally useful in our case than in PL thermometry, and the fact that nanodiamonds can be grown as small as a single nanometer [46] means their size

will not be a limiting factor for the spatial resolution of our method.

3 Experimental methods

As the goal of this PhD is the development of a new measuring technique, we need to establish a good understanding of the capabilities and limits of the experimental setup used during its development. Hence, the following chapter will be dedicated to the experimental equipment and methods used during the development of this thesis.

3.1 Field Emission Scanning Electron Microscope

The main experimental setup used during this PhD was the Field Emission Scanning Electron Microscope (FESEM) FEI Inspect F50 at Institute Neel, managed by Fabrice Donatini.

The FESEM allows for an electron acceleration voltage range between 200 V and 30 kV. Temperature control is achieved via a Gatan helium cryogenic stage, allowing for a range of temperatures from 5 to 320 K. Using a series of turbomolecular vacuum pumps, the FESEM operates at a sample chamber pressure of 10^{-6} mBar, and a gun chamber pressure of 10^{-10} mBar.

To form an image in FESEM, the sample is bombarded with electrons emitted from the tip of the electron gun, called primary electrons. When the electrons impact the sample, they produce secondary and back-scattered electrons, which are then collected to form the image. Secondary electrons were those that originally formed part of the sample and were expelled by the high energy of the primary electrons, whereas back-scattered electrons are primary electrons that have bounced back after interacting with the sample.

The effect of the primary electrons is not limited to the emission of secondary and back-scattered electrons. Braking radiation, commonly referred to as bremsstrahlung, is emitted by the primary electrons inside the sample. Due to the high energy involved, the bremsstrahlung is usually in the X-ray range.

Auger electrons are a particular type of secondary electron with very low energy. When a inner shell electron is expelled as a secondary electron, the vacancy state left will have a lower energy

than most electrons in the atom. Hence, an electron from a higher energy level may fill the vacancy, and the transfer the energy to an outer shell electron, which will be expelled into free space. This phenomenon is known as the Auger effect, and the released electron is the Auger electron.

If the energy from a filled inner shell vacancy is released as a photon instead, it will produce what is called a characteristic x-ray, referred as such due to its energy being dependent on the atomic composition of the sample.

Primary electrons will also transfer some of their energy to the sample. This will result in localized heating and the formation of electron-hole pairs, as the energy from primary electrons excites the energy levels of the sample. Finally, as the primary electrons represent a current entering the sample, electrical charge will accumulate in samples that are not conductive enough to dissipate this current. Charge accumulation can be limited by the use of silver paint to create a bridge between the sample surface and the conductive sample holder.

The e-h pairs created by the beam can decay radiatively, emitting a photon. Studying this light will provide information about the sample energy structure, which will be the basis of cathodoluminescence spectroscopy, a technique discussed in detail in section 3.2.

A diagram of the different interactions produced in FESEM can be seen in figure 5.

Increasing the acceleration voltage will increase the energy of primary electrons, and therefore, the amount of secondary electrons, leading to a higher resolution: From 3 nm at 1 keV to 1 nm at 30 keV, according to product specifications. The main issue with higher acceleration voltages is the risk of damaging the sample. Higher voltages also have an effect when performing cathodoluminescence, reducing the relative contribution of the sample surface to the total CL signal.

This loss of sample surface CL signal occurs because the interaction volume of primary electrons will grow in size as the acceleration voltage is increased. This volume will dictate the region of the sample in which e-h pairs will be formed, and therefore will be vital for performing cathodoluminescence measurements.

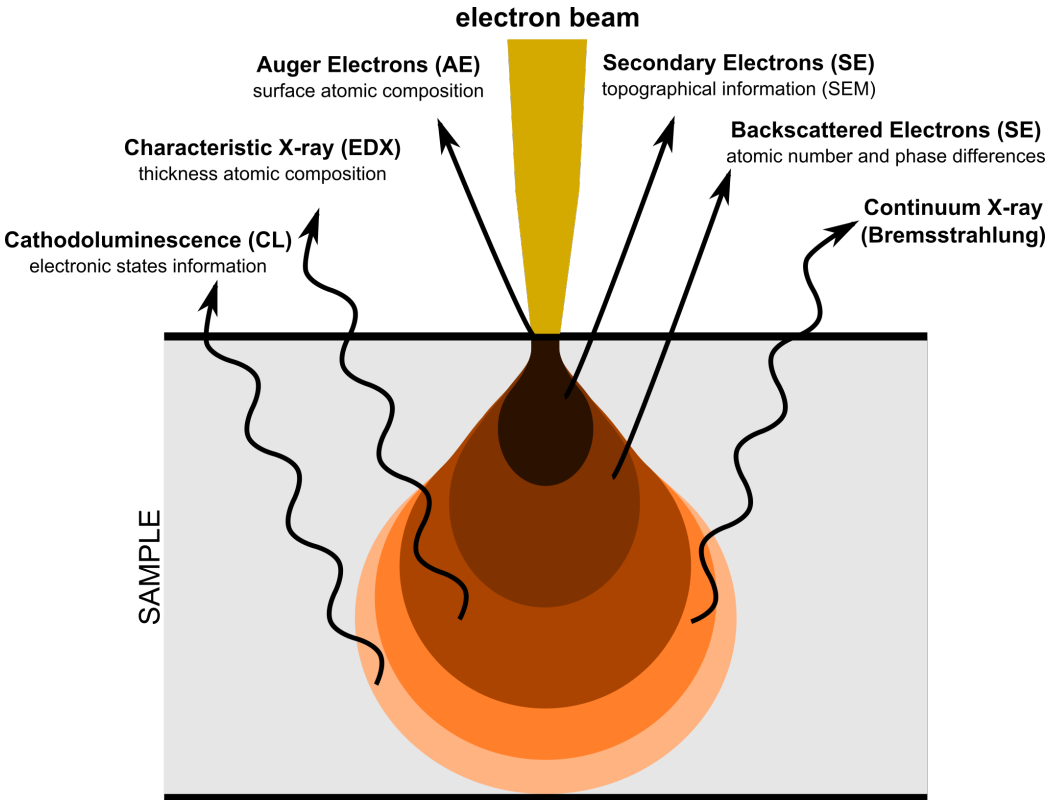


Figure 5: Interaction volume and different types of electron-matter interaction in FESEM operation. Source [47]

This interaction volume (also called penetration volume) will depend on the material studied and the acceleration voltage. The shape and size of the volume can be calculated with the aid of CASINO simulation software [48]. Figure 6 shows some examples of this volume in diamond. As we can see, for an acceleration voltage of 1 kV, the cathodoluminescence spatial resolution in diamond is 14 nm, the lateral dimension of the volume in which 95% of the total beam energy is deposited.

3.2 Cathodoluminescence spectroscopy

The two main characterization techniques used for the PhD are cathodoluminescence (CL) and photoluminescence (PL) spectroscopies. Both techniques are based on studying the light emitted from a sample when excited via particle bombardment. In either case the light is produced by the decay of electron-hole (EH) pairs inside the sample created by the original particle. The core difference is the particle that causes the original excitation: photons in the case of PL, electrons

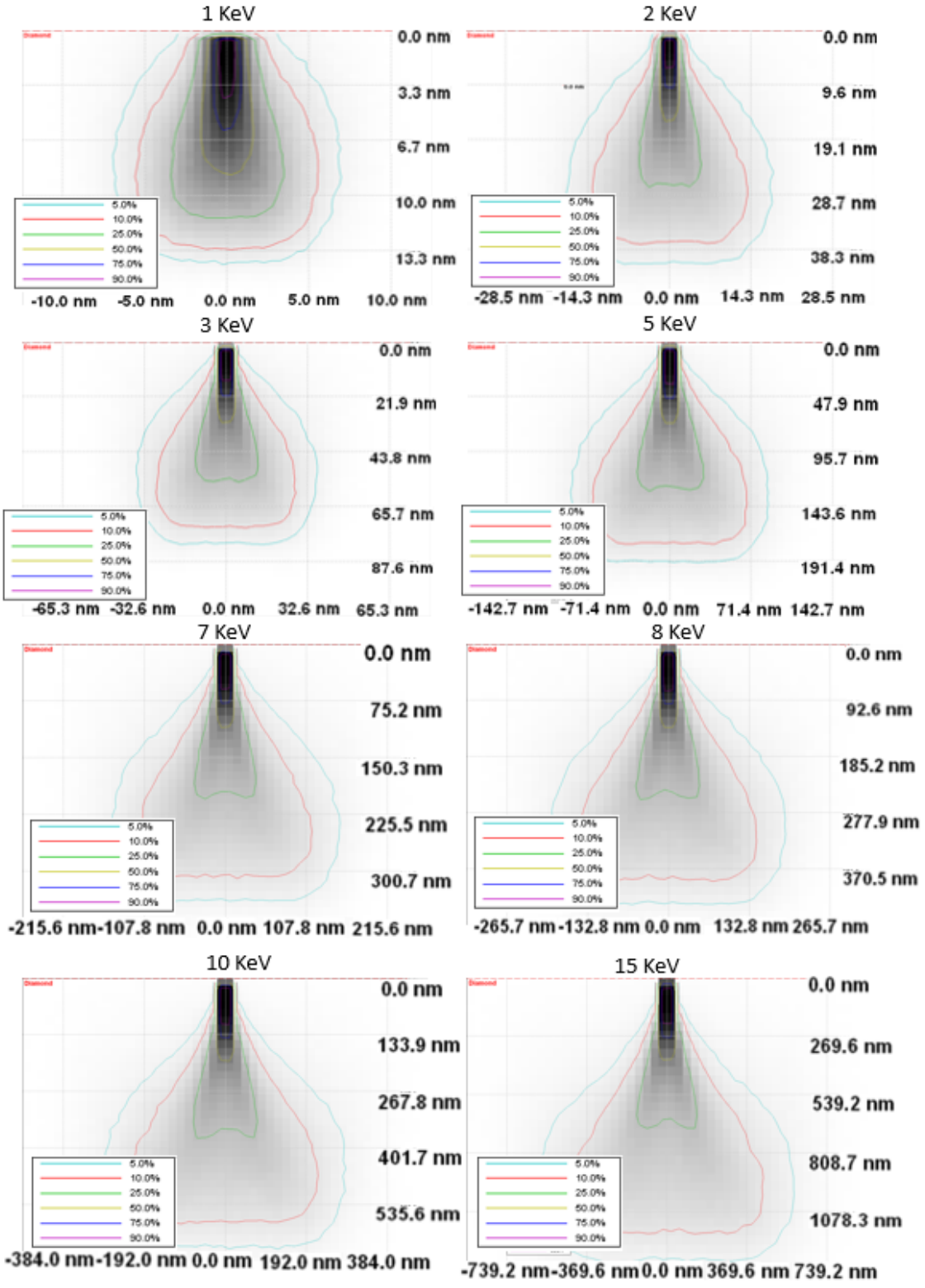


Figure 6: Simulations of the interaction volume of an electron beam inside a diamond sample, performed using the CASINO software [48]. The droplet-like shape of the region is similar for other materials, although its size can change significantly.

in the case of CL.

Despite their similarities, there are important differences between PL and CL. The energy of the photons is much lower than that of electrons, and the fixed wavelength allows to excite only part of the spectrum. In contrast, CL will excite the full spectrum, and the energy of a single electron will be spread around a region, the interaction volume shown in figure 6. As multiple excitations will be produced almost simultaneously at the arrival of single electrons, the lifetime of CL created e-h pairs can be measured by using the so-called autocorrelation function, which we can obtained using a Hanbury Brown Twiss interferometer (HBT). Both the autocorrelation function and the HBT interferometer which will discussed in more detail in section 3.4.

Our main focus will be CL, which we will proceed to discuss now in more detail. PL, and its differences with CL will be discussed in the following section. As discussed in chapter 2, our interest in the nanodiamond CL spectra for nanothermometry stems from the higher spatial resolution that can be achieved with an electron beam in contrast with a laser spot, affected by the diffraction limit of light [49].

The electron beam used for CL measurements is that of the FESEM discussed in section 3.1, therefore the same limitations and considerations discussed in that section will apply to this technique as well. Notably for our goals, the localized heating effect will limit our thermal resolution, especially at very low temperatures.

There is an important difference to consider between FESEM and CL, related to the interaction volume. In the case of CL, the resolution given by this volume is only part of the story, as the charge carriers created by the beam can diffuse in the material. This diffusion causes the CL signal to be emitted over a much larger area than the original interaction volume. For example, excitons in diamond have an average diffusion length of 34 µm at room temperature [50]. This may seem like a serious limitation to our goal of high spatial resolution thermal sensing. However, as our method would be based on isolated nanodiamonds, exciton diffusion will be limited to the individual nanodiamonds excited by the electron beam.

Figure 7 shows a diagram of the FESEM setup, which enables simultaneous, photoluminescence, cathodoluminescence, and HBT measurements at different temperatures. Standard FESEM

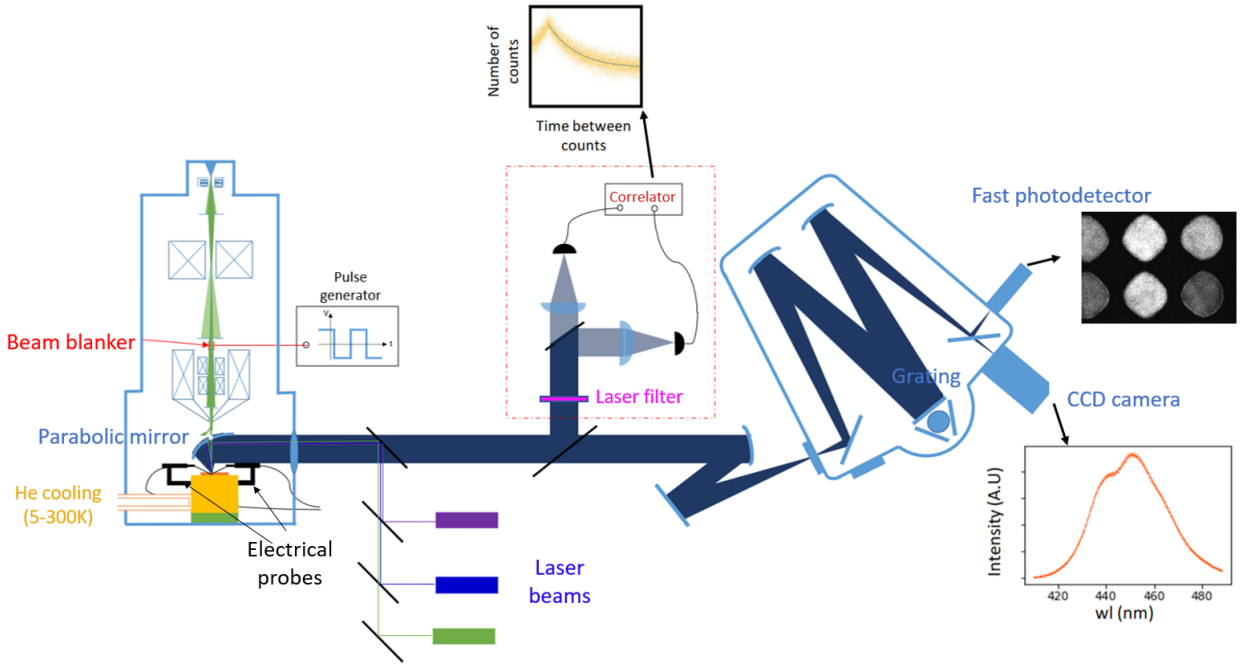


Figure 7: SEM setup used for CL and PL measurements. The spectrometer is a combination of a diffraction grating and a USB 2.0 Newton BU2 DU940P CCD camera [51].

imaging can also be performed these methods, but the parabolic mirror placed to collect the light beam reduces the collection of secondary electrons, and therefore the contrast.

The mirror will also affect the minimum possible temperature of the sample. As mentioned in section 3.1, temperature is set via a helium cryogenic stage, which is situated below the sample, while the mirror is connected to the side of the chamber, and therefore will be at room temperature. The vacuum inside the chamber stops heat from transferring directly between sample and mirror, but the sample will still absorb the black body radiation emitted by the mirror. This effect will be specially noticeable at low temperature, leading to a real minimum temperature of about 10-15 K, depending on the thermal conductivity of the sample and sample holder. Our particular observations with bulk diamond using a copper sample holder gave us a minimal temperature of 17.4 ± 0.1 K.

As discussed in section 3.1, the e-h pairs, and therefore the CL photons, are created alongside an interaction volume. This volume will depend on the material impacted and acceleration voltage. We will have to consider the acceleration voltage and the carrier diffusion carefully when performing CL to understand what parts of the sample we are characterizing.

After being generated, the photons must be collected by the parabolic mirror. Care must be taken to adequately position the mirror to ensure the center of the interaction volume matches the position of the focal point of the parabola. The mirror can be moved in the X and Y axis, while the sample holder can be moved in the Z direction. This means, for example, that sample holder realignment must be performed when changing acceleration voltages, as the center of the interaction volume is deeper inside the sample for the higher energy electrons, and the beam lateral position may shift slightly.

The now collected light signal is focused by a set of mirrors, as illustrated in figure 7. This focused signal goes through a slit with controllable aperture. The purpose of the slit is to have a single point at the CCD when the grating is operating as a mirror. A grating spreads different wavelengths at different diffraction angles, so having the studied light originating from a single point is required to achieve a good spectral resolution.

There are two diffraction gratings available in the spectrometer: a 600 g/mm, and a 1800 g/mm, with spectral resolutions of 0.04 nm and 0.012 nm respectively. Despite the higher resolution, the latter is notably less efficient for wavelengths longer than 350 nm, losing most of the light signal. Hence, the grating used depended on the section of the spectra we wished to study.

The spectrometer itself has two possible detectors: a silicon Charge-Coupled Device (CCD) camera, and a PhotoMultiplier Tube (PMT). The CCD enables us to obtain spectral information, as the different pixel positions correspond to different constructive interference wavelengths from the diffraction grating. The PMT enables much faster detection at the expense of lower energy resolution. It can be used to quickly elaborate spatial CL mappings from different wavelengths.

The CCD generates wavelength-resolved intensity measurements for a chosen energy range. The FESEM software enables us to automatically set the electron beam in a single spot, measure the CL spectra with the CCD, change the beam spot position, and repeat. This enables the elaboration of spatial mappings, where hundreds of CL spectra corresponding to the emission of different regions in the sample are measured. This data can be analyzed with the Python software Hyperspy [52]. Some of these spatial CL mappings will be shown in later chapters.

3.3 Photoluminescence spectroscopy

As previously mentioned, photoluminescence is the technique of studying the light emitted by a sample when bombarded with photons. Two setups were available at Néel to perform these types of measurements: The FESEM used in CL and a fluorolog setup. We will start by discussing the former:

The FESEM setup at Néel (figure 7) allows for simultaneous CL and PL measurements. PL is achieved with a 375 nm laser beam. As the figure shows, in PL the mirror is used not only to collect the light, but also to aim the laser towards the sample. Hence, it is specially important to ensure a proper alignment.

As in CL, the e-h inside the sample are not created at a single point, but in a volume. In the case of PL, there exist a theoretical limit, the diffraction limit of light, which was mentioned in section 2.4.2. The limit is caused by the spatial delocalization of the light states, leading to a limit in resolution dictated by the numerical aperture of the mirror and the wavelength used. In our particular case, the resolution limit is 267 nm for a laser of 375 nm. There are some techniques, like STED, that can overcome this limit, but they are quite complex and their application is limited to certain types of samples.

In the case of our setup, the spatial resolution does not reach this limit. Instead, the excitation volume will depend on the laser spot, which can be calculated by setting the grating in the mirror position and using a test sample with high CL emission. As shown in the diagram from figure 7, there are two mirrors that distort the size of the spot: The parabolic mirror, with a focal length of 3 mm, and a concave mirror with a focal length of 200 mm, leading to an optical magnification of 67. Each CCD pixel is 13 by 13 µm in size. By measuring the size of the emitting region of the bright PL sample in the CCD camera, we obtain a width of roughly 7 pixels, which translates to a spot diameter of about 1.4 µm.

As figure 7 shows, it is possible to perform PL and CL imaging simultaneously using our setup. This was achieved with a nanodiamond sample, and will be discussed in section 6.2.2.

A second photoluminescence setup allows us to perform PL measurements with a variable

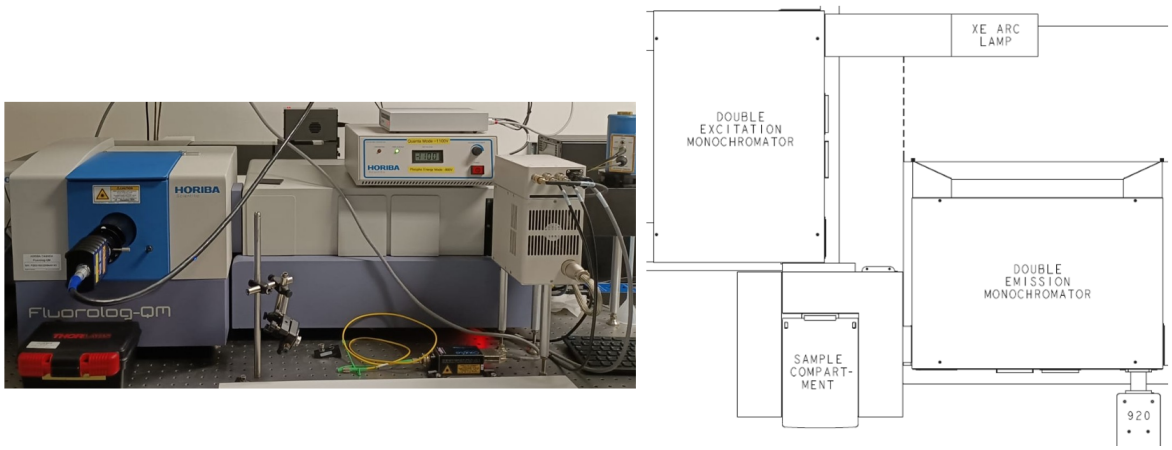


Figure 8: Left: HORIBA Fluorolog-QM used for PL spectroscopy and lifetime measurements. The 452 nm laser can be seen connected to the sample holder Right: Schematic of the Fluorolog setup. Laser not shown.

excitation wavelength (185-900 nm). The device is a HORIBA Fluorolog-QM with the FelixFL proprietary software [53]. A picture of the setup is shown in figure 8. The fluorolog main advantage over the FESEM is the controllable excitation wavelength. The setup is also much faster and simpler to operate, as it excites the entire sample simultaneously, rather than being locally focused, and hence not requiring mirror alignment. As it does not use an electron beam, the fluorolog can operate at room pressure, simplifying the sample loading procedure as well.

The fluorolog is also provided with a 452 nm laser to perform lifetime measurements. However, this wavelength does not excite the NV0 peak strongly enough for lifetime measurements, as will be discussed in section 6.2.

The reason a laser beam is required to measure lifetime in the fluorolog chamber is that the variable excitation lamp does not achieve the level of light bunching required for HBT measurements. A laser itself generates no bunching at all, so the lifetime is instead measured in a more conventional way, by studying the change in intensity of photons of a certain wavelength versus time since the last laser beam pulse. This intensity follows an exponential decay that can be fitted to obtain the lifetime of the excited states emitting at that wavelength.

In order for the lifetime measurement to be possible, the emission of inciding PL photons needs to be controlled with high temporal precision, hence the need for a laser. The laser is controlled with a pulse, which is synchronized with the fluorolog detector. This will cause the laser photons

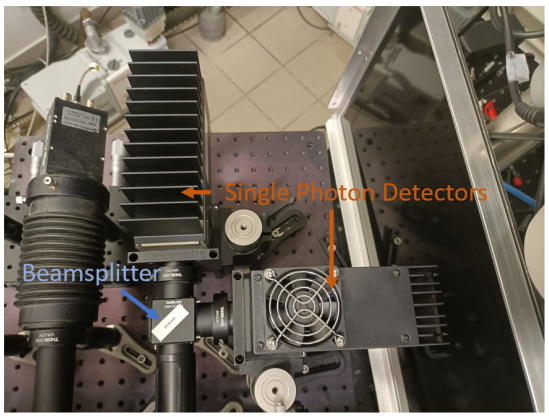


Figure 9: Hanbury-Brown-Twiss interferometer used to measure the autocorrelation function. The setup is is composed of a beam splitter and two single photon detectors connected to an autocorrelator.

to arrive at the sample almost simultaneously at intervals much larger than the e-h lifetime in the sample. This enables the FelixFL proprietary software to extract the sample emission intensity as a function of the time passed since the exposure to the laser beam, which is an exponential decay curve with the PL lifetime as the decay factor.

The fluorolog also has a cryogenic stage that allows for helium temperature measurements, but due to the lack of heater, measurements at the in-between temperatures are not possible.

3.4 Hanbury-Brown-Twiss interferometry

The light created during PL and CL in the FESEM can be studied in a number of ways. In addition to measuring the spectra with the CCD, we have another useful tool available to us: The Hanbury-Brown-Twiss interferometer (HBT), also shown in figure 7.

An HBT interferometer is formed by a beamsplitter, where the original signal is separated in two, and a pair of single photon detectors that each capture half of the original signal. The detectors are then connected to a correlator. This connection is not symmetrical, since a delay is added to one of them. A picture of the HBT setup can be seen in figure 9.

The correlator measures the time between the detection of a photon in the nondelayed photon detector, and a subsequent detection in the delayed one. The purpose of this process is to obtain

what is called the intensity autocorrelation function of light $g^{(2)}(\tau)$ [54]. This function, as the name indicates, is the number of photons emitted by the sample at a time t, given the condition that a photon was emitted at time 0 during the period of measurement.

By this definition, is clear that the autocorrelation function is dependent of both the measurement time and the intensity (and hence beam and light detector conditions). However, simply by normalizing it, $g^{(2)}(\tau)$ becomes the probability of the sample emitting a photon at a time τ, given the condition that a photon was emitted at time 0. The delay introduced in one of the photo-detectors allows access to the negative part of the function, by moving the entire function by a fixed time.

The autocorrelation function carries information on the quantum nature of light. Its shape will always be symmetrical, as the beamsplitter separates photon states in two halves randomly. The function can take on three broad shapes:

1. Poissonian: As the name indicates, this distribution corresponds to a Poissonian light emitter, meaning that photon emissions are independent of each other. Since the probability of a photon being emitted is independent to that of any other photon, the autocorrelation function will be constant.

2. Sub-Poissonian: This distribution corresponds to a single-photon emitter. In this case, the emission of a photon is conditioned to the fact that no other photon was emitted at the same time. Hence, the autocorrelation function will be 0 at $t = 0$, and its value will grow with t at a higher rate the brighter the single photon emitter.

3. Super-Poissonian: This distribution has a maximum at $t = 0$, which then decreases following a negative exponential. This shape shows that photons are more likely to appear closer in time, as if they were "clumped together". More precisely, this distribution corresponds to a large collection of independent excited states with the same lifetime, all of them having become excited at the same time. As they will most likely emit a photon around their lifetime, most of the photons will appear close in time, closer the shorter the lifetime is.

Figure 10 shows the shape of the autocorrelation function for all three statistical distributions

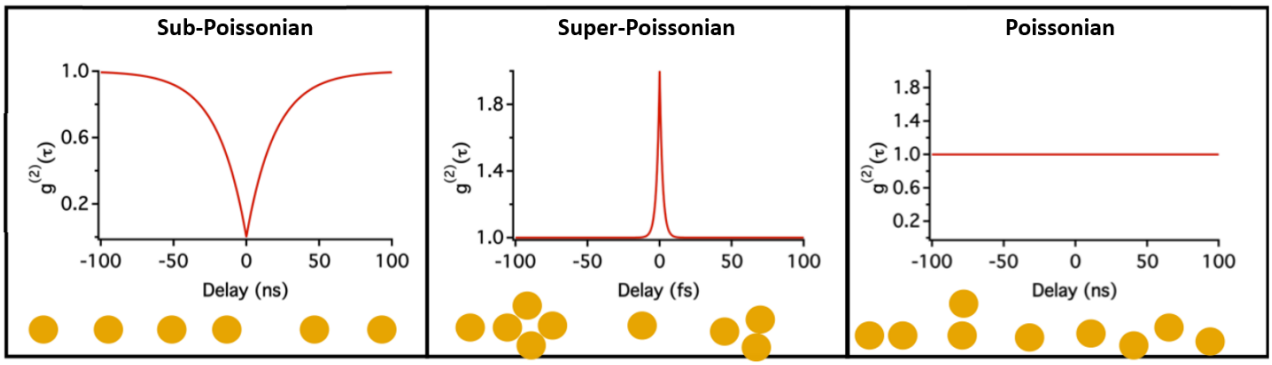


Figure 10: Examples of the three possible shapes of the autocorrelation function of light $g^{(2)}(\tau)$. Source [55]

of light.

In the case of CL light, photons are emitted from e-h pairs with the same lifetime, which are all created together by a single electron impact [56]. Hence, we expect our samples to follow a super-Poissonian distribution, as long as the time between electron arrivals is longer than the lifetime of e-h pairs. If the electrons are too close together in time, e-h pairs created by different primary electrons will emit photons continuously, resulting in a Poissonian distribution.

We can ensure that the time between electron arrivals is longer than the lifetime by either working at low current or using the beam blanker shown in figure 7.

The reason we want Super-Poissonian light is to estimate the lifetime of our excited states. This can be achieved simple by fitting the super-Poissonian autocorrelation function to an exponential decay, with the decay constant being the lifetime [57]. By splitting the beam between CCD and HBT we can simultaneously study the lifetime and spectra of the sample.

3.4.1 Beam blanker

The beam blanker is a device that will block the FESEM electron beam when receiving an electric signal, which enables the screening of the CL signal with a high temporal resolution.

In our setup, the beam blanker consists of a capacitor with a plate separation of 100 µm.

During operation, the beam blanker is placed in the beam trajectory, causing the electrons to pass between the two plates. In this way, when a voltage is applied to the beam blanker, the electrical field between the plates will cause the beam to deviate. For a high enough voltage, this deviation will cause the electrons to be blocked entirely, regardless of the sign of the voltage. The rise and fall time of the beam blanking voltage in our setup has been measured by Donatini and Pernot to be 250 ps [58].

The purpose of the beam blanker for our PhD was to perform direct lifetime measurements, which will be discussed in the following section. The beam blanker can also be used to perform time-resolved CL and electroluminescence, in a process that will be discussed in more detail in section 6.5.3.

3.5 Lifetime measurements

Although the Hanbury-Brown-Twiss interferometer enables us to measure the lifetime of the e-h pairs inside the sample and the spectra simultaneously, it has one limitation. As the rate of incoming electrons needs to be lower than the emission lifetime, we must work at a low current, which leads to a relatively low emission intensity from the samples. If the sample is not bright enough, this method does not allow us to measure lifetime in a reasonable timespan.

In order to measure the lifetime for these less bright samples, we combine a beam blanker and a single photo-detector. This single photo-detector replaces the fast photo-detector in the setup from figure 7, while the beam blanker described in section 3.4.1 is connected to a pulse emitter.

By connecting the beam blanker to a square electric beam pulse that oscillates between 5 and -5 Volts, FESEM electrons will only be able to enter the sample during the very brief transition between the two voltages, which will occur twice per pulse period. Working with a long enough period for the studied sample will ensure that all e-h pairs are created almost simultaneously during a pulse transition, and that the separation between the creation of e-h pairs is large enough for the fully to decay between two events.

Similarly to the fluorolog described in section 3.3, this procedure ensures beam electrons will

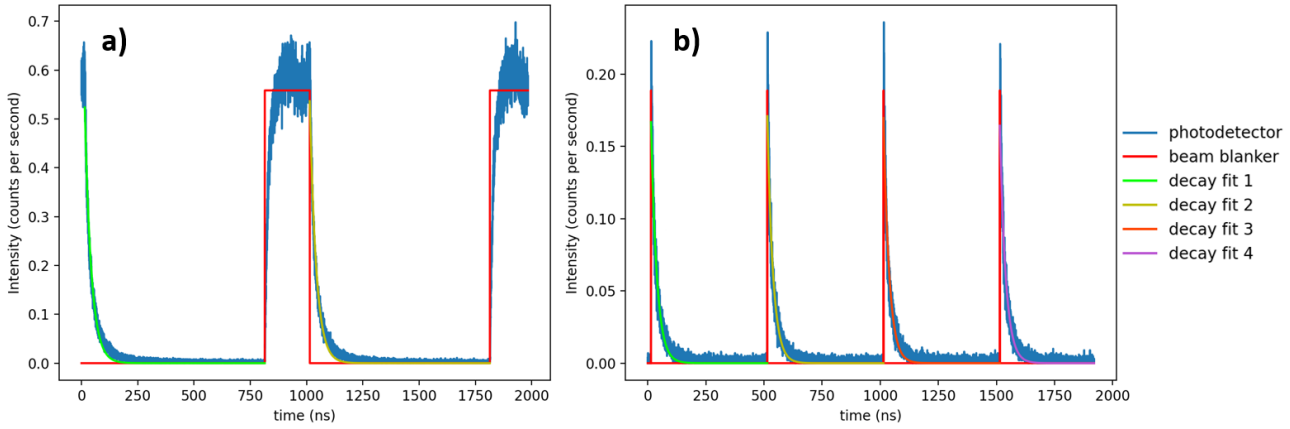


Figure 11: Example of direct lifetime measurement on a nanodiamond sample using a) a 0 to 5 Volts square pulse for the beam blanker b) a -5 to 5 Volts square pulse. The red line indicates the pulse regions in which the Voltage is 0, and therefore the electron beam is active. The exposure time was 1000 seconds for the -5 to 5 Volts pulse and 120 seconds for the 0 to 5 Volts pulse.

arrive at the sample almost simultaneously at intervals much larger than the e-h lifetime of the studied samples. By connecting the single photo-detector and the beam blanker pulse to a correlator, we can obtain the sample emission intensity as a function of the time passed since the creation of e-h, which is precisely an exponential decay curve, with the e-h lifetime as the decay factor.

The main limitation of this method is the low intensity, as a large fraction of the beam current is removed by the beam blanker. Therefore, a faster way to obtain the lifetime is by using a square pulse in the beam blanker that switches between 5 and 0 Volts. The intensity will grow to saturation during the 0 Volts part of the pulse, and then decay according to a similar exponential when the voltage becomes positive and the beam blanker activates. Figure 11 shows examples of both types of measurements. We can see that despite requiring a much higher exposure time, the measurement using discrete e-h creation has a lower total intensity.

3.6 Electroluminescence spectroscopy

The sample holder described in figure 7 is provided with a set of electrical probes, shown in the diagram. Their positions can be controlled independently in all three dimensions by a set of

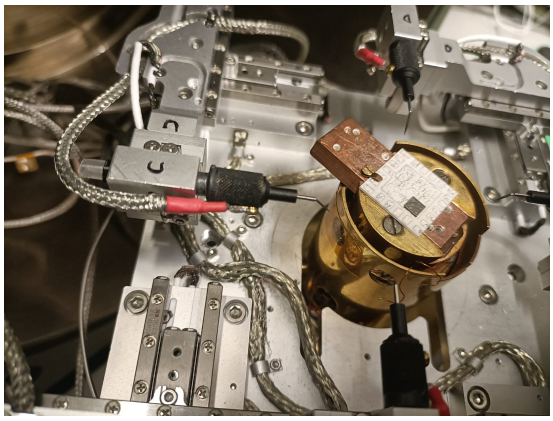


Figure 12: Electroluminescence sample holder and electrical probes in our FESEM setup.

nanomanipulators. By connecting the probes to an external source measuring unit and placing the tip of the probes in contact with the sample, we can create a voltage difference between two points in our sample, and therefore a controllable electrical current. The position of the probe tips can be monitored in real time via FESEM imaging. A picture of the electroluminescence setup can be seen in figure 12.

The electrical probes can be used in conjunction with the mirror, which enables the collection of any potential electroluminescence signal produced by our sample. However, this is not a simple process and must be performed with extreme care. The reason for this is the mirror alignment position, which requires it to be placed in extreme proximity to the sample, with a distance of about 3 millimeters between the two. As the diagram in figure 7 shows, the probes must be placed between the mirror and the sample to perform electroluminescence spectroscopy. The parabolic mirror is extremely delicate, and if it were to touch the metallic probe, it would most likely be damaged. Hence, the probes must be placed as close to the sample as possible, and the mirror alignment step must be done by carefully monitoring the distance between probe and mirror. The FESEM is provided with an interior camera that allows us to gauge this distance.

Although the process of placing the electrical probes alongside the mirror is far from trivial, once that step has been performed, there is nothing in the electroluminescence setup that interferes with the other measurement setups described in this chapter, enabling us to perform electroluminescence alongside other techniques. In fact, in section 6.5.1 we will show some results of cathodoluminescence measurements performed on an active electrical circuit controlled by the electrical probes.

4 Emission Heterogeneity in InGaN/GaN Micro-Light-Emitting Diodes

As mentioned in the general introduction, one of our main objectives in the PhD thesis is to monitor the local temperature at the level of a single micro light-emitting diode (µLED). For this reason, we first investigated the optical properties of such optoelectronic devices prior to the measurements of their local temperature under operation. In particular, we first wanted to assess the homogeneity of the optical properties prior to the deposition of nanodiamonds.

Hence, we performed some CL and PL characterizations of µLED devices. Unexpectedly, our observations show a large variation in CL intensity between similarly sized µLEDs, particularly in the smallest samples. This raised our interest and led us to investigate further, resulting in the publication of an article [1]. In this chapter, we will discuss the results described in the article.

The fundamental physics of LEDs have been previously discussed in section 2.2.1. There are, however, a few considerations on those general principles significant for our particular samples which must be briefly mentioned:

The first of these considerations relates to the extraction efficiency (EXE), the ratio between IQE and EQE. This parameter has a notable impact on GaN-based LED structures such as ours. This is because of the high refractive index of GaN, about 2.48 at room temperature. Such a large value means that the critical angle for an GaN/air interface is roughly 24°, which will cause a large part of the generated light to reflect back inside the LED, making EXE an important magnitude for the optimization of Nitride LEDs [59].

The second consideration relates to the current regime. As mentioned in section 2.2.1, there exist three possible current regimes in which a LED can operate: The low current regime, the peak efficiency regime, and the efficiency droop regime. As will be discussed in section 4.2, we were limited to working in the low current regime in order to access the lifetime of the LED samples with the Hanbury-Brown-Twiss interferometer.

The third consideration relates to the injection of e-h pairs. Under normal operation, this injection is achieved by connecting the LED to a circuit and flowing a current through it. However, in order to investigate the optical properties of the LED, we used both cathodoluminescence or photoluminescence spectroscopy techniques. Hence, injection efficiency needs to be replaced by excitation efficiency: The probability of a beam electron to create at least one e-h pair within the QW.

4.1 LED sample structure

The µLED samples studied were fabricated and treated by Corentin Le Maoult during his PhD [60]. The samples were etched from a commercial blue LED grow on the (0001) direction over sapphire substrate. The structure of the LED was determined by Le Maoult, by using TOF-SIMS (Time Of Flight Secondary-Ion Mass Spectrometry) and by analyzing Scanning Transmission Electron Microscopy (STEM) vertical cuts of the sample. More information on the sample characterization can be found on Le Maoult's PhD thesis [60].

The sample structure from surface to substrate was found to be as follows:

- A 200 nm positively doped GaN layer, with Mg as the hole donor. Mg concentration was estimated to be $4.5 * 10^{19}$ per cm^{-3}.
- A AlInGaN super-lattice embedded in the p-GaN between the depths of 80 and 170 nm. The function of super-lattice seems to be either to increase the electron blocking capabilities of the following EBL (electron blocking layer), to lower the activation energy of the p-GaN to optimize hole injection, or a combination of both effects.
- A 20 nm thick AlGaN EBL. As the name implies, the EBL ensures electrons cannot cross into the p-GaN, ensuring recombination occurs in the MQW.
- The MQW (Multiple Quantum Wells) made of a $In_{0.14}Ga_{0.86}N$ alloy. Each QW is 3 nm thick, and they are separated by 15 nm barriers of intrinsic GaN, for a total of 147 nm.
- A small (68 nm) undoped GaN layer between the depths of 367 and 435 nm.

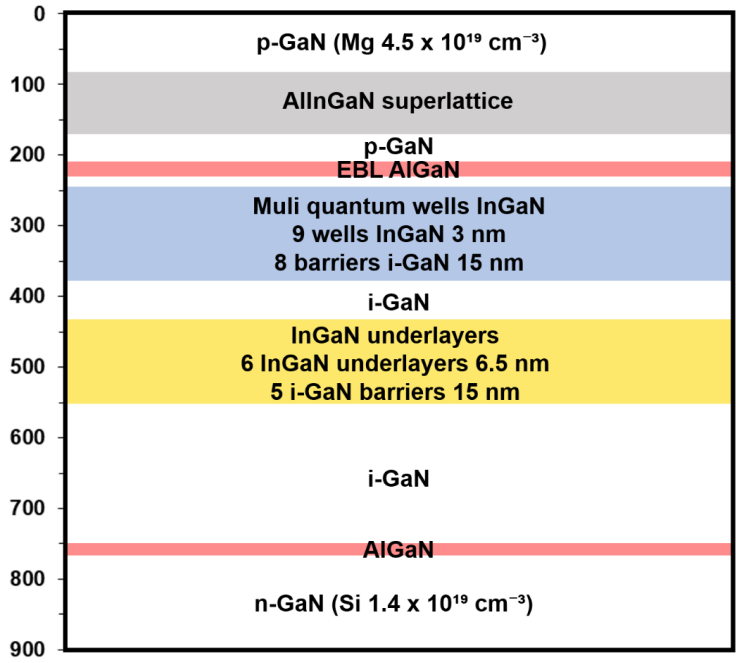


Figure 13: Structure of the commercial blue LED samples used in our study. The sample was etched into µLED by Corentin Le Maoult. Source [60]

- The $In_{0.14}Ga_{0.86}N$ UL (under layers). Each of the six UL is 6.5 nm thick, and they are once again separated by 15 nm intrinsic GaN barriers, for a total width of 115 nm. The function of this underlayer is to reduce point defect density [61].
- A 200 nm buffer layer of intrinsic GaN, between the depths of 550 and 750 nm.
- A small (20 nm) AlGaN buffer layer.
- A negatively doped GaN layer, with Si as the electron donor. Si concentration was estimated to be $1.4 * 10^{19}$. According to our own calculations, this layer has a thickness of 2100 nm. These calculations will be discussed in section 4.3.1.

A diagram of the LED structure can be seen in figure 13.

This commercial LED was then etched into µLEDs of both circular and square shapes, with sizes ranging from 1 to 100 micrometers. The method used was an Inductively Coupled Plasma Reactive Ion Etching (ICP-RIE) optimized by CEA-LETI. The process consists on the deposition of a SiO_2 hard mask, followed by 1 µm of etching using Cl_2/BCl_3. The hard mask was finally removed via buffered oxide etch (BOE).

As discussed in section 2.2.1 one of the main limitations to the luminosity of µLEDs is surface recombination. This effect appears when some electron-hole pairs decay using non-radiative states on the sidewalls of the LED rather than forming a photon in the quantum well. These recombinations lead to a major loss of intensity, especially for smaller samples with larger surface-to-volume ratio. In order to limit this effect, Le Maoult performed a passivation treatment on the LED samples.

This passivation consisted of a nitrification pre-treatment achieved via N_2–H_2 plasma, followed by the intercalated growth of AlN-Al_2O_3-AlN layers on the sidewall. The growth was performed using Plasma Enhanced Atomic Layer Deposition (PEALD).

4.2 LED sample measurements

In order to study the properties of our LED samples, we employed the techniques discussed in chapter 3, with a particular focus on PL and CL. There are common techniques for LED characterization, as both allow access to the bandgap energy of the QW directly from the emitted photon energy. In our particular case of Nitride LEDs, knowledge of the bandgap energy allows us to spatially map the presence and concentrations of the group III elements, as they have a known effect on the bandgap [62]. However, this is only a small part of the kind of characterization these techniques can achieve, as will be discussed in the chapter.

4.2.1 Photoluminescence measurements

In order to properly study the µLED samples, a high spatial resolution was required. Resolution needs to be high enough to distinguish the individual smaller samples, but also to study the differences in emission between the areas in a single µLED. As mentioned in section 4.1, surface recombination is a common effect in µLEDs. Hence, in order to understand the samples properly, we need to be able to study the emission properties of the edge and the center and the differences between the two.

A first attempt to characterize the samples was done using the photoluminescence setup in the

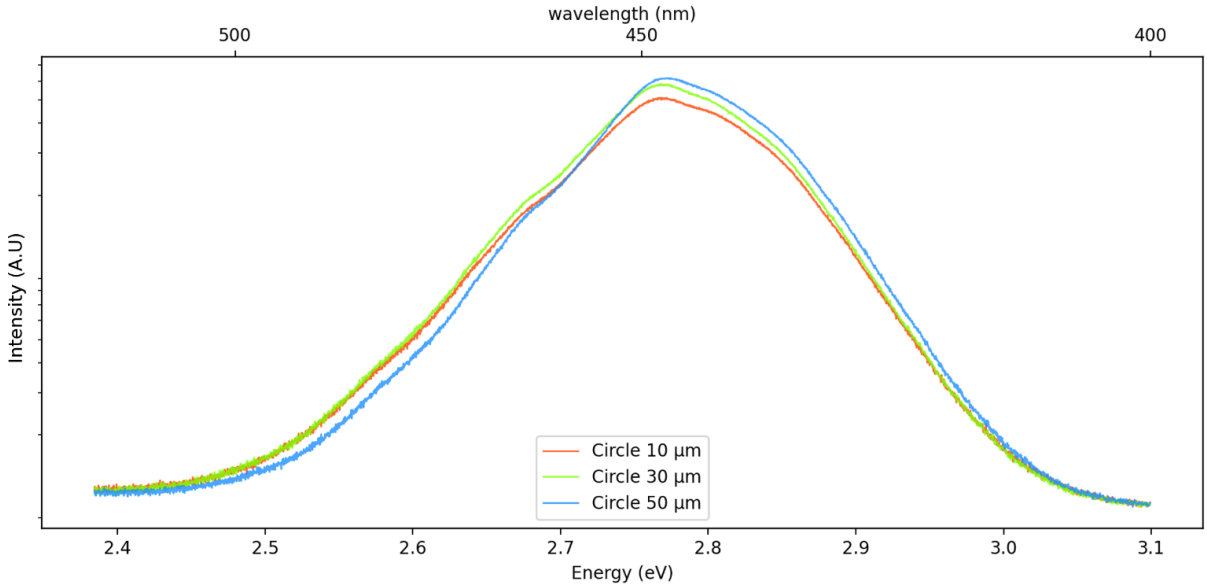


Figure 14: photoluminescence results on three circular µLEDs of different sizes. Laser was focused at the center of the sample.

FESEM described in section 3.3. However, it became clear than the spatial resolution was not high enough to distinguish the different regions inside the µLEDs. Despite this limitation, we noticed that bigger samples had their average emission blue-shifted compared to small ones. Figure 14 examples of this effect for circular samples. This blue-shift was similarly present in square samples.

The shape of the PL peaks is consistent with emission from a single QW, modulated by an interference pattern caused by a GaN structure of 2800 nm of size. This behavior allowed us to infer the thickness of the n-GaN layer. Similar results were observed in CL spectra. The interference pattern will be discussed in more detail in section 4.3.1.

4.2.2 Spatially resolved CL-HBT measurements

To improve spatial resolution, the majority of our µLED study was done using electron beam techniques: FESEM, CL, and HBT interferometry. As discussed in chapter 3, all these techniques can be performed simultaneously. The acceleration voltage was chosen to be 10 kV for all measurements. This value was chosen based on CASINO simulations, which revealed this acceleration creates an interaction volume large enough to reach the QW inside the

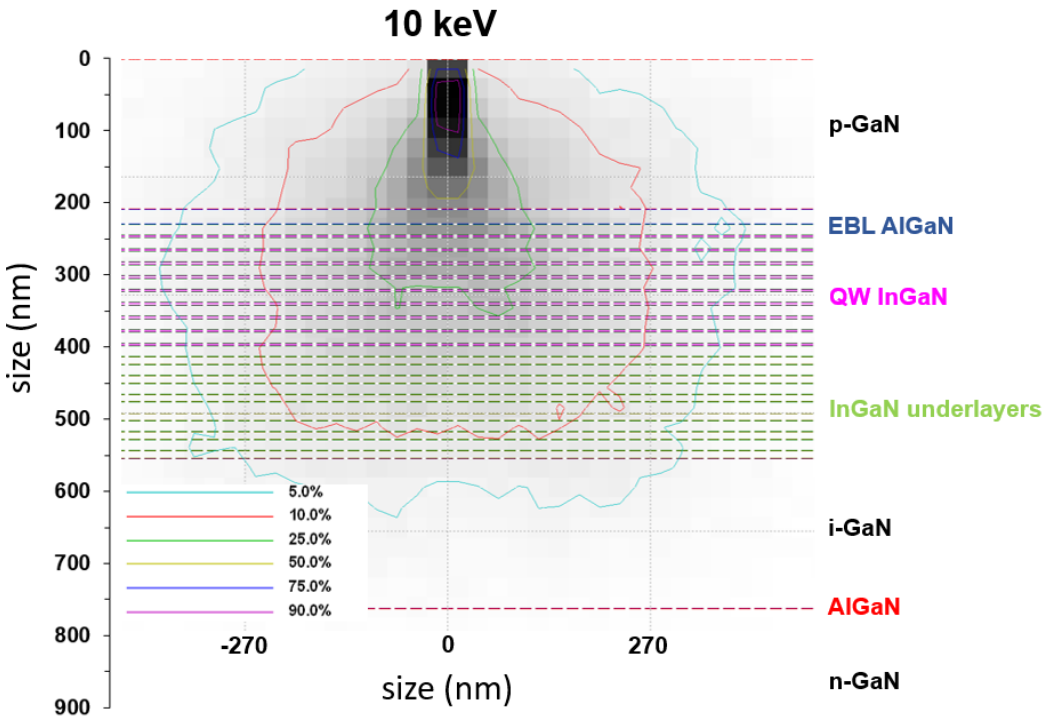


Figure 15: CASINO simulations [48] of the interaction volume of an 10 keV electron beam inside the LED sample structure previously shown in figure 13. The different regions are delimited according to the fraction of beam electron energy absorbed by the sample.

sample, enabling the creation of e-h pairs, and therefore photons. Figure 15 shows the result of this simulation.

Figure 16 shows an example of the combined measurement that can be achieved by our setup. For each pixel in the studied area, we obtain a CL spectra and an autocorrelation function. In order to visually display the information, the figure shows the fitted lifetime of the autocorrelation function, the number of CL counts, and the average wavelength. More than a 150 different individual µLEDs were studied using this type of mapping.

As mentioned in section 3.4, HBT measurements requires the photon bunches do not overlap. To achieve this, the time between the arrival of two electrons needs to be significantly larger than the carrier lifetime. This puts a hard cap on the beam current; therefore, all measurements were done under carrier densities that corresponded to the low current regime of the µLEDs.

Fortunately, as the µLED samples were very bright, a exposure of less than a second was enough for each spatial position even at low current. This lead to a scanning time between 10 and 30

minutes per µLED, depending of the spatial resolution used.

Figure 16 illustrates a series of interesting behaviors, that were observed in all samples. First of all, the effect of the edge: As the subfigure D shows, the lifetime of the e-h pairs significantly decreases near the edges of the samples. This effect is caused by surface recombinations, which create a new decay path for the e-h pairs. This loss in lifetime is to be expected, and was already observed by previous studies [63, 64].

Interestingly, this loss of lifetime does not correspond to a loss in intensity, but on the contrary, as figure 16 C shows, intensity actually seems to grow at the edges of the sample. This was true for all the mappings, and the reason is explained in the work of Sylvain Finot [63].

As Finot describes in his thesis, the edges of the µLED mesas are not perfectly vertical, but have some level of inclination. For this reason, an electron beam impacting on the edge will generate an interaction volume with potentially higher overlap with the quantum well, as figure 17 illustrates. Larger overlap means more e-h pairs, leading to higher intensity, even if the IQE is lower due to surface recombinations.

Furthermore, the edge of the LED also increases light intensity by providing an extra surface for photons to escape the LED. As mentioned in section 2.2.1, the high refractive index of GaN means most inciding angles of light cannot escape the sample, so an extra surface provides an alternative path for some of those photons. The enhancing effect of the surface has been studied by Olivier *et al.* [65].

A second effect of the edge that can be observed in figure 16 b) is the blue shift that occurs in the LED CL emission. This blue shift at the edge was present in all samples, regardless of size or shape. This blueshift has already been observed by Xie *et al.* [66] and Zhang *et al.* [67], and has been attributed to strain relaxation caused by the edge leading to a shift in the band gap.

The most strange behavior seen in figure 16 are the dark spots in CL intensity (subfigure C) that do not correspond to a change in lifetime. Similar results were observed in all samples.

Since the spots do not show a change in lifetime, they can not correspond to a variation of

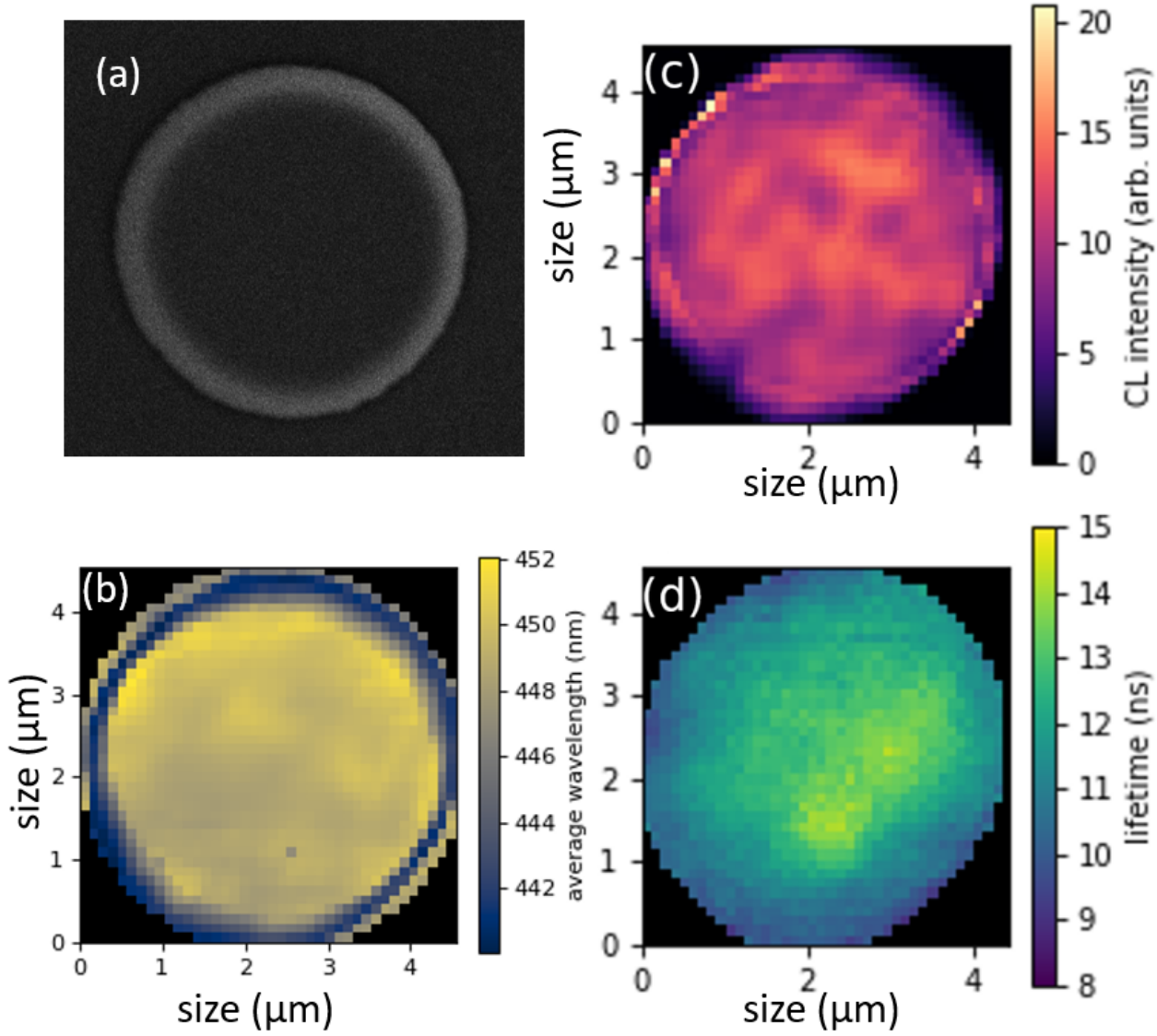


Figure 16: a) SEM image of a circular 4 µm LED. CL mapping of b) average wavelength, c) total intensity, and d) estimated lifetime of the LED from autocorrelation function. The measurements were done with the setup described in figure 7, at room temperature and without the PL laser. Acceleration voltage was 10 kV.

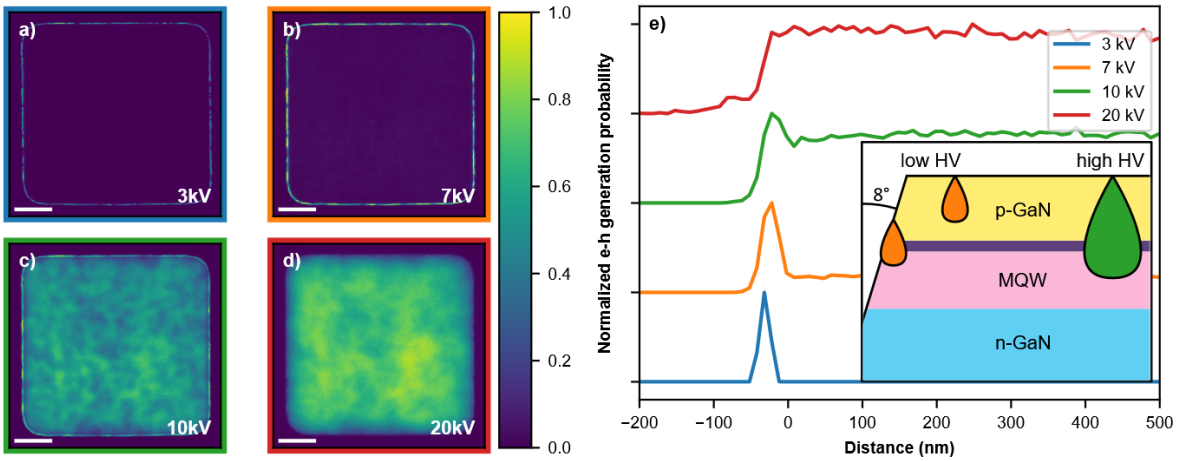


Figure 17: a-d) CL images of the same µLED at the quantum well energy (440 ± 10 nm) for different acceleration voltages. The scale bar is 2 µm long. (e) Normalized e-h pair generation probability in the active region simulated with CASINO. (inset) Schematic of the interaction volume at low (orange) and high acceleration voltage (green). Source: [63]

internal quantum efficiency. A change in IQE implies a change in the decay path of e-h pairs, and hence in their lifetime. We have attributed the intensity change to a change in excitation efficiency caused by the presence of a defect structure called the V-pit. We will discuss the interpretation of these dark spots in further detail in section 4.3.

Although the acceleration voltage was kept constant in all measurements, the total current was changed between measurements. As we stayed in the low voltage regime, current did not have an impact on any emission properties besides light intensity. Still, this must be taken into account, as we cannot compare the intensity of samples under different currents.

To enable a quick comparison of the intensity of multiple samples under the same beam conditions without requiring a full CL mapping of each, we used the PhotoMultiplier Tube discussed in section 3.2. The PMT can be used to quickly generate an image of the relative CL intensity of a certain wavelength. Figure 18 shows an example of this kind of measurement for the smaller samples, the 1.2 µm circles. The image shows the advantage of using the PMT, enabling us to directly compare emission intensity in the 450 nm wavelength of 48 different samples, at the expense of losing access to the spectra and lifetime.

Figure 18 shows that intensity varies very significantly between these small LED samples, despite

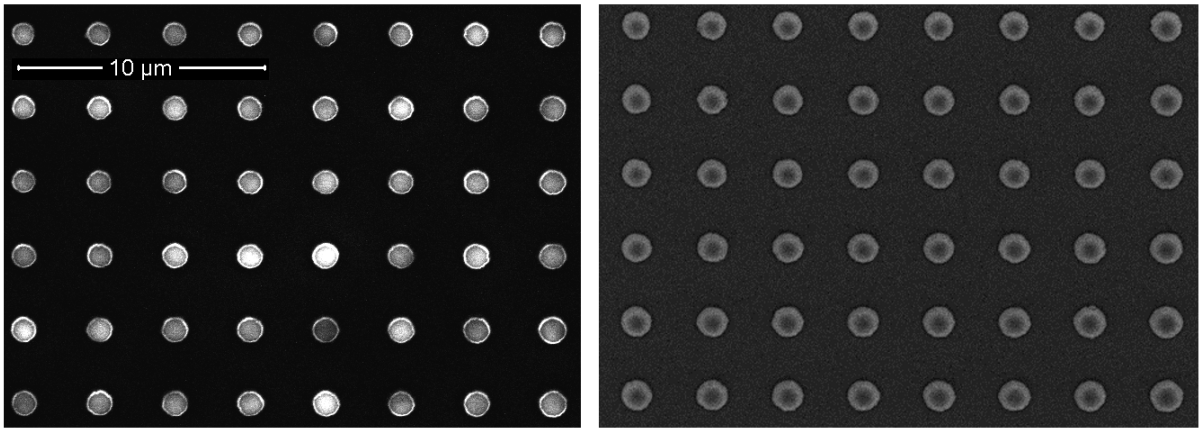


Figure 18: Left: Panchromatic CL image at 450 nm of a collection of 1.2 µm circular LEDs, obtained using the PMT. Brightness indicates CL intensity at the chosen wavelength. The images were obtained with an acceleration voltage of 10 kV and an electron beam current of 14 pA. Right: SEM imaging of the same samples.

their similar shape and structure, with the brightest samples more than doubling the intensity of the smaller ones. This strong variation was lessened in bigger samples, but still present. The origin of these changes in intensity will be discussed in section 4.3.

When studying the emission of the different samples, the first surprise was the lack of correlation between the average intensity of the samples and their average lifetime. A shorter lifetime usually indicates the presence of alternative decay paths for e-h pairs, leading to lower IQE, and therefore lower total intensity. However, as shown in figure 19, the relationship is actually the opposite.

Figure 19 only shows the measurements for a beam current of 14 pA, as intensity cannot be directly compared between different currents. Results were similar for the other tested currents. Despite this limitation we can still observe the variation in intensity for seemingly identical samples discussed before, and how it is particularly strong for the smallest LEDs.

The negative correlation in figure 19 means the change in CL intensity is not related to an IQE variation. Instead, these results can be explained by the different sizes of µLEDs studied. Within pixels of the same size, the correlation between intensity and lifetime is positive, but smaller samples have larger intensity and lower lifetime.

The lower lifetime of smaller µLEDs is due to surface recombination, which as discussed before,

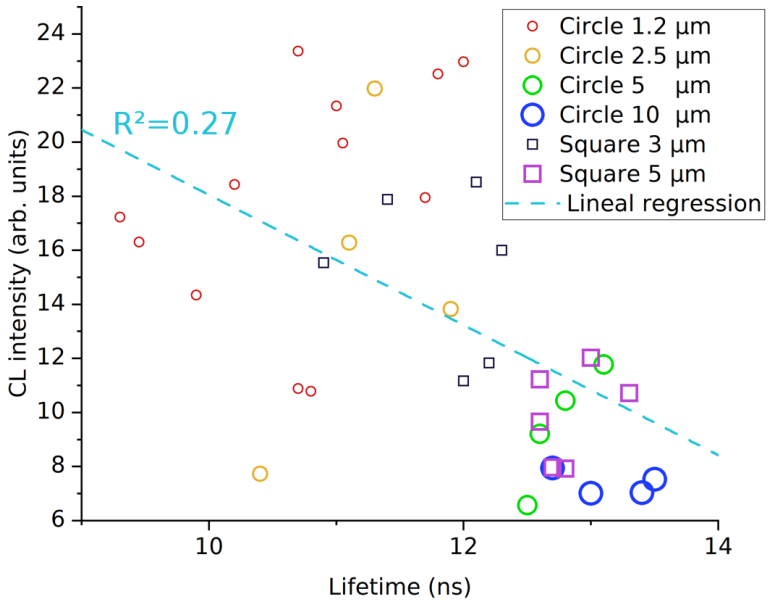


Figure 19: CL Intensity vs lifetime at the center of the µLED samples for an acceleration voltage of 10 kV and a current of 14 pA. There is a low negative of correlation between intensity and lifetime. There is also a negative correlation between the lifetime and the pixel size, with smaller pixels having shorter lifetimes.

is more prominent in smaller samples. The higher intensity of smaller µLEDs indicates that the extraction efficiency is favored, due to the extra surface provided by the sidewalls. Figure 19 does not include the edge contribution, only the intensity in the interior of the sample. Hence, is clear that the extra extraction efficiency of smaller samples has a global effect on the intensity, not only on the edge. Another effect that could contribute to the enhanced intensity of the smallest pixels is the presence of resonant cavity modes, such as whispering gallery modes [68].

When studying the CL spectra of the different samples, another interesting correlation appears: CL intensity grows in samples that are red shifted, as figure 20 (a) shows. This effect is particularly pronounced in smaller samples, which, as figure 20 (b) shows, have a larger range of possible average wavelengths. This is related to the previous observation that smaller samples have a broader range of intensities, as these two magnitudes are correlated.

Figure 20 (b) also shows that, just as it was observed for PL measurements, bigger samples are blue-shifted compared to smaller ones. Since the samples were all etched from the same LED, their differences in wavelength cannot be explained by a difference in the QW composition. Hence, the blue-shift is likely related to strain relaxation, which points to the existence of a

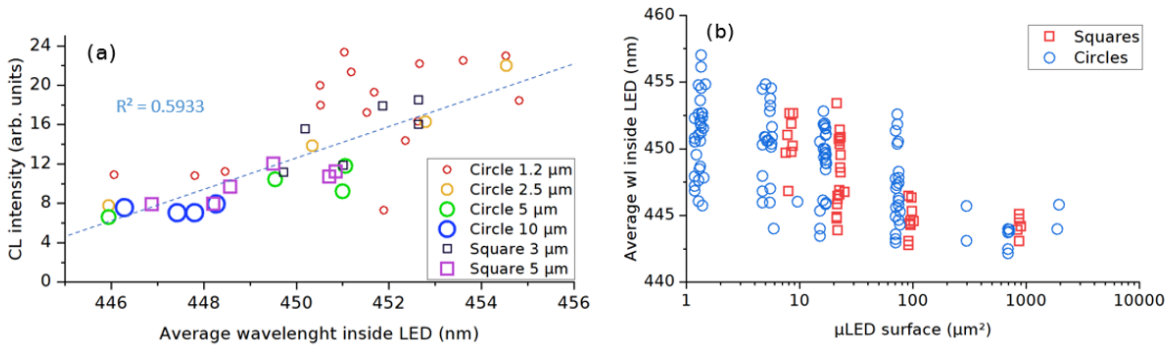


Figure 20: (a) CL intensity as a function of arithmetic mean emission wavelength at the center of the µLED samples for an acceleration voltage of 10 kV and a current of 14 pA. (b) Arithmetic mean emission wavelength at the center of the µLED samples as a function of the µLED area.

relaxation mechanism only present in larger samples.

4.2.3 Substrate analysis

In our effort to understand the source of the emission heterogeneity in our LED samples, we postulated that the source of different behaviors between seemingly identical samples could be related to differences in the non-doped, or intrinsic, GaN layer (shown in figure 13 as i-GaN). Therefore, we proceeded to analyze that region of the µLED samples.

To study the intrinsic GaN layer, we used spatially resolved cathodoluminescence once again. The same acceleration voltage of 10 kV was used, as it was high enough to reach the i-GaN layer, according to CASINO simulations, while maintaining an adequate spatial resolution. A diagram showing the results of simulations performed by Sylvain Finot of two different penetration volumes in the LED structure can be seen in figure 17 e). Our own simulations yielded similar results.

GaN has a direct energy bandgap of approximately 3.4 eV [8], which corresponds to a wavelength of roughly 365 nm. Hence, we performed spatially resolved CL, mapping the relative intensity of the GaN peak in multiple µLED samples.

These measurements showed that darker LED samples had a tendency to have spots in which

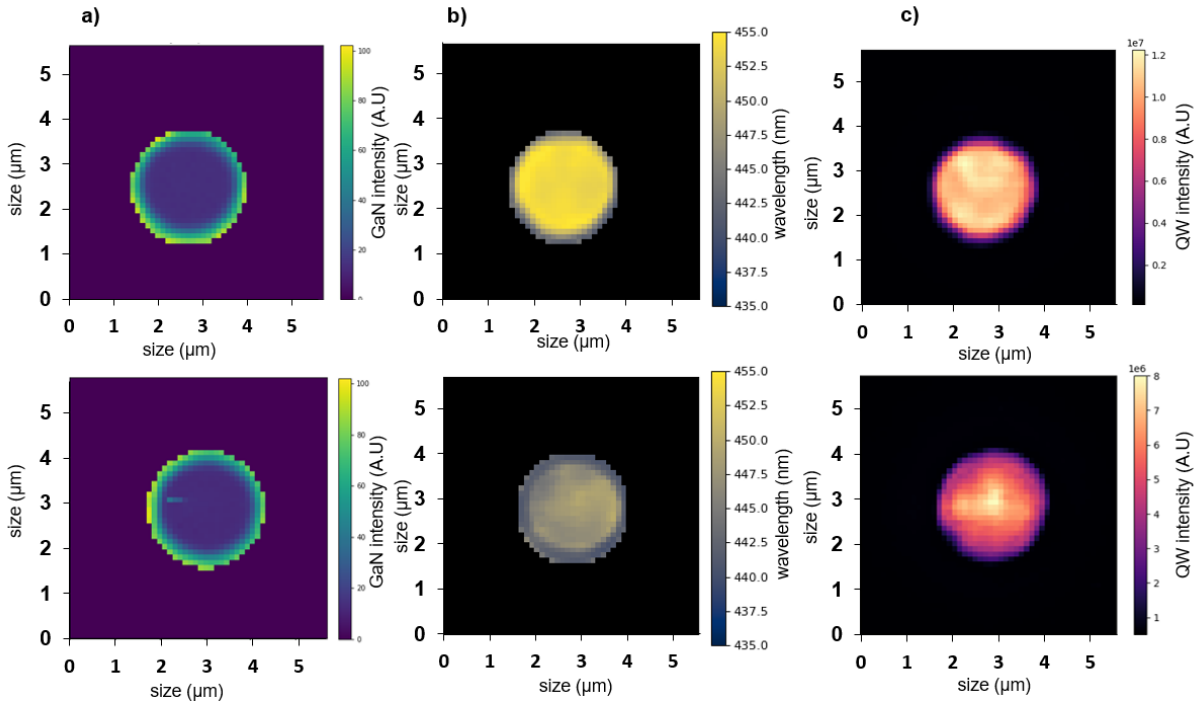


Figure 21: a) CL Intensity of the GaN peak, b) CL emission wavelength of the LED quantum well and c) CL emission intensity of the LED quantum well for a (top) hight brightness sample and a (bottom) low brightness sample. We can see a small area of higher CL GaN emission in the low brightness sample, on the left side of the sample.

the intensity of the GaN peak under CL was enhanced. Hence, it appears that the cause of the intensity loss for some LED samples could be related to the presence of spots with higher GaN concentration.

Figure 21 shows two of these measurements, on a high brightness and a low brightness sample. The low brightness sample displays a small spot with higher GaN CL intensity on its left side. Similar spots were found in all low brightness samples, which led us to believe that the change in intensity was related to local increases in the concentration of intrinsic GaN. We will discuss how these points can be explained by V-pit concentration in section 4.3.

4.2.4 Low temperature measurements

In order to study the effect of temperature on the diffusion length of carriers, we decided to perform low temperature CL measurements on the µLED samples. The cryogenic stage described

in section 3.2 was set at 30 K. The procedure was otherwise identical to room temperature measurements.

The first notable difference between the room and low temperature measurements is a significant redshift on the colder samples, with an average emission energy difference of 4.2 meV (0.7 nm increase in wavelength) between the two temperatures. This redshift is caused by carriers relaxing into lower energy states at lower temperatures. These lower energy states are also more localized, leading to a much lower diffusion length [69].

Notably, the average wavelength is much more stable between samples at low temperature, with the standard deviation of the average energy emission an order of magnitude lower that at room temperature. Defect states are frozen at low temperature [70], which supports our argument that the wavelength emission heterogeneity is caused by V-pit defects. As will be discussed in section 4.3, these defects cause the observed blue-shift at room temperature. Hence, this defect freezing effect may explain why low temperature samples are red-shifted and much more homogeneous.

Another effect of the lower temperature on the µLED emission was an increase in emission intensity. This appears to be due to two reasons: Firstly, the defect-freezing effect of low temperature increases the emission intensity, as there are less nonradiative decay paths for e-h pairs. Secondly, the effect of surface recombination is greatly reduced at low temperature.

The reason for the decrease of surface recombination in low temperature samples is the much lower carrier diffusivity [71]. This lower diffusivity means e-h pairs cannot travel to the surface to decay nonradiatively, and are more likely to emit a photon. This effect can also be appreciated in the lifetime of the sample.

Figure 22 shows two samples, at high and low temperature, and a mapping along a line of their surface. The line mappings were done to improve the resolution over spatial mappings, allowing for closer points in a reasonable time frame. In order ensure we captured the full range of the LED, the extremes of the line were place slightly outside the LED. As a consequence, the figure also shows estimated lifetime of those external points. However, the signal at those points is mainly noise, so the lifetime at those points is meaningless.

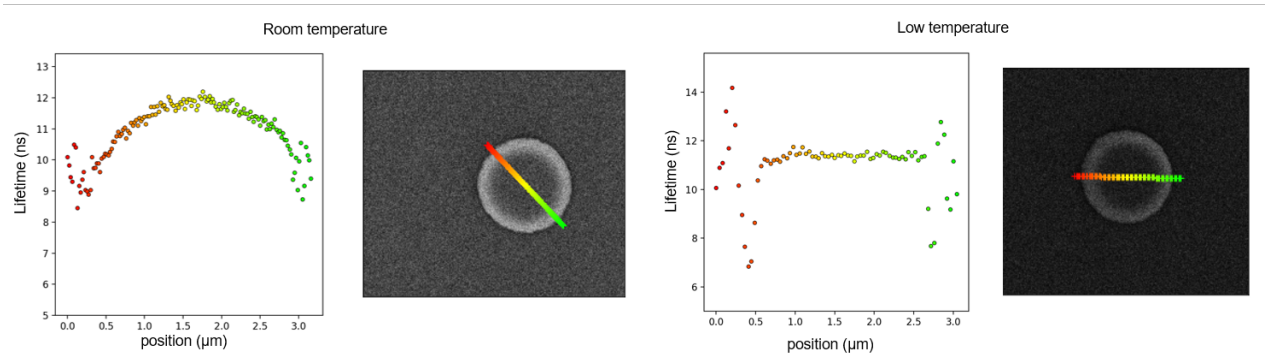


Figure 22: Comparison of lifetime along a line between a room temperature (left) and a low temperature (30 K) (right) 2.5 µm circular LED. The colors in the line on the SEM images match those on the plot for each point. Acceleration voltage was 10 kV and beam current 14 pA. Lifetime in both samples was estimated from the autocorrelation function obtained from HBT measurements.

Figure 22 clearly illustrates how the lifetime of room temperature samples decreases close to the edges of the samples, as e-h pairs created there can recombine using the edge. For a sample of the same size at low temperature, there is no lifetime loss at the edge, as the low carrier mobility prevents even very close e-h pairs from reaching it. This result shows the strength of the localization effect at low temperatures in LEDs, and demonstrates that the intensity loss observed at the edge is indeed caused by surface recombination of carriers.

4.3 Analysis of LED results

4.3.1 Emission spectra and interference pattern

When observing the emission spectra in more detail, there appeared to be two peaks with different energies contributing to the total luminosity. Figure 23 a) illustrates this by showing the spectra of a 4 µm circular LED, separating the contributions of the center and the edge of the sample. From the figure, it appears that the effect of the edge is simply to increase the ratio of the higher energy peak.

Emission in LEDs is usually modeled as a Gaussian peak [72]. Hence, it seemed logical to

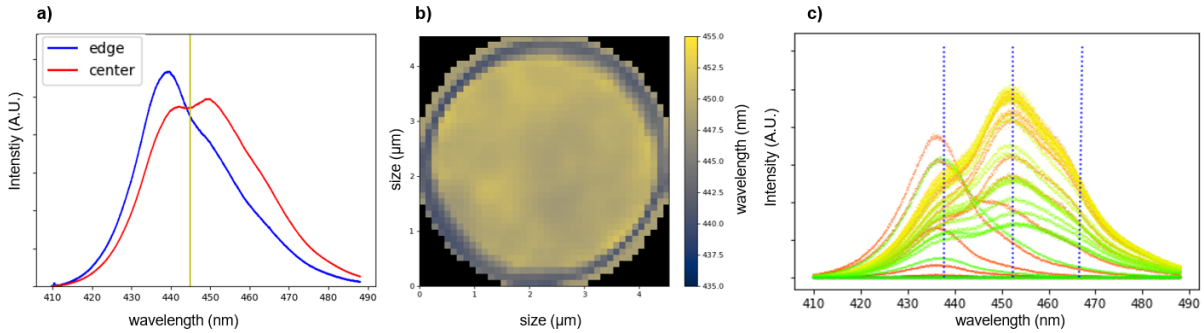


Figure 23: a) Combined CL spectra at the center and edge of an LED sample. b) spatial mapping of the average wavelength for the same LED sample as a). c) Spectra of 40 randoms points extracted from different LEDs. red and green colors indicate proximity to the edge of the sample, while yellow indicates proximity to the center.

attempt to model the emission spectra as a combination of two Gaussian peaks. However, when attempting to fit the data accordingly, this model did not work well, with an error rate of about 20%.

We tried multiple alternatives in order to find a good theoretical model for the CL and PL spectra. In the end, we found that the best model, with an error less than 5 % was as follows: A single peak with a variable position (to account for the strain relaxation shift) and the interference effect corresponding to the reflection of photons in the GaN/Sapphire interface.

Figure 23 c) shows the spectra at 40 randomly chosen points from different µLED samples, as well as the interference maxima for the GaN/Sapphire interface (blue dotted lines), showing that the maxima of the spectra correspond to interference maxima. This model also provided us with a way to measure the total width of the GaN structure, as the position of the maxima informs us of the difference in optical path lengths between direct and reflected photons. Based on this calculation, we estimate the thick n-doped GaN layer described in section 4.1 has a thickness of 2100 nm.

We tested a model with both two peaks and GaN/Sapphire interface interference, but the improvement on the fit was minimal, despite almost doubling the fitting parameters. Based on these results, we attribute the two peaks shown in figure 23 a) to the interference between direct photons, and those reflected in the GaN/Sapphire interface, as it is the physical model

that better matches the data.

4.3.2 V-pits as the source of µLED heterogeneity.

The key question we need to answer in order to understand the LED behaviors we have observed is the origin of the dark spots detected in CL. As figures 16 and 19 show, these dark spots do not impact the lifetime, and therefore they can not be directly related to the µLEDs internal quantum efficiency.

As per the discussion in section 4.2.3, these dark spots correlate to an increase in pure GaN emission. This led us to believe that the loss of intensity could be related to excitation efficiency. Particularly, our electron beam was creating more e-h pairs in the GaN than in the quantum well in certain regions.

The reason why e-h pairs were not being created in the QW could be related to the structure of the µLEDs. Hence, we proceeded to study said structure. Nicolas Bernier and David Vaufrey, collaborators of Corentin Le Maoult had already performed scanning transmission electron microscope (STEM) imaging of 80 nm vertical cuts of the µLEDs sample, which we proceeded to examine in detail.

An example of said cut can be seen in figure 24. The cut shows four structures know as V-pits. V-pits, sometimes called inverted pyramids, are a type of defect that forms around a dislocation. As figure 24 shows, the dislocation causes spiral growth, drastically affecting the heterostructure in the vicinity of the dislocation, and giving the defect its characteristic V shape [73, 74].

The density of the V-pits was not uniform, with all of the V-pits concentrated in one half of the mesa. Figure 24 is a zoom in on this area of interest, to better display the effect of V-pits on the heterostructure.

As proposed by Hangleiter *et al.* [75], V-pits create an energy barrier around the local defect. Although the dislocation creates a non-radiative decay path, e-h pairs generated outside the V-pit can not reach it due to this potential barrier. Meanwhile, e-h pairs created directly in

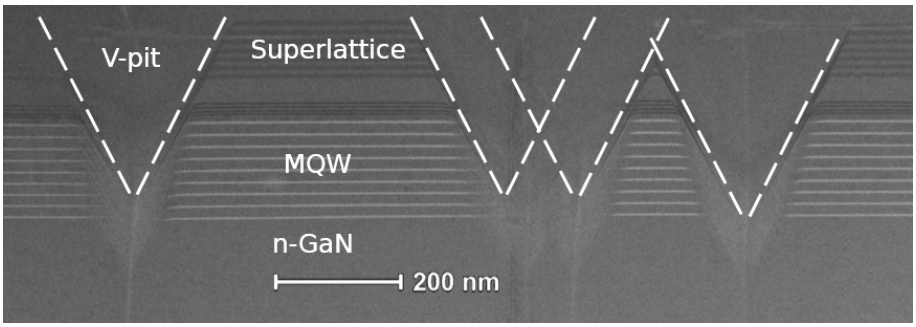


Figure 24: STEM image of a vertical cut from one of our µLED pixels. Detail on the measurement conditions can be found in [60]. The studied mesa is a 2.5 µm square. Sample was prepared with focused ion beam etching to obtain a width of 80 nm. Four V-pits can be seen in the active region.

the V-pit almost instantaneously recombine non-radiatively on the dislocation [74] and do not contribute to emission intensity.

The behavior expected from V-pits perfectly matches our previous observations:

- Electron-hole pairs created inside a V-pit decay nonradiatively via the defect, causing CL emission to be less bright at their position. Since e-h pairs inside V-pits do not emit photons, they do not influence the local carrier lifetime we can measure, as we are limited to measuring the lifetime of states that can emit light. This explains the dark spots with no effect on the lifetime shown in figure 16, and the lack of correlation shown in figure 19.
- The extra intensity of the GaN substrate detected on the darker samples can be explained by the structure of V-pits observed in figure 24. V-pits disrupt the layer growth, causing GaN inverted pyramids to form at the depth the quantum wells would normally be. Hence, we detected a higher concentration of GaN in darker LEDs, which have higher V-pit density.
- The correlation between wavelength and intensity observed in figure 20 can also be explained by different concentrations of V-pits between samples. It has been observed by Chen *et al.* [76] that V-pits can alter the emission properties of LEDs during operation, with wavelength decreasing as total V-pit surface increases. V-pits cause strain relaxation [77], which could cause a blue-shift in the surrounding QW emission, similarly to the edge.

These properties match our observations, supporting the role of V-pits in the CL intensity

variation. Pixels with a larger V-pit concentration are blue-shifted, as shown by [76], and their total intensity is lower, due to their detrimental effect on excitation efficiency, since e-h pairs created inside a V-pit do not contribute to intensity, as per [74], explaining the correlation seen in figure 20 a).

Hence, we believe that the origin of the sample to sample differences in intensity and wavelength emission is the relative concentration of V-pits inside different LEDs. Samples with more V-pits are less bright and have their emission blue-shifted. As figure 20 b) shows, smaller samples have a much higher variation in both intensity emission. The reason appears to be that the variation in the amount of V-pits will be naturally larger in smaller µLEDs, as we are considering a smaller area.

To test this hypothesis, we needed to calculate the density of V-pits and their average size. In order to do this, we used the PhotoMultiplier Tube described in chapter 3.2. The PMT enabled us to quickly image the emission in the QW wavelength range. By imaging a series of micrometric rectangles in a large non etched region of LED, we obtained a series of images that clearly showed dark spots corresponding to V-pits. Figure 25 shows one of these images.

Rather than count the number of V-pits manually, we wrote a python program that would count V-pits by detecting areas with low intensity and a circular shape. The red dots in figure 25 correspond to the center of the V-pits detected by the program. The density of V-pits calculated by this method was $7.6 \pm 0.1 \cdot 10^8$ V-pits per cm^{-2}.

This density is higher than previous reports for the expected V-pit density of InGaN LEDs grown on sapphire, of $1.5 \cdot 10^8/cm^2$ [78] and $3 - 5 \cdot 10^8/cm^2$ [79]. However, as observed by [80], the amount of V-pits grows with the number of layers, so that discrepancy could be explained by the presence of an underlayer. As observed on the STEM images, the V-pits cannot be counted by high resolution SEM nor atomic force microscopy due to the conformal growth of the p-GaN layer.

The smallest pixels have a surface of about 1 $\mu\mathrm{m}^2$, so they will contain 7 V-pits on average. Therefore, the number of V-pits per µLEDs may vary significantly ranging from even 0 to a few, as figure 25 shows their density is not uniform, and the pixels were etched post growth. Hence,

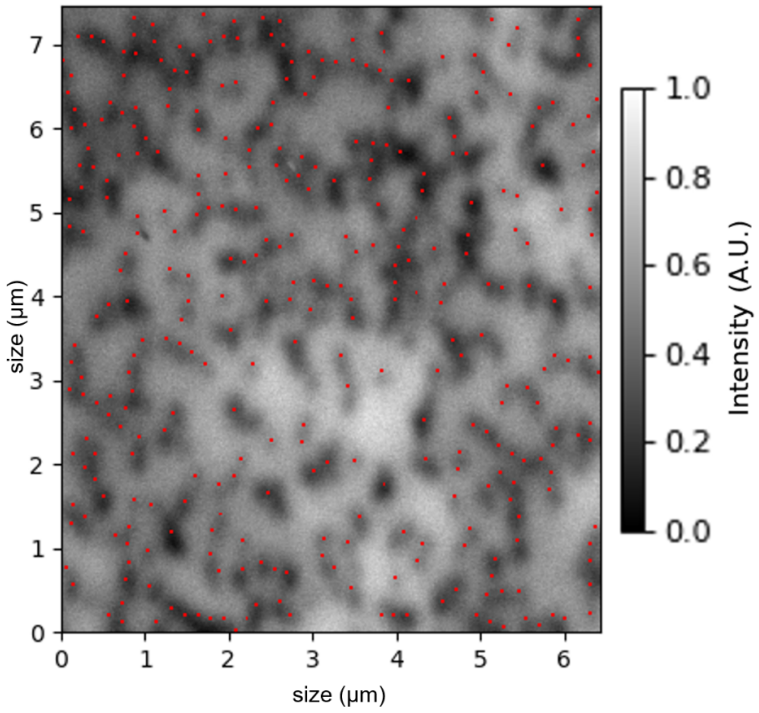


Figure 25: Cathodoluminescence spatial imaging of a non-etched region of the LED sample. Acceleration Voltage was 10 kV. image was obtained with the PhotoMultiplier Tube, for a wavelength of 450 nm, corresponding to that of the LED emission. Red dots indicate the position of V-pit, as detected using our python program.

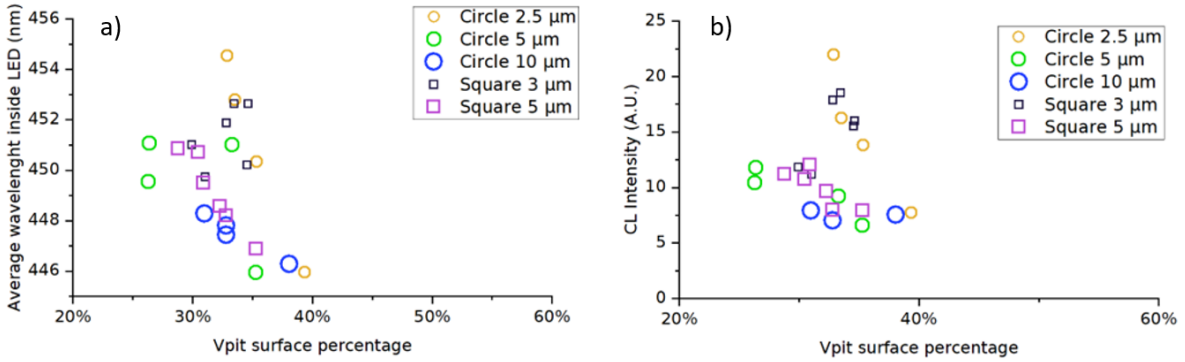


Figure 26: (a) Average wavelength and (b) CL intensity versus percentage of V-pit surface in pixel (defined as percentage of µLED pixel surface with intensity below 95% of average LED intensity).

despite a high V-pit density, it is statistically possible to obtain single µLED free from V-pits, explaining why the variance in intensity and wavelength is much larger in smaller pixels.

As a final test to the V-pit explanation for the emission heterogeneity between µLEDs, we decided to study the relationship between their concentration, intensity and wavelength. Since V-pits can have different sizes, as shown in figure 25, we decided to estimate the fraction of the total surface of the LED they represented. In order to do this we considered that a point within the CL mapping of a µLED was a V-pit if its intensity was less than 95% of the average emission of the µLED.

Figure 26 shows the correlation between this percentage and both intensity and wavelength. The smallest µLEDs were not included due to the difficulty of measuring the V-pits due to their large effect on average intensity: A large V-pit could fully cover a small sample, making the average intensity that of the V-pit. Despite this limitation, the trend is clear: Darker µLEDs are not uniformly darker, they are darker on only some parts of their surface. Similarly, blue shifted µLEDs have a larger percentage of darker regions. Both of these results match the V-pit explanation.

4.4 Energy excitation efficiency

Our observations point to the detrimental effect of V-pits in the excitation efficiency of the electron beam in the µ-LED samples. Hence, we attempted to access the excitation efficiency of our measurements to confirm these results.

The work of Magdalena Solà-Garcia *et al.* [43] outlines a method to estimate excitation efficiency of an electron beam inside a LED sample. Their method is based on the number of counts of the autocorrelation function $g^{(2)}(\tau)$ at $\tau = 0$. As we have access to the entire autocorrelation function for each measurement position thanks to the HBT measurements, we can estimate this excitation efficiency in a spatially resolved way.

It is important to note that the autocorrelation function plots number of counts as a function of time, so it will be dependent on intensity, and therefore beam conditions exposure time. To avoid this dependence, Solà-Garcia *et al.* redefined the autocorrelation function $g^2(\tau)$ as being normalized with respect to its value at very long delay ($\tau \to \infty$), *i.e.* the number of counts for uncorrelated events.

The expression for the autocorrelation function $g^{(2)}(\tau)$ at $\tau = 0$ found by Magdalena Solà-Garcia *et al.* is as follows:

$$g^{(2)}(0) = 1 + \frac{q}{I\alpha_{\mathrm{b}}}\frac{b+1}{b} \tag{4}$$

With q the electron charge, I the beam electron current, b the average number of e-h pairs created inside pair by a single inciding electron, and α_{b} the shape factor of $g^{(2)}(\tau)$ bunching peak, that is, the ratio between the peak height and its surface area.

For the case of a Super-Poissonian autocorrelation function, such as ours, the shape factor α_{b} will be related to the lifetime τ_{eff} by the expression $\alpha_{\mathrm{b}} = 2\tau_{eff}$. And as the number of e-h pairs created by a single beam electron follows a Poisson distribution, the probability of creating at least one e-h pair, *i.e.* the excitation efficiency γ follows $\gamma = 1 - e^{-b}$.

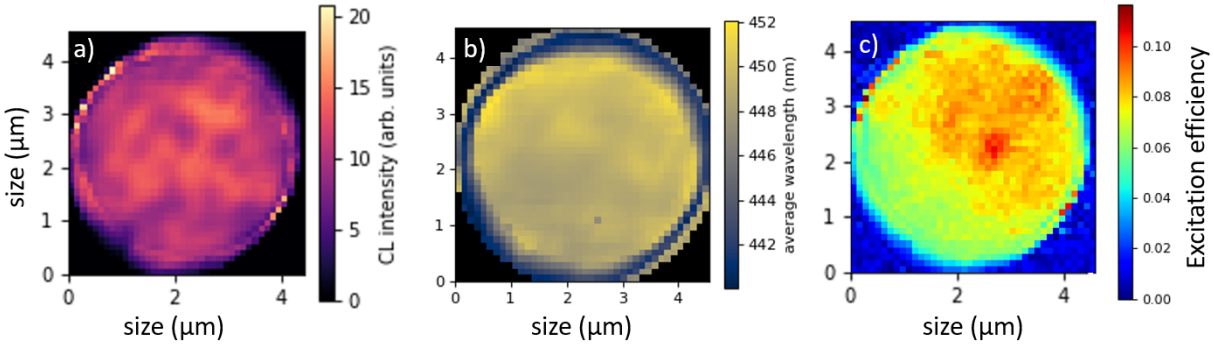


Figure 27: CL mapping of a circular 4 µm LED a) total intensity, b) average wavelength, and c) the excitation efficiency calculated using equation 6. Data is the same as figure 16.

Combining everything, equation 4 becomes:

$$b = \frac{1}{(g^{(2)}(0) - 1)\frac{I\alpha_b}{q} - 1} \tag{5}$$

$$\gamma = 1 - \exp\left(\frac{1}{1 - (g^{(2)}(0) - 1)\frac{I\alpha_b}{q}}\right) \tag{6}$$

We proceeded to calculate the spatially resolved excitation efficiency in our µLED samples using this method. An example of the results obtained can be seen in figure 27. These figure shows that the bright points at edge of the LED cause a high increase of the excitation efficiency, confirming Sylvain Finot attribution of the intensity increase to the enhanced overlap between QW and excitation volume [63, 64].

Figure 27 also shows that excitation efficiency is overall quite low within our sample. This is to be expected, since as discussed in section 4.1 the QW structure is 220 nm deep inside the sample, so for the chosen acceleration Voltage of 10 kV Figure, more than half the beam energy will be lost before the electrons reach the top QW, as can be seen in figure 15. This low total value led us to choose a rainbow colormap for the plot, in order to better appreciate the small local changes in excitation efficiency.

The high excitation efficiency pixels at the edge shown in figure 27 c) correspond to the same high intensity pixels at the edge of figure 27 a). This is consistent with the results from Finot [63], discussed in section 4.2.2 and shown in figure 17. As the electron beam impacts on the inclined edge of the mesa, the associated interaction volume intersects with a larger volume of

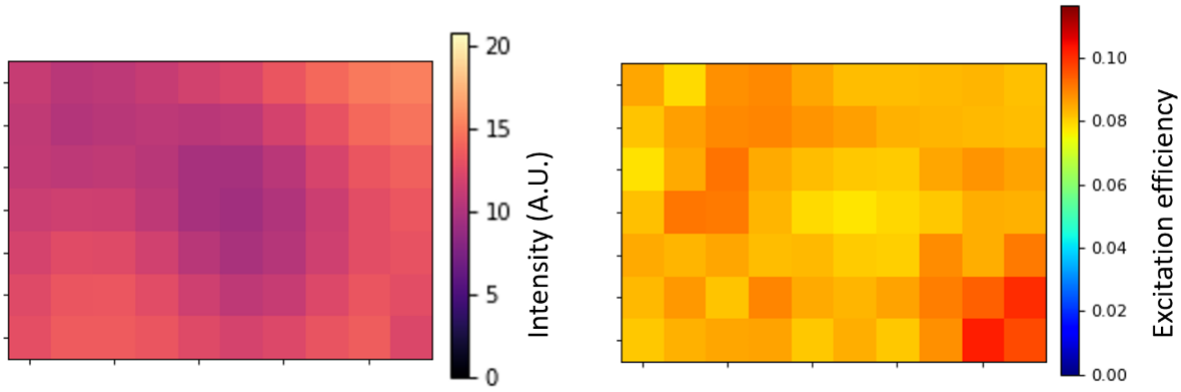


Figure 28: Zoom in on sections of figure 27 a) and c), showing total intensity and excitation efficiency in the chosen regions.

the QW, causing both intensity and excitation efficiency to increase.

Figure 27 c) also reveals that the lower left section of the LED shows a lower excitation efficiency that the rest of the sample. The cause is likely a reduction in QW width, as this area also presents lower intensity and a slight blue-shift in the average wavelength, which are both effects expected from such a small reduction in width. This effect makes it a bit more difficult to appreciate the effects of the V-pits on the excitation efficiency. Hence, figure 28 shows the excitation efficiency vs CL intensity in a certain zoomed in section of the same LED. The dark spot associated to V-pits displays a decrease in injection efficiency compared to their surroundings, as was expected.

4.5 Conclusions

Our study of the properties of a large number of differently sized µLEDs has demonstrated the strengths and weaknesses of the various experimental techniques used during the development of this PhD. In particular, we have focused on spatially resolved cathodoluminescence and derived techniques, as we realized we needed the spatial resolution provided by CL to properly understand the samples.

As for our observations in the samples themselves, we have found that light emission in can change by a factor of two between seemingly identical µLEDs. We have mapped the lifetime of multiple pixels and found no correlation within single µLEDs between lifetime and intensity.

This points out to a significant variation in either extraction or excitation efficiency within individual pixels. The source of this variation has been attributed to differences in the number of V-pits between samples.

Between different µLEDs, variations in intensity were correlated with a change in wavelength at the center of the pixels, with less bright µLEDs blue-shifted. This blue-shift has also been attributed to the increased concentration of V-pits due to its negative correlation with CL intensity. This matches previous observations on the effect of V-pits on emission wavelength. Smaller samples had a higher range of possible values for intensity, lifetime, and red-shift, which has been attributed to the larger expected variance on the amount of V-pits.

V-pits are usually considered a desirable defect for large nitride LEDs [81]. First, they do not affect the EQE because of the potential barrier between the active region and the dislocation. Second, they can even improve the wall plug efficiency by lowering the forward voltage in InGaN/GaN LEDs due to lateral hole injection [82]. In contrast, our results show that, for µLEDs, V-pits can induce a color and intensity variation from sample to sample, which may be caused by strain relaxation. For the smallest size studied, 1 µm, a large V-pit can cover the surface of the LED in its entirety. This represents an issue for applications that require very small LEDs, such as virtual reality headsets, as we have shown the effect of V-pits for those pixels sizes causes a significant heterogeneity in emission wavelength and intensity.

5 Cathodoluminescence temperature sensing in bulk diamond

5.1 Introduction

One of the main reasons that led us to use nanodiamond as a cathodoluminescence temperature probe was the previous success of CL based thermometry on bulk diamond [83], including some of our previous work in the form of a master's thesis.

There are significant differences between the characterization and application of bulk and nanodiamond thermal sensing. Mainly, since diamond is such an excellent thermal conductor, the temperature will be very homogeneous alongside the entire bulk material, making spatial resolution less of a priority.

This homogeneity in temperature may appear counterproductive to our goal of high spatial resolution. However, the stable temperature will make temperature characterization easier in bulk diamond than in nanodiamond. Bulk samples are also much more homogeneous than nano samples, which leads to better spectral stability. These properties made bulk a logical starting point for characterization.

Apart from being easier to perform than in nanodiamond, CL sensing in bulk diamond has value as a characterization technique in its own right, as it allows to set the penetration depth, which is useful to characterize synthetic diamonds with different growth layers. There are also some valuable insights that can be gleamed from comparing the CL spectra of bulk and nano diamond.

For all these reasons, we will discuss our CL results on bulk diamond in the next section. We will dedicate special attention to a spectral feature called the Nitrogen-Vacancy defect, and we will discuss its physical structure in more detail.

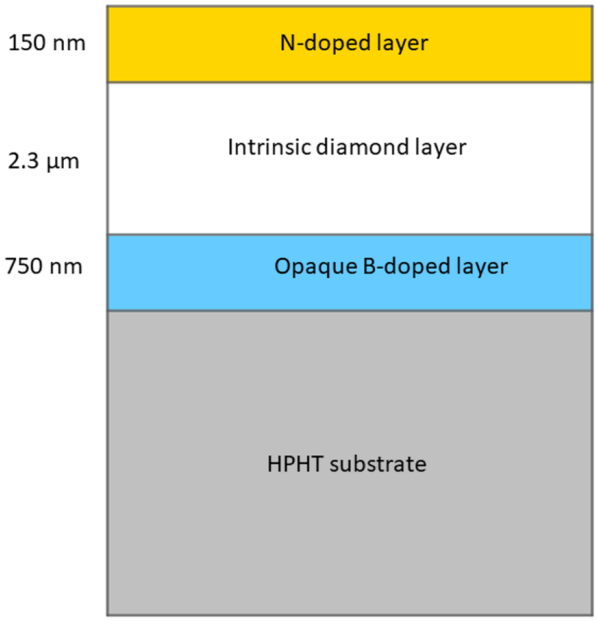


Figure 29: Structure of the bulk diamond sample used for this study. Sample has been provided by the company DIAMFAB [84]. Samples were grown on top of a HPHT diamond, using MPECVD, with CH_4 and N_2 as precursors.

5.2 Bulk diamond sample

The bulk diamond sample studied was provided by the company DIAMFAB [84]. Its structure can be seen in figure 29. As the figure shows, the top nitrogen-doped layer, with a width of 150 nm, sits on an intrinsic diamond layer of 2.3 µm, which is separated from the high pressure high temperature (HPHT) substrate by a boron-doped layer with a width of 750 nm.

The samples were grown using microwave plasma-enhanced chemical vapor deposition (MPECVD), with CH_4, B_2H_6 and N_2 as precursors. The diamond was grown on the plane (100) of a HPHT diamond substrate, leading to a single crystal structure.

The purpose of the opaque layer is to block any potential contribution from the HPHT substrate, ensuring that only the light emitted by the MPECVD layer is studied. The intrinsic layer exist to prevent potential Boron contamination in the Nitrogen doped layer.

The CL measurements on the bulk diamond were performed with an acceleration voltage of 10 kV, which leads to a penetration depth of about 0.5 µm, as seen in figure 6, from section 3.1.

Hence, we are only studying the intrinsic and N-doped layers.

The Nitrogen doping was used to introduce atomic defects in the diamond lattice, in order to study the associated peaks in CL and their evolution with temperature, particularly the Nitrogen-Vacancy center, a structure discussed in more detail in section 5.4.

Despite the fact that no silicon precursors were introduced, silicon-related impurities were detected during the CL measurements. These impurities come from the interaction of the plasma with the chamber walls, which are made of quartz. The plasma damages the quartz, extracting silicon ions that deposit in the sample. The issue is compounded by the fact that silicon atoms inserted in diamond are very stable, to the point that uncontrolled silicon impurities are a well documented issue when synthesizing diamond via CVD [85].

5.3 Cathodoluminescence spectroscopy results on bulk diamond

CL measurements were performed in two separate regions, from 200 to 350 nm using the 1800 gr/mm grating; and from 350 to 800 nm, using the 600 gr/mm grating. As mentioned in section 3.2, the former grating is only adequate for short wavelengths, therefore we used it when possible to increase spectral resolution.

The CL measurements were performed for a temperature range of 5-300 K. It is important to note that, as discussed in section 3.2, the real minimum temperature is actually above 5 K due to the black body radiation emitted by the mirror. The CL spectrum at 5 K can be seen in figure 30. The spectra for all the temperatures studied may be found in figure 31.

As shown in figure 30, the main features of the spectra from higher to lower energy are the 389 nm peak, the TR12 peak, two CVD related peaks, the H4 peak, the 533 nm peak and its replicas, the NV0 peak and its replicas, and the SiV- peak.

We will discuss our analysis of these peaks in the following sections, with special attention given to the NV0 peak.

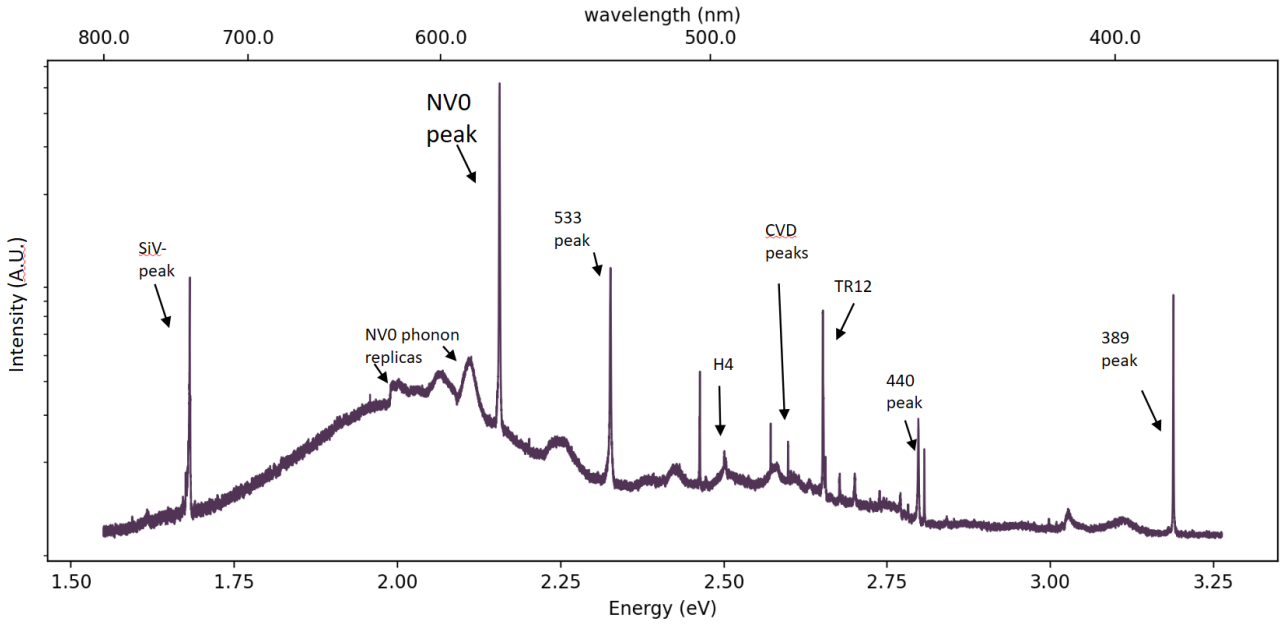


Figure 30: Visible cathodoluminescence spectrum of CVD grown bulk diamond with nitrogen doping at 5 K. The intensity axis used a logarithmic scale. Measurements were done by irradiating a single point with the SEM electron beam. The acceleration voltage was kept to 10 kV and the exposure time was 5 s.

5.3.1 389 nm peak

The origins of the 389 nm peak are currently unknown. The peak appears after nitrogen implantation in all species of diamond, but also after radiation damage [86]. The peak is uncommon in non doped, CVD diamonds, appearing in only 7% of samples [87], and its entirely absent in HPHT grown diamonds [88]. Oddly enough, despite not appearing in natural diamonds with no nitrogen, the 389 nm peak is more intense in diamonds with lower concentration of nitrogen impurities [86]. Even more strangely, the peak does not appear at all in the photoluminescence spectra of diamonds were the nitrogen impurities are very close together [89].

Figure 32 shows the temperature evolution of the 389 nm peak CL spectra for our bulk sample.

The full width at half maximum of the 389 nm peak was observed to grow at a predicate, albeit slow, rate. This means the peak is a potential candidate for temperature sensing. However, its relative low luminosity, unknown origin, and low rate of change made us not focus on this peak,

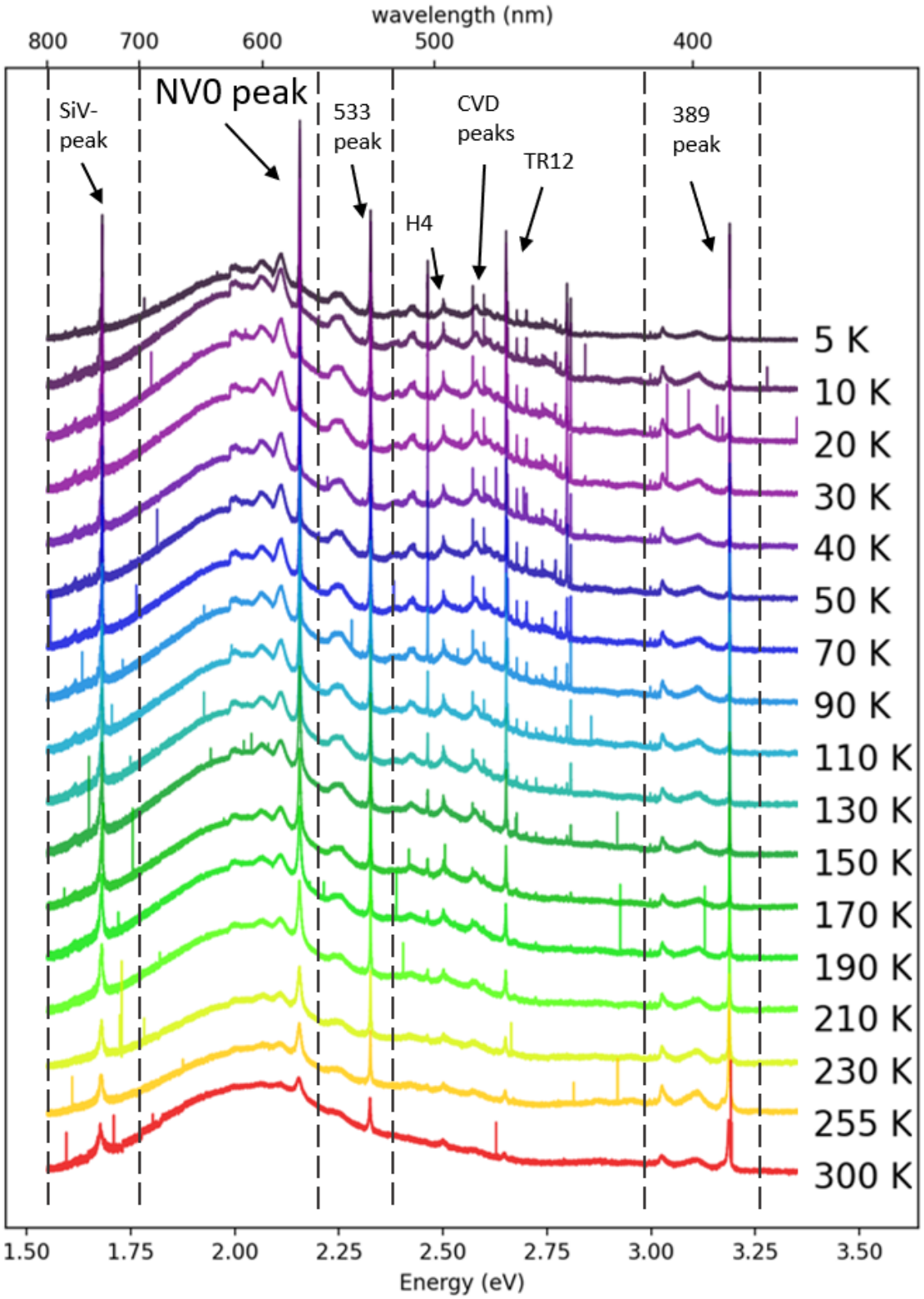


Figure 31: Visible cathodoluminescence spectra of CVD grown bulk diamond with nitrogen doping for all measured temperatures. The intensity axis used a logarithmic scale. Measurements were done by irradiating a single point with the SEM electron beam. The acceleration voltage was kept to 10 kV and the exposure time was 5 s.

as we found better options.

5.3.2 440 nm radiation peak

The small peak at 2.81 eV, or 440 nm, is a radiation damage peak usually associated with nitrogen doping [90]. The intensity of the peak is weak, and its size and shape is constant until it quickly disappears at 170 K.

As the peak itself is created by the beam, its characteristics will likely depend on the electron beam properties and exposure time. Since the peak itself is only present a low temperature, has no clear temperature dependence, and its properties may change during a measurement, it was quickly discarded as a temperature sensor.

5.3.3 TR12 peak

The TR12 is a peak at 470 nm caused by radiation damage [86], hence it was likely caused by the exposure of the sample to the electron beam. The peak is suppressed by hydrogen defects [91], so its presence may indicate a lack of hydrogen impurities in the sample.

The intensity of the peak appears to decrease with temperature, but since the peak is created by the beam, it is subjected to the same limitations as the 440 nm peak. This potential unreliability, alongside the peak small intensity and low temperature dependence made us discard it.

5.3.4 CVD peaks

The two sharp peaks at 477 and 482 nm are a common occurrence in CVD grown bulk diamond, although their exact origin is currently unknown [92].

The shape and intensity of the peaks are very stable with temperature, until their signal quickly vanishes between 150 and 170 K. Low change and unknown physical origin compound to make the CVD peaks very poor candidates for temperature sensing.

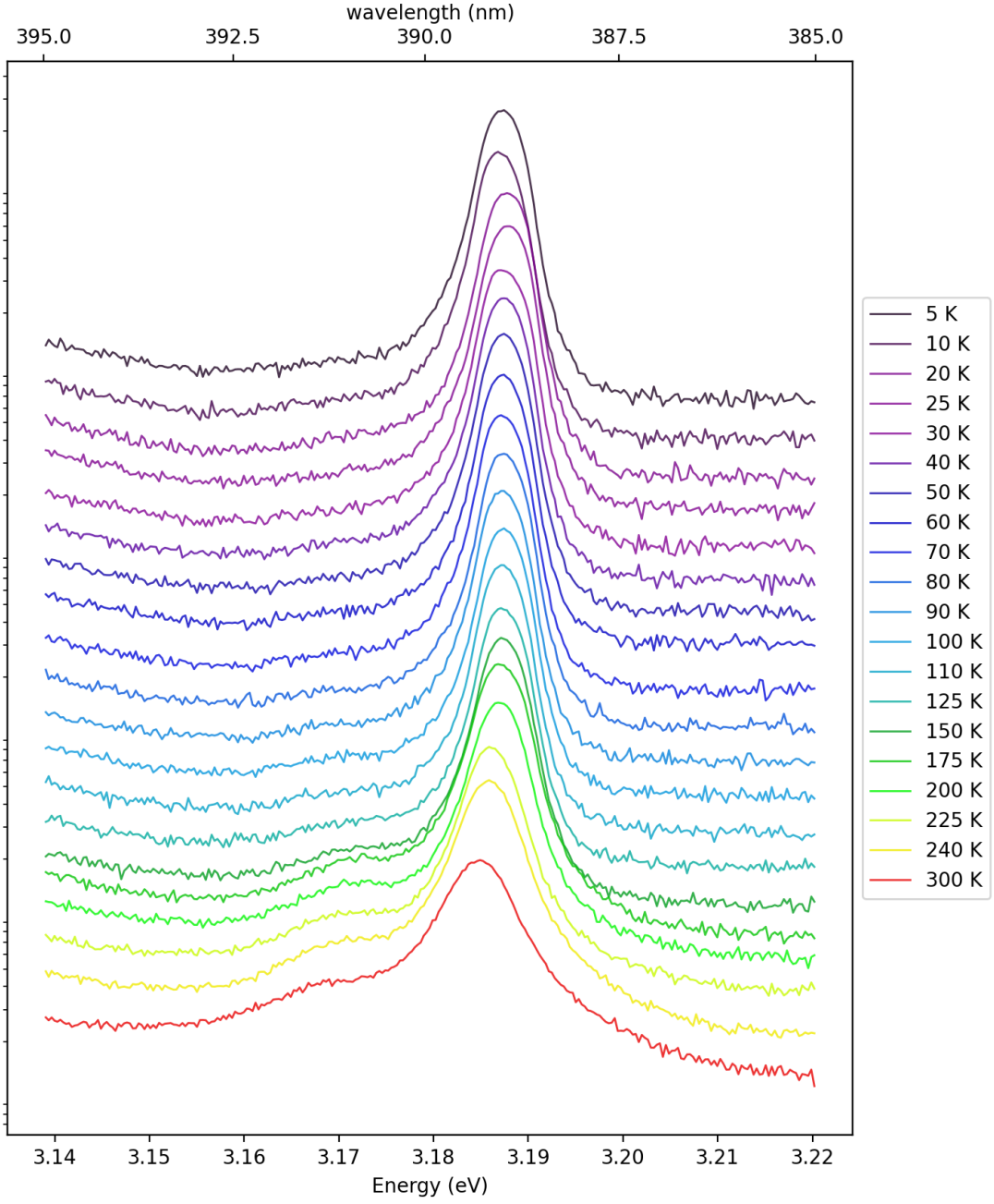


Figure 32: cathodoluminescence spectra of 389 nm peak in CVD grown bulk diamond for multiple temperatures. The intensity axis used a logarithmic scale. Measurements were done by irradiating a single point with the SEM electron beam. The acceleration voltage was kept to 10 kV and the exposure time was 5 s.

5.3.5 H4 band

The peak at 496 nm is attributed to the H4 band. The band loses intensity as the temperature raises, and almost disappears at room temperature. The bands is attributed to radiation damage [86], and its formation has been observed to be enhanced by the presence of both Nitrogen defects [93] and vacancies [94]. The bands have a series of phonon replicas, stretching all the way to 530 nm.

The H4 band has extremely low intensity, making it hard to detect and even harder to fit to a model. Furhermore, its shape appeared to be stable with temperature, with the intensity being the only parameter that evolved. Hence, the H4 band was discarded as well.

5.3.6 533 nm peak

Similarly to the 389 nm peak, the 533 nm peak does not have a known origin. It has been observed that the peak is almost exclusive of CVD grown diamonds [86], but is only present in 16% of these types of samples [87]. Multiple authors have postulated that the peak origin is related to a nitrogen associated defect, similarly to the 389 nm line [86, 95, 96]. However, it has also been proposed that the line is caused by boron defects [97]. The 533 nm line is usually accompanied by a second line at 531 nm, except in perfectly homoepitaxial samples [96], such as ours.

The evolution of the peak was studied by fitting its shape to a Voigt profile. Unlike most peaks, its width became slightly smaller with temperature, up until 150 K, at which point it started to grow. Overall, the variation in the peak shape was small below 250 K. The intensity of the peak is about the same as the 389 nm peak at low temperature, but it becomes much lower at room temperature. The peak FWHM versus temperature can be seen in figure 33.

The peak only displays significant temperature sensitivity in a region were it intensity is too weak for good accuracy, and has no known origin or method to ensure its presence. For these reasons, it was ultimately discarded as a potential temperature sensor.

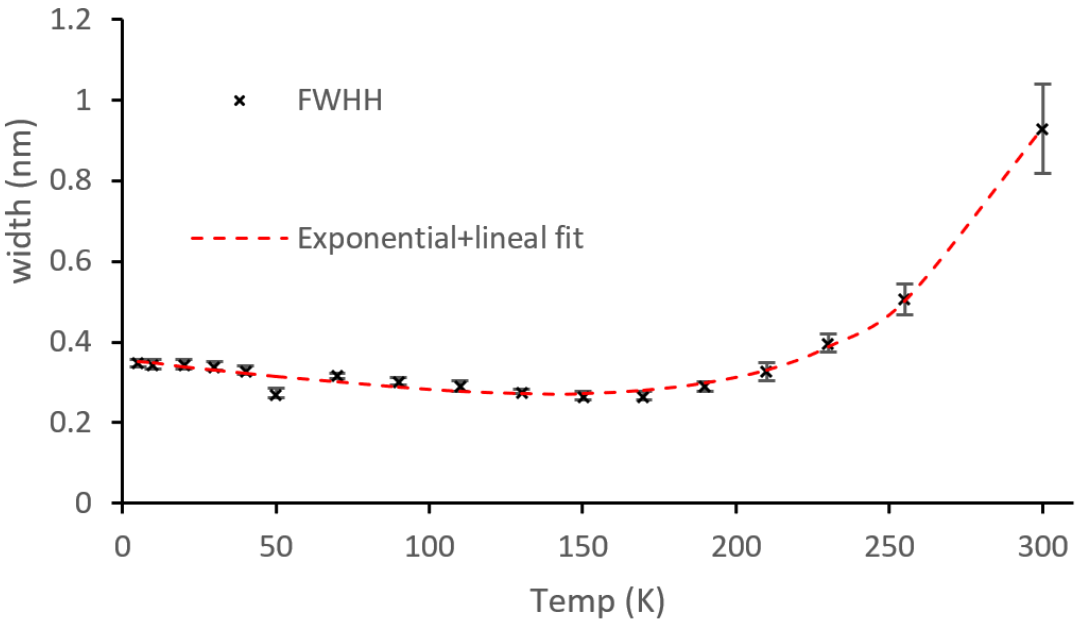


Figure 33: Full width at half maximum of the 533 peak in bulk diamond and associated exponential+linear model. The parameter was estimated using the Voigt fit, and J.J. Olivero and R.L. Longbothum [98] approximation. Dataset is the same as figure 39.

5.3.7 SiV peak

The silicon-vacancy center, or SiV^- is a diamond lattice defect that appears when a pair of adjacent carbon atoms in the diamond lattice are substituted by a single Silicon atom. We can see an example of this structure in figure 34.

As discussed in section 5.2, these silicon defects were not intentionally introduced during growth, but are the result of the plasma precursors interacting with the quartz in the growth chamber and extracting silicon ions that are incorporated in diamond. Despite being unable to control their concentration, silicon defects produce a bright peak, so we decided to study their potential for thermal sensing nonetheless.

The SiV^- defect breaks lattice symmetry, and causes a strong localisation of phonons and electrons. This localisation causes the SiV^- center to behave similar to a molecule, with excited and ground states that lead to light emission.

The SiV^- center has the symmetry of a D3d point group. This symmetry produces an electronic

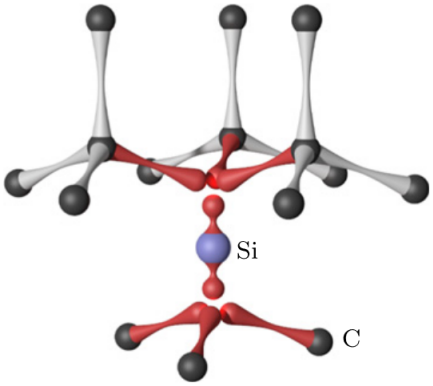


Figure 34: Molecular structure of a silicon-vacancy centre in diamond. Source: [99].

structure with two ground states and two excited states [99]. The energy split between excited and ground states corresponds to a wavelength of roughly 737 nm. Radiative transitions will happen between excited and ground states, which means there are four possible transitions that will lead to a 4-peak fine structure.

These states and transitions are represented in figure 35, alongside their associated peaks in our spectra. It has been observed that transitions C-D are much more common, due to a larger electronic population in level $|e^u_-\rangle$ [100]. The reason for this larger population is the dynamic Jahn–Teller effect, which allows for nonradiative decay from $|e^u_+\rangle$ to to $|e^u_-\rangle$ [99].

In our particular sample, the peaks associated to transitions A and B have an intensity 30 times lower than transitions C and D, to the point they are hard to separate from background noise. Hence, we will focus exclusively on the C-D transitions.

Figure 36 shows the evolution of these peak with temperature. Like the 533 nm peak, the C-D peaks full width at half maximum have been observed to grow with temperature, likely due to thermal broadening. Thermal broadening is caused by the wider energy distribution of carriers at higher temperatures, causing photons emitted to display a larger wavelength range. Above a certain temperature threshold (100 K), the fine structure becomes impossible to resolve, and the C-D transitions merge in a single peak.

It has been observed by C. D. Clark *et al.* that the peaks associated to the C-D transitions can be used as a temperature sensor below this 100 K mark, by using the ratio between the two

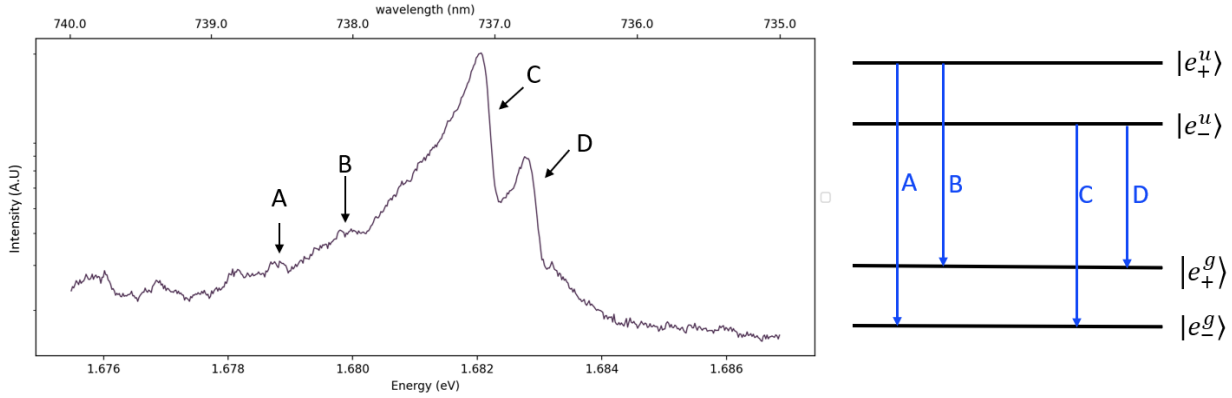


Figure 35: Left: CL spectrum of Silicon vacancy peak at 20 K for our bulk diamond sample. Peaks are labeled according to their transition.
Right: Energy levels and radiative transitions for electrons in a silicon-vacancy center. Transitions are labeled A-D from highest to lowest energy.

peaks intensities [101]. However, because we are also interested in higher temperatures, we will study the evolution on the defect emission above this value, when the transitions C and D merge into a single peak.

The position of the merged peak grows with temperature in a predictable cubic relation above 150 K. Below this temperature, peak position variation is virtually zero. Hence, the peak position has potential applications, but only above 150 K.

The width of the single peak was also observed to grow predictably: By fitting the peak to a Voigt profile (a function described in more detail in section 5.5), we could extract its full width at half maximum, or FWHM.

This FWHM grows exponentially up to a saturation point at around 220 K. For a value to be a good temperature sensor, it has to change predictably and meaningfully with temperature, so the FWHM of the SiV^- is best suited for estimating temperatures in the 150-200 K range, as the change is too low below this temperature.

Overall, the SiV^- peaks showed some promise as temperature sensors, but were outclassed by the two peaks we will proceed to discuss in more detail: The NV0 peak, and the phonon-assisted exciton peaks.

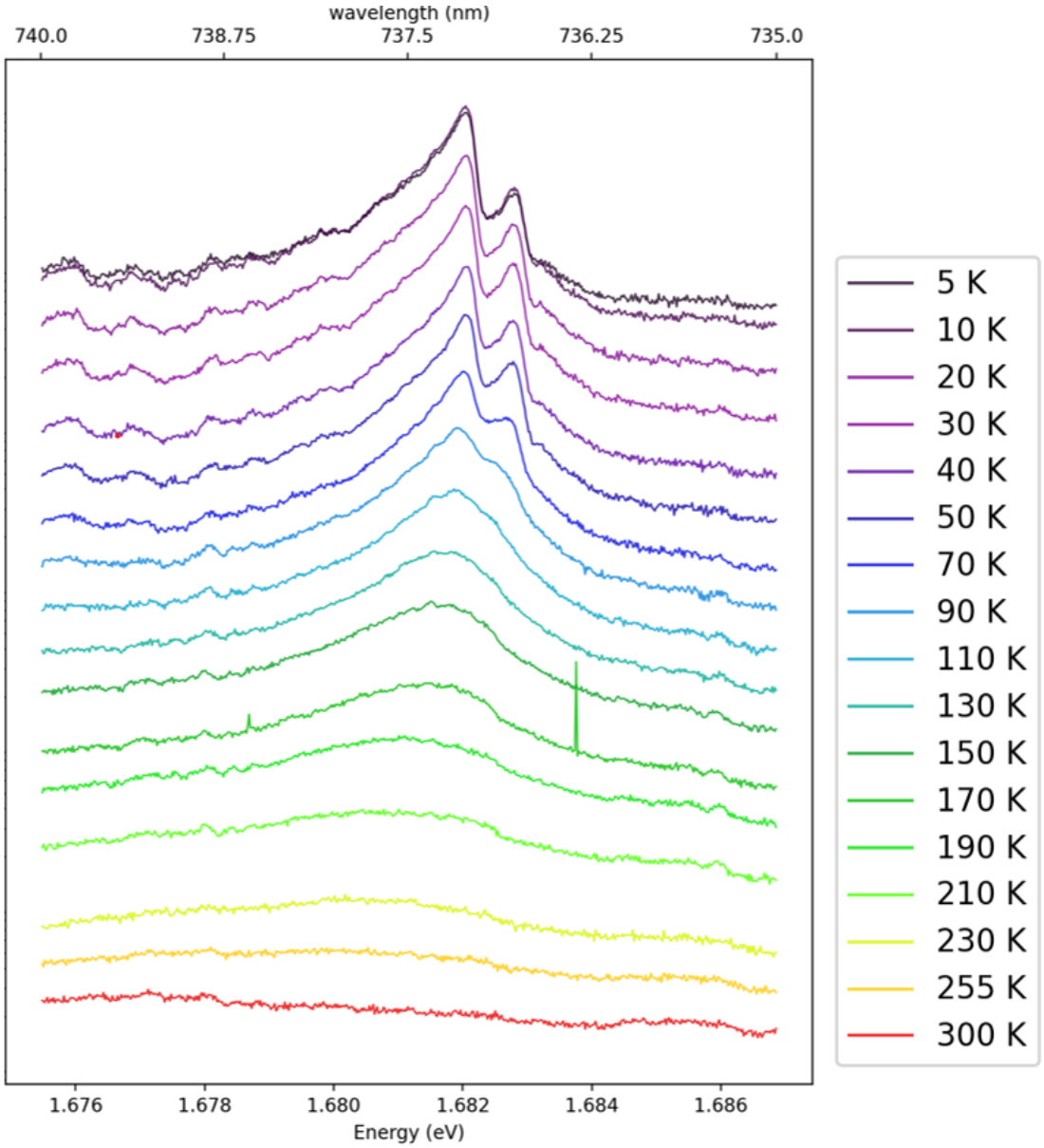


Figure 36: cathodoluminescence spectra of SiV peak in CVD grown bulk diamond for multiple temperatures. The intensity axis used a logarithmic scale. Measurements were done by irradiating a single point with the SEM electron beam. The acceleration voltage was kept to 10 kV and the exposure time was 5 s.

5.4 The Nitrogen-Vacancy color center in diamond

The main feature of the spectra owes its name to the neutral Nitrogen-Vacancy or NV0 color center of diamond, from which it originates. Before discussing the characteristics of the associated peak, we will give an overview of the structure and properties of this type of defect.

The Nitrogen-Vacancy (NV) color center is a type of defect in diamond formed by the nitrogen substitution of a carbon atom in the diamond lattice adjacent to a vacancy, as seen in figure 37. The nitrogen atoms can be introduced directly during diamond growth using N_2, or post growth via nitrogen ion implantation.

To form NV centers, a process known as annealing is used. Annealing consist on heating up the sample, usually to about 800 °C, which allows the vacancies to move around the diamond lattice. Vacancies are more stable when adjacent to a nitrogen atom, therefore when a vacancy reaches a N defect, they join into a NV center that remains stable [102].

Nitrogen-Vacancy defects have two possible charge states, neutrally and negatively charged, referred respectively as NV0 and NV-. The NV- state is achieved by the incorporation of an electron into the defect from a donor, usually a single nitrogen substitution defect. The NV center is not necessarily stable, and can switch between its two charge modes [103].

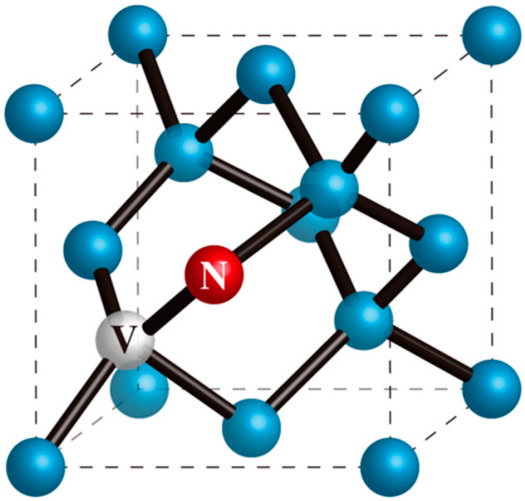


Figure 37: Structure of a Nitrogen-vacancy color center within the diamond cubic cell. The center is formed by two adjacent defects, a Nitrogen substitution of Carbon and an adjacent vacancy. Source: [104].

Both of NV charge states have optical transitions between an excited and a ground state, all localized inside the large diamond bandgap. The zero-phonon lines of the transitions have wavelengths of 575 nm for NV0 and and 638 nm for NV- [105]. Both peaks have also been observed to broaden with temperature, which makes them of interest to our goals.

Of the two charged states, the negative one has attracted the most attention due to its various applications. This center has shown great potential for quantum computing applications, as the spin of the added electron can be initialized and read out optically [106]. As it was discussed in section 2.4.3 the center can also be used as a magnetometry sensor by measuring the splitting of the electron states with magnetic quantum number $m_s = \pm 1$ [107]. More relevantly for us, the transition between the spin magnetic quantum number states $m_s = 0$ and $m_s = \pm 1$ is highly depended on temperature, a property that makes the NV- defect a commonly used PL temperature probe [108].

However, we cannot use the NV- state in our study, as this defect can not be observed at all in CL, hence why its associated peak is not present in figures 30 nor 53. This is because electron beam radiation switches the NV- peak to NV0, as has been observed by [109]. The reason for the switch appears to be the negatively charged incident electrons pushing the negative charge away as they excite the defect, ensuring all excited defects are in their neutral charge state.

This vanishing of the NV- peak under a CL beam is also present in nanodiamonds, as shown in figure 38. In this figure, there appears to be a slight NV- signal in CL model, which is likely produced by the PL emission induced by the CL signal of the NV0 state. The differences between PL and CL on the nanodiamond samples will be discussed in more detail in section 6.2.2.

The electronic structure of both NV states has been studied in detail by Larsson and Delaney [110]. To obtain this structure, they considered the atomic orbitals overlapping in the vacancy: The three sp^3 orbitals from the adjacent carbons, and the sp^3 orbital of the nitrogen, as can be seen in figure 37. The orthonormal energy levels that are obtained by linearly recombining those orbitals are as follows:

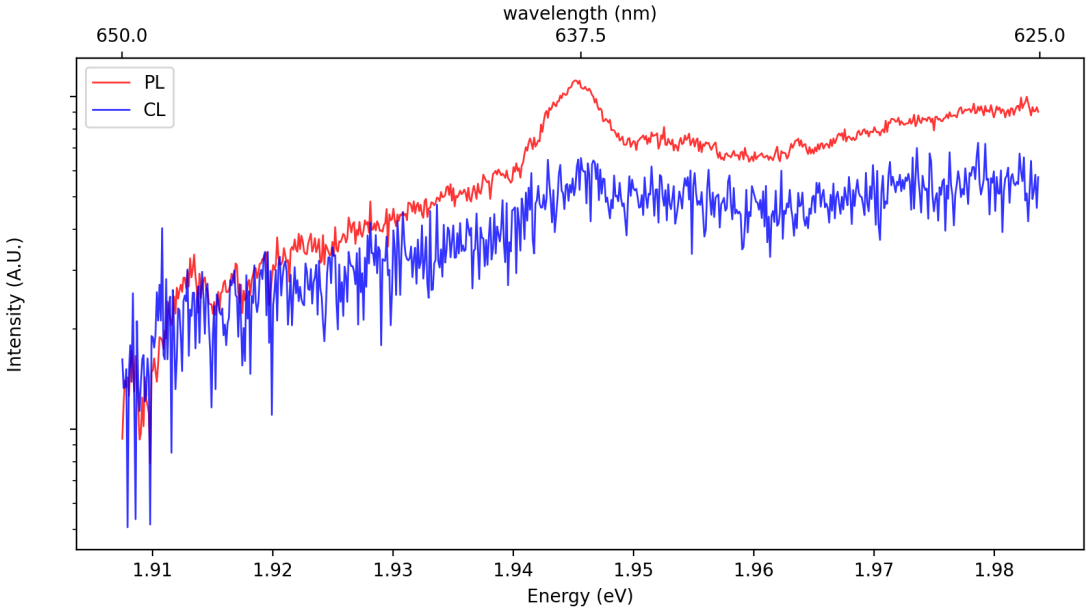


Figure 38: PL and CL signals from heavy nitrogen-doped nanodiamonds (2.5 ppm) at 50 K in the NV- emission energy range. The intensity is in logarithmic scale, and both spectra have been rescaled for visual clarity.

$$v = (a + b + c)/\sqrt{3 + 6S}$$
$$u = (d - \lambda v)/\sqrt{1 - \lambda^2}$$
$$e_x = (2c - a - b)/\sqrt{6 + 6S}$$
$$e_y = (a - b)/\sqrt{2 + 2S}$$

With: a, b, c the Carbon sp^3 orbitals, d the Nitrogen sp^3 orbital, $S = \langle a|b\rangle$ and $\lambda = \langle d|v\rangle$. The two e levels have the same total energy.

All these three levels exist within the very large diamond bandgap. The u orbital, the closest to the nitrogen atom, is the one with the lowest energy, while the e orbitals are the most energetic. The ground states of the NV0 and NV- charge states are $u^2v^2e^1$ and $u^2v^2e^2$, respectively. The transition that produces the 637 nm line in NV- is $u^2v^1e^3 \rightarrow u^2v^2e^2$, while the transition for the NV0 575 nm line is $u^2v^1e^2 \rightarrow u^2v^2e^1$. The lifetime of the excited states has been measured in nanodiamonds to be 23 ± 6 ns for NV-, and 29 ± 7 ns for NV0 [111].

The fine and hyperfine structures of the electronic levels in NV0 and NV- are a heavily debated topic, with no current consensus [112, 113]. The broadening with temperature of both NV0 and NV- peaks is a significant part of that discussion, as it hints at some interaction between the NV states and phonons [114]. However, as the energy distribution of the peak does not correspond with those of diamond phonons, this connection is more complex than a phonon mediated transition.

The peak broadening with temperature is even more strange when considering that both peaks emit a series of well defined replicas at lower energies, which are attributed to the defect vibronic structure [112]. Figure 30 shows those vibronic bands for our NV0 emission.

These vibronic bands show that neither the valence nor conduction band states are involved in the optical transitions; but rather that the NV energy levels are deep inside the diamond bandgap, far from the diamond lattice states [112].

Lacking a better understanding of the underlying physics that cause the NV0 peak broadening, we will focus on numerically analyzing its relationship with temperature, and we will study and test other factors that may be contributing to the broadening, in order to help improve our understanding of this peak.

5.5 NV0 peak in bulk diamond

Now that we have discussed the physical origins of the NV0 peak, we can focus on its structure and properties. As discussed in section 5.4, the NV0 peak has been observed to evolve with temperature, which combined with the fact that it is the brightest feature of the spectra by an order of magnitude, marks the peak as an excellent potential candidate for a thermal sensor.

As we can see in figure 39, the shape and intensity of the NV0 peak have both a strong evolution with temperature, with the intensity decreasing as the sample heats up, but remaining high even at room temperature. This loss of intensity could be used to estimate the temperature, however it may also be detrimental, as the exposure time required to infer the temperature will be longer the less bright the signal is.

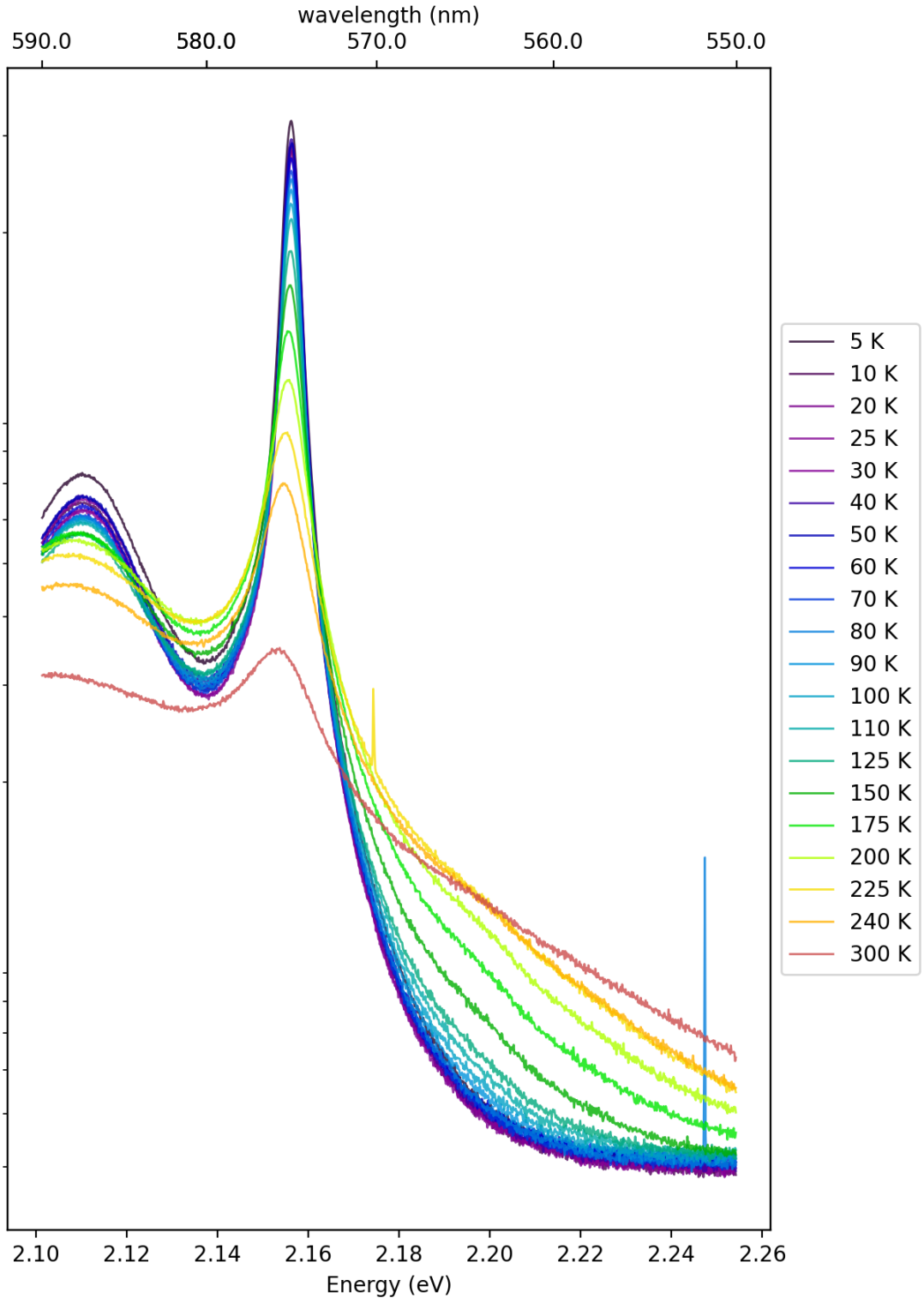


Figure 39: Neutral Nitrogen-Vacancy defect peaks of CVD grown bulk diamond with nitrogen doping for all measured temperatures. The intensity axis used a logarithmic scale.

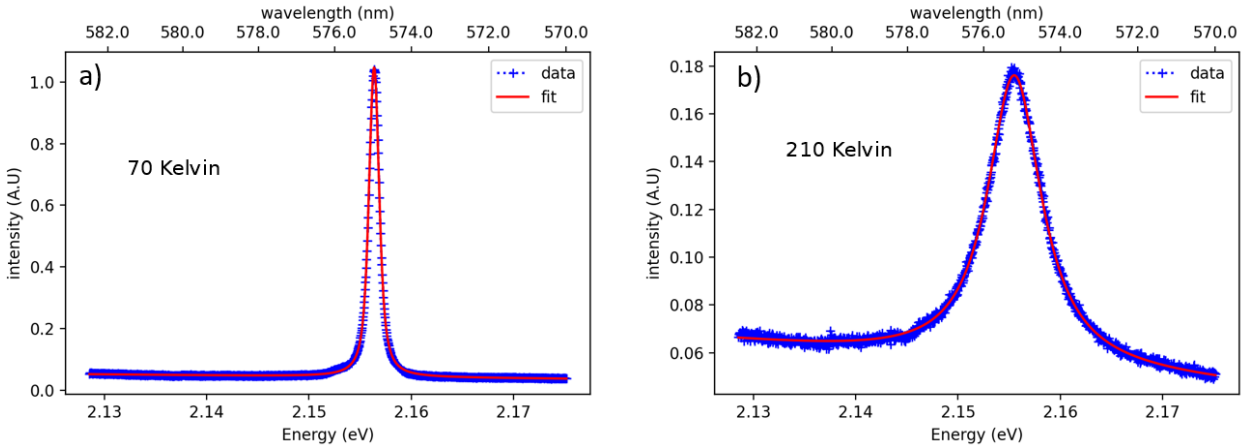


Figure 40: Neutral Nitrogen-Vacancy defect peaks and associated fits of CVD grown bulk diamond with nitrogen doping for a) 70 and b) 210 K. Fit was similarly accurate for all temperatures. The intensity axis used a linear scale, and each fit has been rescaled for visual clarity purposes . Data is the same as figure 39.

In order to properly study the evolution of the NV0 peak with temperature, we fitted it to a function with the goal to extract its key parameters. After some experimentation, we settled on a Voigt profile as the model for the peak, with an added linear background noise, also to be fitted. Examples of the fit for the spectra at low and high temperature can be seen in figure 40.

The Voigt profile is a convolution of a Gaussian and a Lorentzian profiles [115]:

$$V(x,\sigma,\gamma) = \int_{-\infty}^{\infty} G(\xi,\sigma)L(x-\xi,\gamma)d\xi$$

$$\text{With:} \quad G(x,\sigma) = \frac{e^{-\frac{x^2}{2\sigma^2}}}{\sqrt{2\pi}\sigma} \quad ; \quad L(x,\gamma) = \frac{\gamma}{\pi(\gamma^2+x^2)}$$

It has two parameters: σ, which corresponds to the standard deviation of the underlying Gaussian peak; and γ, which corresponds to the median absolute deviation of the Lorentzian peak. If one of those parameters is very close to zero, the associated function will be a Dirac delta, and therefore the Voigt profile will be equal to the other function in the convolution.

The density function of the Voigt does not have an analytical expression. To calculate the fit, we used the numerical approximation implemented in the Python library Scipy [116].

From the profile fits, a collection of peak parameters can be obtained. We tested some of them as potential temperature sensors, including total intensity, peak intensity, peak position, the sigma and gamma Voigt parameters, and full width at half maximum. Three of them (peak position, peak intensity and full width at half maximum) showed some promise due to their significant evolution with temperature, so they were studied in more detail.

Peak intensity was calculated as the number of counts at the maximum point of the fit, to reduce the impact of noise and increase precision. However, as seen in figure 40, the difference between this value and the maximum data point is very small. This means we could potentially skip the fit if we were only interested in this parameter, enabling faster and simpler measurements.

Before we proceed, we must be aware of a large intrinsic limitation to peak intensity as a temperature sensor. As all intensity-derived parameters, it will depend on a large number of factors that affect intensity counts. Such factors include: The concentration of NV0 in the irradiated region, the electron beam conditions, the aperture of the slit, and the spectrometer characteristics, just to name a few.

Due to the infeasibility of separating those different contributions from the effect of temperature, the parameter cannot be used as an absolute temperature sensor. It is possible, however, to use peak intensity as a relative temperature sensor, as long as we ensure the measurement conditions, including the beam position on the sample, stay the same.

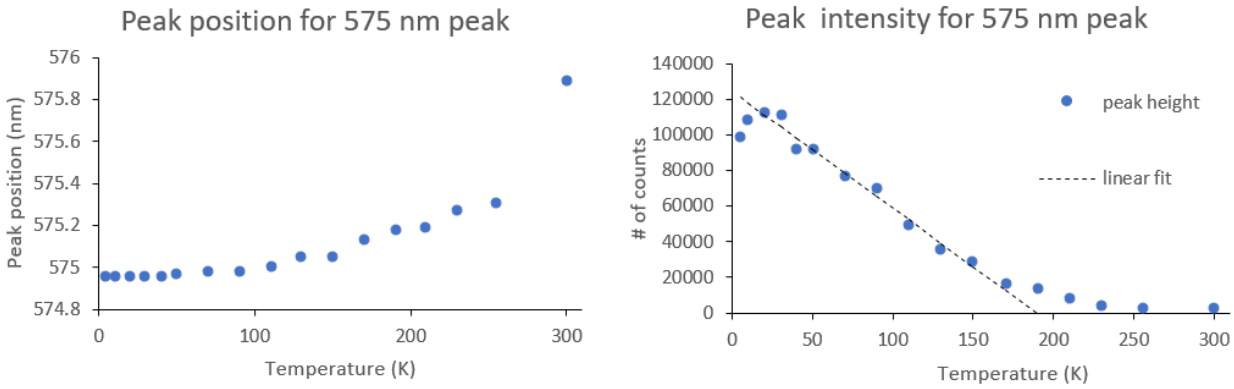


Figure 41: Peak position (left) and intensity (right) of the NV0 defect peak in bulk diamond. Both parameters are estimated using the Voigt fit.

The results of the peak intensity vs temperature for the bulk sample can be seen in figure 41

(right). The value of the parameter appears to decrease linearly with temperature between 20 and 170 K. Performing a linear fit between these temperatures gives us an R squared value of 98.8%, which means a linear fit is adequate for the data.

The linearity disappears after 170 K, which hints at some kind of paradigm shift. Interestingly, the linearity is preserved up to room temperature in the nanodiamond samples, as will be discussed in chapter 6.

The linearity enables peak intensity to serve as an adequate relative temperature sensor in the 20 to 170 K temperature range, but it can not be used as an absolute temperature sensor for the reasons listed above. Hence, the main value of this parameter is the ease of access, since a model fit is not required to obtain its value. However, due to its limited applicability, we did not pursue study of the peak intensity any further.

Peak position was determined as the wavelength of the Voigt fit maximum position. This was done for two reasons: Firstly, since we need the exact position of the maximum, using the fit makes the parameter more resilient to noise, as discussed for the peak position parameter. The second is that the fit enables us to surpass the resolution of the spectrometer (0.012 nm as discussed in section 3.2). This was necessary as the change in the peak position with temperature was very small (less than 1 nm between 5 and 300 K).

The evolution of peak position with temperature can be seen in figure 41 (left). As shown in said figure, there is a slow increase in the peak's wavelength as temperature grows. This corresponds to a decrease in the peak energy of roughly 1 meV between the lowest temperature and 250 K. Since the change is so small, the peak position is extremely sensitive to noise. For this reason and the lack of a good model fit to predict the evolution of the parameter with temperature made us discard the peak position as a temperature sensor in the end.

The last parameter studied was the full width at half maximum (FWHM) of the NV0 peak. Since the Voigt profile does not have a known analytical function for the value of this parameter, we calculated it using the expression obtained by J.J. Olivero and R.L. Longbothum [98], which has a maximum error rate of 0.02%.

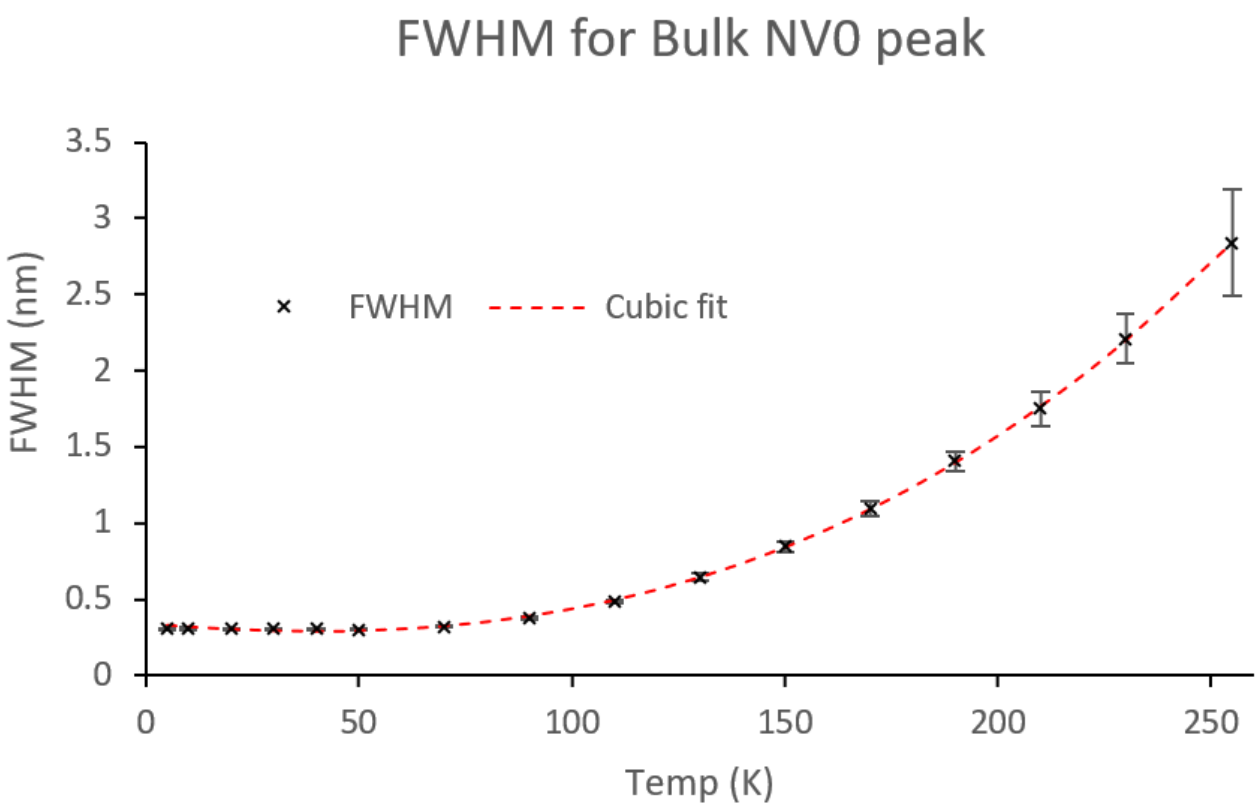


Figure 42: Full width at half maximum of the NV0 defect peak in bulk diamond and associated cubic model. The parameter was estimated using the Voigt fit, and J.J. Olivero and R.L. Longbothum [98] approximation. Dataset is the same as figure 39.

As seen in figure 40, the change in FWHM with temperature is quite significant, being noticeable directly on the images. The exact value of the FWHM vs temperature can be seen in figure 42. In this figure, we modeled the evolution with temperature using a cubic curve, which allows for a good fit. A similar cubic function was also found to be a good model for the nanodiamond FWHM.

Figure 42 shows that the value of the FWHM evolves from 0.3 nm to 3 nm in the 5 to 250 K range, much larger than the change in peak position. This change was even more pronounced in nanodiamonds, as will be discussed in chapter 6.

The slope of the FWHM vs temperature curve grows quite fast, making the peak a good temperature sensor above 150 K. However, due to the strong decrease in intensity, the FWHM is highly sensitive to noise at high temperatures. This can be seen in the expanding error bars in figure 42. With this fact in consideration, the FWHM seems best fit to estimate

temperatures for bulk diamond in the 150 K to 200 K range, but is limited beyond that.

As can be seen from figure 42, the thermal precision is different for each temperature. At the highest possible temperature, 210 K, the error induced by the model is ±5 K. As the measurement time was 5 s, the resulting thermal precision is 11 K/$\sqrt{\text{Hz}}$.

5.6 Phonon-assisted exciton peaks

The only feature of the ultraviolet spectra that was interesting for our purposes were the phonon-assisted exciton peaks, a collection of four peaks with wavelengths between 5.24 and 5.35 eV, shown in figure 43. The origin of these peaks, as the name implies, is the exciton decay in diamond, and their energy is close to that of the diamond bandgap (5.47 eV at 300 K).

However, the phonon-assisted exciton peaks all have energies slightly below the diamond 5.47 eV bandgap. This is because diamond is an indirect bandgap material, meaning the top and bottom levels of the valence and conduction band respectively have a different crystal momentum. In order for crystal momentum to be conserved, the exciton decay must also produce a phonon with the same crystal momentum as the difference between the bands, which will require some energy.

The indirect bandgap reduces the chance of radiative exciton decay, which leads to relatively low luminosity of the phonon assisted peaks. Hence, we raised the exposure time to improve the signal to noise ratio. The peaks also become less bright as the temperature increases.

Figure 43 also shows a pair of very thin peaks with an energy of 5.37 eV, only at low temperature. According to Alexander Zaitsev *Optical Properties of Diamond*, [86] the peaks may be associated with the N9 center. Our current hypothesis is that the peaks have their origin in a bound exciton decay [117], due to their narrow shape. However, the peaks are not interesting to our goals, since they are not bright, do not change their shape with temperature, and disappear above 90 K. Hence, they will not be discussed any further.

There are four phonons modes in diamond: The transverse acoustic and optical modes, labeled

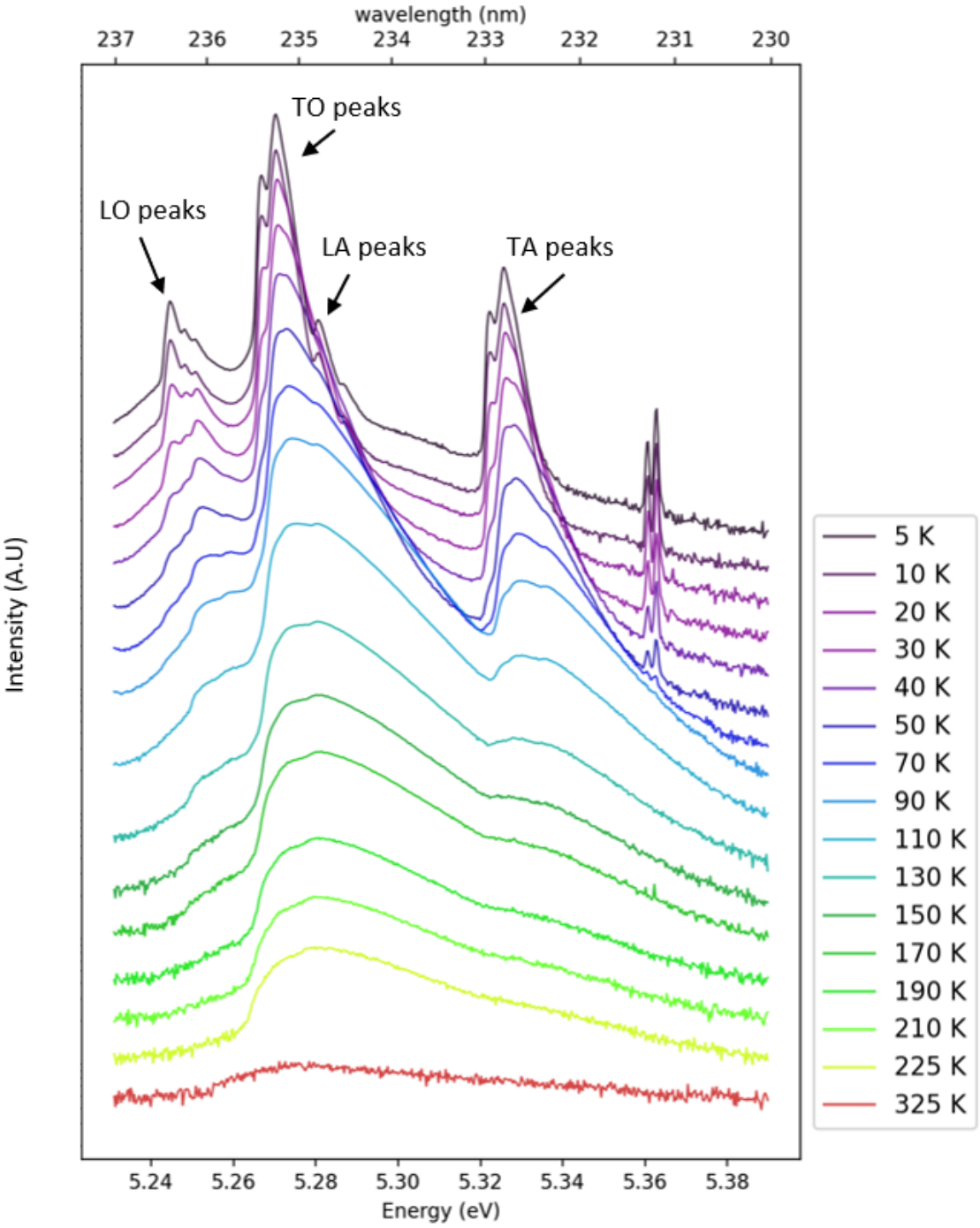


Figure 43: Phonon assisted exciton peaks of CVD grown bulk diamond with nitrogen doping for multiple temperatures. The intensity axis used a logarithmic scale. Measurements were done by irradiating a single point with the SEM electron beam. The acceleration voltage was kept to 10 kV and the exposure time was 50 s.

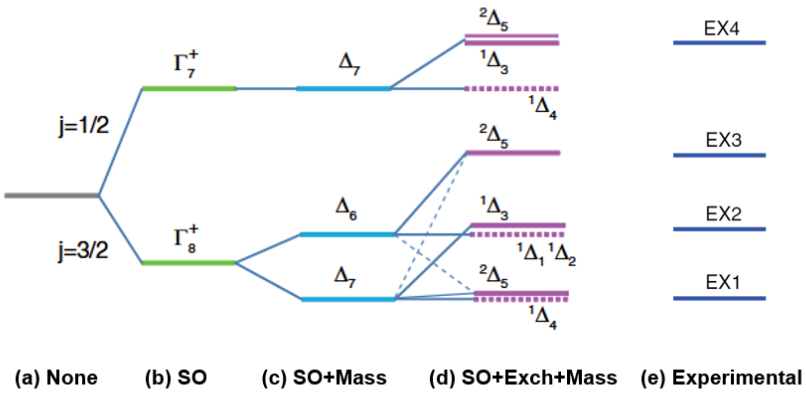


Figure 44: Comparison between theoretical (a-d) and experimental (e) exciton energy levels in diamond. a) Model assuming no splitting. b)Spin-orbit model. c) Spin-orbit + hole mass anisotropy model d) Spin-orbit + hole mass anisotropy + exchange interaction model. Dotted lines indicate optically dark states. Source [118].

TA and TO, and the longitudinal acoustic and optical modes, labeled LA and LO. Hence, we observe four phonon peaks in figure 43, each associated with a phonon.

We must also consider the exciton itself, which has a fine structure related to combined spin-orbit interaction, electron exchange interaction, and hole mass anisotropy splitting, which will cause each phonon line to be separated into four fine structure states, as was demonstrated by Hazama, Naka and Stolz [118]. A diagram from their article can be seen in figure 44. These fine structure states can be seen specially well in our data for the LO peak.

As the energy distribution of the phonons has a known model with a temperature dependence, we can use the peak positions and shapes to estimate the temperature of a sample, as has been studied by [83].

The shape of each phonon peak will then be related to the energy distribution of the associated phonon mode. That is, a Maxwell-Boltzmann distribution with four peaks, one for each exciton fine structure state [118]. The energy differences between those four peaks are the same for all four phonon lines, since they are related only to the exciton.

In order to estimate the temperature of the sample using the phonon peaks, we fit their energies according to the following Maxwell-Boltzmann distribution:

$$I(E,T) = \sum_{i=1}^{4} A_i(T)\sqrt{E - E_i} * exp\left[-\frac{(E - E_i)}{k_B T}\right], \tag{7}$$
$$\text{With: } A_i(T) = a_i exp\left[-\frac{(E_i - E_1)}{k_B T}\right]$$

Where: k_B is Boltzmann's constant, a_i are the tabulated fine structure relative amplitudes [118], and E_i are the energies of the four fine structure peaks. Examples of the phonon peaks shapes and their associated fits at different temperatures can be seen in figure 45, with the only fitting parameter changing being the temperature.

This method allows for an accurate prediction of the temperature up to 200 K. Above this temperature, the intensity of the phonon peaks is significantly reduced, as seen in figure 43, which leads to lower accuracy. The peaks also become more and more overlapped, which makes the numerical fitting more complex and less precise.

The temperatures estimated by this method below the 200 K mark were is close agreement with those indicated by the cryostat, as seen in figure 46. There is a discrepancy at very low temperature, which was to be expected as discussed in section 3.2. In fact, lowest temperature according to the phonon fit method was 14 K. The temperature also appears to be systematically slightly higher for the phonon model vs the cryostat. This is likely due to electron beam heating, as discussed in section 3.1.

5.7 Conclusion

Our analysis of the bulk diamond spectra with temperature has revealed two sets of peaks that can be used to determine the temperature of nitrogen-doped bulk diamond from its CL signal:

The first family of peaks are the phonon-assisted exciton peaks, which provide a strong temperature predictor thanks to the energy dependence of the phonons with temperature. They allow to predict the temperature in the 15 to 200 K range. Above this point, the different peaks start to mix, and their intensity decreases, making them more sensitive to noise.

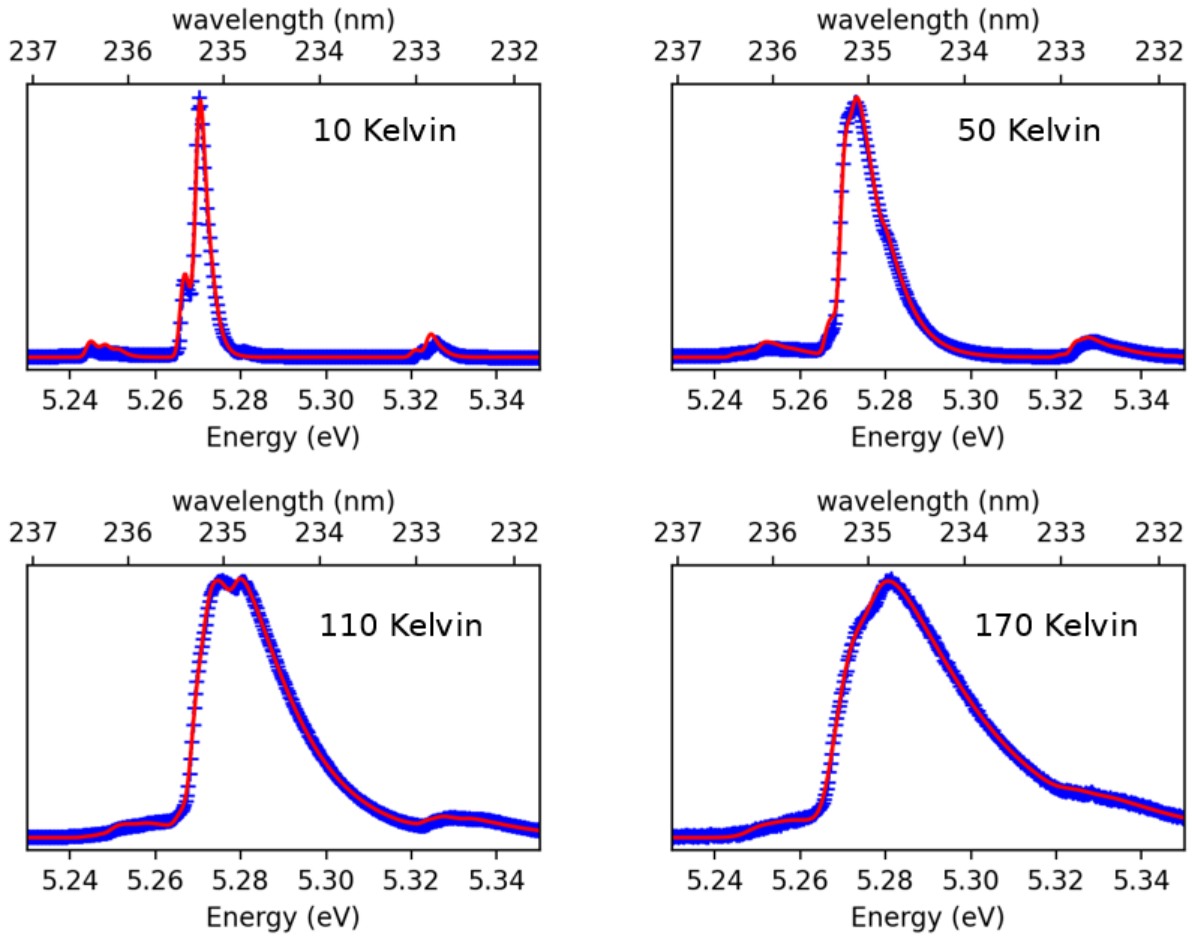


Figure 45: Phonon assisted exciton peaks and associated fits of CVD grown bulk diamond with nitrogen doping for multiple temperatures. The y axis represents intensity in a linear scale, and each fit has been rescaled for visual clarity purposes . Data is the same as figure 43.

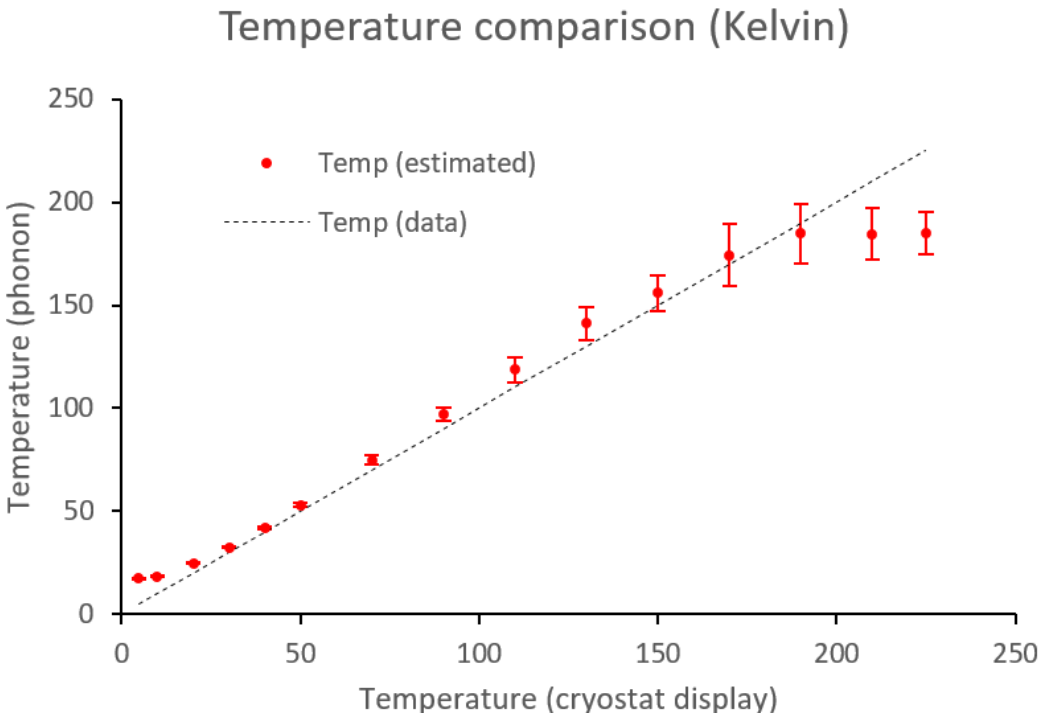


Figure 46: Comparison of the temperature given by the cryostat vs temperature estimated by the phonon peak fitting.

The second peak is the NV0, which provides a quickly accessible relative temperature sensor in its peak intensity for temperatures between 20 and 170 K, and it's full width at half maximum, which can be used as a temperature sensor in the 150-200 K range. However, it appears to be possible to raise this limit by increasing the NV0 brightness.

A summary of the different peaks discussed can be seen in figure 47. In the following chapters, we discuss if and how these peaks and methods can be translated to nanodiamonds.

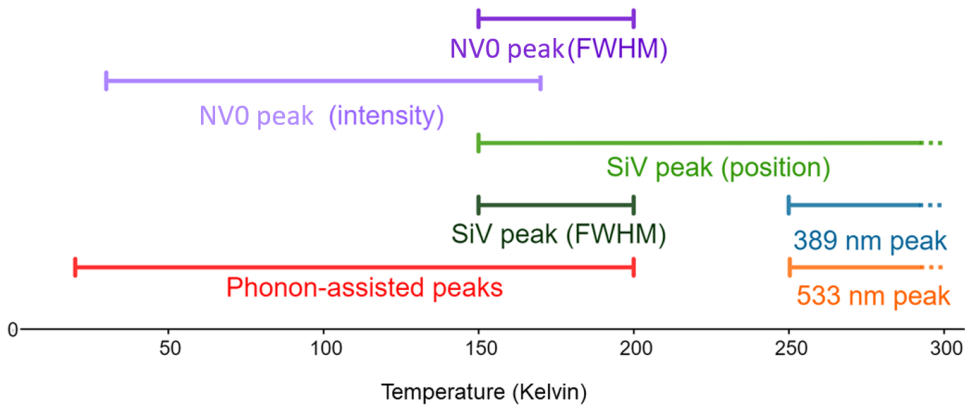


Figure 47: Working range of the different diamond CL temperature sensors discussed in this chapter.

6 Nanodiamond cathodoluminescence spectral results for thermal sensing

Nanodiamonds were chosen as a CL temperature probe for multiple reasons: First of all, their superb chemical and physical stability [119] mean that they can be deposited on all kinds of substrates, will not decay with time, and will resist electron microscopy with high acceleration voltages.

Secondly, diamond is one of the best thermal conductors in existence. This favors the thermalization of nanodiamonds deposited on a sample, meaning sample temperature at the contact point will be matched by the nanodiamond. Nanodiamonds can be grown to be incredibly small, down to a single nanometer [46], which potentially allows for higher spatial resolution.

Finally and as discussed in chapter 5, there exists a series of CL peaks in nitrogen doped diamond that can be used for thermal sensing. Hence, in this chapter we will study the CL properties of nitrogen doped ND in order to develop a CL thermal sensing method.

6.1 Nanodiamond structure

6.1.1 Physical characterization of nanodiamond samples

The nanodiamond samples chosen for our study were a commercially available Sigma-Aldrich fluorescent ND powder, with heavy nitrogen doping. Product specifications can be found in [120]. According to the information provided by the seller, the nanodiamonds contain 2.5 parts per million NV centers and have an average size of 70 nanometers. This corresponds to roughly 10 NV centers per sample, assuming the ND is a perfect sphere. This large concentration of NV leads to a high brightness, which was the main reason to choose these samples. However, experimental observations showed us that these NV were poly-dispersed, with the concentration of NV center different for each ND.

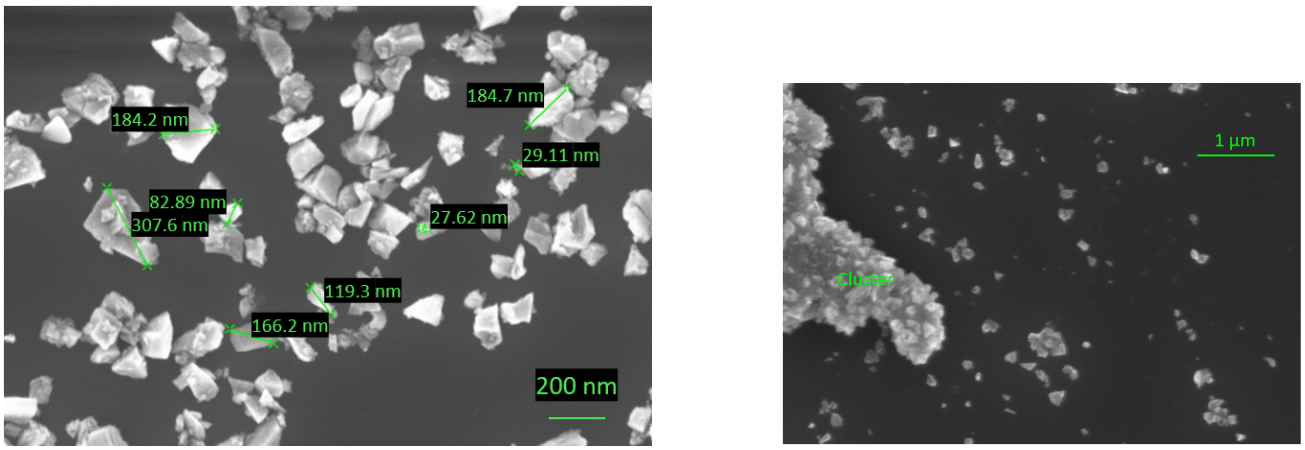


Figure 48: Left: SEM image of the ND samples. Measurement was done by Hugues Girard of Université Paris-Saclay. We can appreciate the heterogeneity of samples sizes and shapes. Right: Example of nanodiamond spread on top of Si substrate. Spread was similar for SiO_2 and GaN, with both large clusters and isolated ND.

In order to study the CL spectra of the ND, we deposited them on top of multiple substrates: Silicon oxide, silicon and an etched InGaN LED with a top GaN layer. The purpose and results of these different substrates will be discussed later in the chapter. The ND were on a colloidal suspension in deionized water. In order to deposit the ND on top of the substrates, we placed a droplet of the ND suspension on top of the chosen substrate, and waited for it to evaporate. After evaporation, a thin layer of nanodiamonds was formed.

The silicon and silicon oxide were cleaned before deposition by being submerged in ethanol and subjected to an ultrasonic bath for 2 minutes. No similar treatment was employed on the LED, to avoid damaging the etched structure.

This deposition allowed us to perform SEM imagings of the ND samples, which revealed their sizes and shapes to be highly inhomogeneous, as seen in figure 48, going from less than 10 nm to more than 300 nm. The SEM imaging also showed the ND density to be very heterogeneous, with some region where the ND were isolated from one another, and other regions where they concentrated forming large clusters. Figure 48 shows an area where both isolated samples and a cluster could be observed.

The nanodiamonds were firmly attached to all substrates; they did not move or detach even if the sample was flipped upside down. This is most likely due to Van der Waals bonding, which could

potentially impact the chemical properties of the ND surface, therefore causing said properties to change between different substrates. This hypothesis and its consequences will be discussed further in section 6.4.7.

The estimated average height of the clusters was highly variable, going from less than 40 nm in some regions to more than 300 nm. A layer smaller than the average ND size can be explained due to the large range of possible sizes, alongside the fact that ND will naturally deposit with their shorter axis in the vertical direction.

The extension of the clusters could range from a few micrometers to millimeters. Interestingly, the edges of the clusters always had a much shorter vertical width that any other area, being even smaller than our minimum resolution of 16 nm in some cases.

The depth of the clusters was measured thanks to the InGaN LED substrate. The process will be explained in more detail in section 6.4.6, but in short, this was achieved by measuring the maximum acceleration voltage that did not excite the active region of the LED. The InGaN LED has very high luminescence in a band not present in the ND (450 nm), allowing us to separate its CL signal from that of the ND. By determining the minimum acceleration voltage required to excite the LED band, and comparing it with the vertical length of the interaction volume in diamond, we could estimate the depth of the ND layer.

6.1.2 Surface chemical characterization

As will be discussed in this chapter, various measurements of the nanodiamonds revealed their surface chemistry to play an important role in the properties of NV emission. In order to understand this surface in more detail, our collaborators from Universite-Paris Saclay performed a chemical analysis of the nanodiamond. These analysis were then published as part of the results on nanodiamond [2], and we will proceed to discuss them.

The first analysis they performed was infrared spectroscopy directly on the ND solution. The measurements were performed on a Bruker Alpha II spectrometer equipped with a Platinum ATR system (diamond crystal), with 128 scans for the sample and 64 scans for the background.

The results of these measurements revealed a partially oxidized surface, with C-H stretching bonds remaining on the surface, which may originate from non-diamond phases. At the same time, C=O stretching mode appears at 1740 cm^{-1}, which is downshifted compared to those of equivalent air-treated particles (highly oxidized) which typically peak at 1780 cm^{-1}. Further measurements on the Zeta potential corroborated the low oxidation, showing a value of only -20 mV, whereas highly oxidized particles often exhibit Zeta potentials as low as -50 mV [121].

Surface oxidation of nanodiamond is known to be detrimental to the stability of the NV center [122], which may explain this partially oxidized surface. As Sigma-Aldrich sells these nanodiamond specifically for their high NV fluorescence, they may have develop some proprietary surface treatment to enhance emission that limits oxidation. This represents a potential issue for us, as the size and shape of the samples is inhomogeneous, and therefore the effect on NV emission of this treatment will be sample dependent, which may have a negative impact on the stability of our temperature sensing method.

6.2 Nanodiamond photoluminescence

6.2.1 Fluorolog Photoluminescence

The Neutrally charged Nitrogen Vacancy peak is known to have a low photoluminescence signal due to its weak photo-absorption. In fact, NV0 was initially only observed in cathodoluminescence [112]. Despite this limitation, we attempted to perform photoluminescence characterization of our nanodiamond samples, which we will proceed to discuss.

The first PL measurements were performed using the HORIBA Fluorolog described in section 3.3. The emission of both the NV0 and NV- peak were measured for PL excitation wavelengths from 350 nm to 540 nm, in 10 nm steps. The resulting spectra can be seen in figure 49. Our results were similar to those obtained by Beha *et al.* [123], with an intensity maximum for NV- emission at an excitation wavelength of 520 nm. Emission from NV0 reached a maximum at 470 nm excitation, but both signals were quite weak overall.

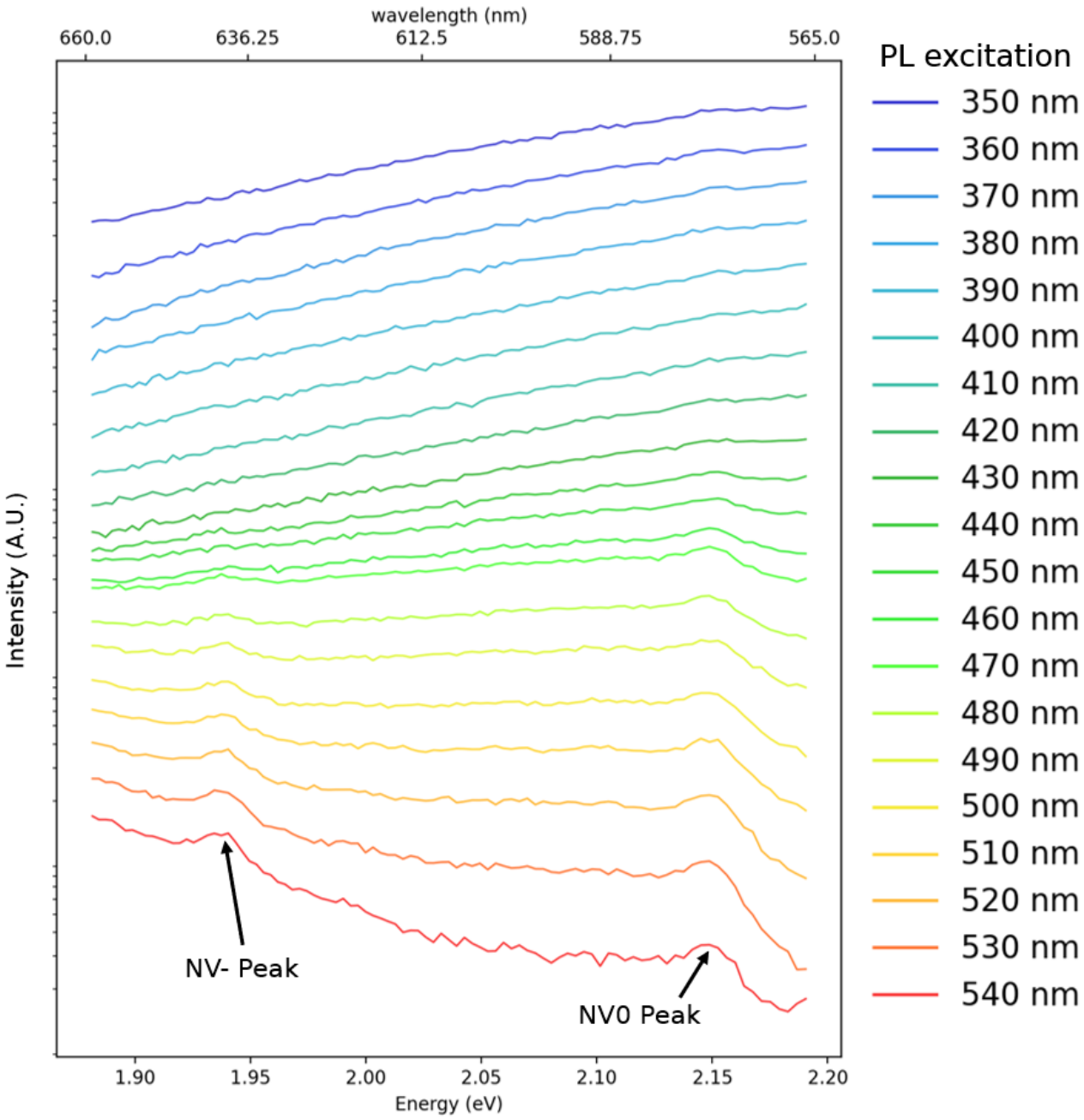


Figure 49: PL spectra of nitrogen-doped ND in the NV0 and NV- emission regions obtained by the HORIBA Fluorolog described in section 3.3. The fluorolog had a controllable excitation wavelength, so we can compare the excitation efficiency on both NV0 and NV- for different photon energies.

The low emission was to be expected: As discussed before, NV0 is very weak under photoluminescence. As for NV-, the PL maximum is normally achieved using 575 nm light, which can be easily absorbed by an NV defect in the neutral state. Part of the excited NV0 will switch to NV- before emission, emitting a PL peak at wavelength of 638 nm. However, since our focus is NV0, we did not wish to employ a PL beam close to 575 nm, to avoid hiding the NV0 signal itself in the reflected light, hence we did not obtain a high intensity signal for NV-.

Oddly enough, both NV0 and NV- signals were weaker under the 452 nm laser than for a similar wavelength under the controllable lamp. This has been attributed to the lower power of the laser compared with that of the lamp. The lower signal harmed our ability to reliably measure lifetime, since as discussed in section 3.3, a laser light is required to measure lifetime in the fluorolog.

The lifetime of NV0 at room temperature was estimated to be 15±5 nanoseconds with this method. This is lower than the expected value of 29±7 ns at room temperature reported by [111]. One of the main factors that could explain this discrepancy on the nanodiamond surface, which has been observed to affect lifetime [124]. In nanodiamonds, since each individual sample has a different surface, the lifetime of NV can change significantly from sample to sample, as seen in previous studies [111, 125]. The work of Sophie Meuret *et al.* supports this observation, as they noticed a decrease in NV0 lifetime from 23.4±0.7 to 15.8±0.8 withing the same nanodiamond sample by irradiating different regions [126]. In particular, NV0 defects closer to the edge of the sample had shorter lifetimes.

In comparison, the CL lifetime of the NV0 peak, measured in section 6.7 was 18 ± 2 ns. In said section, it will be shown that the ND surface chemical properties had a severe impact on the lifetime. Hence, the shorter than expected lifetime is most likely due to the Sigma-Aldrich surface chemical treatment, which appears to achieve high NV luminosity by reducing the lifetime of the defect excited state.

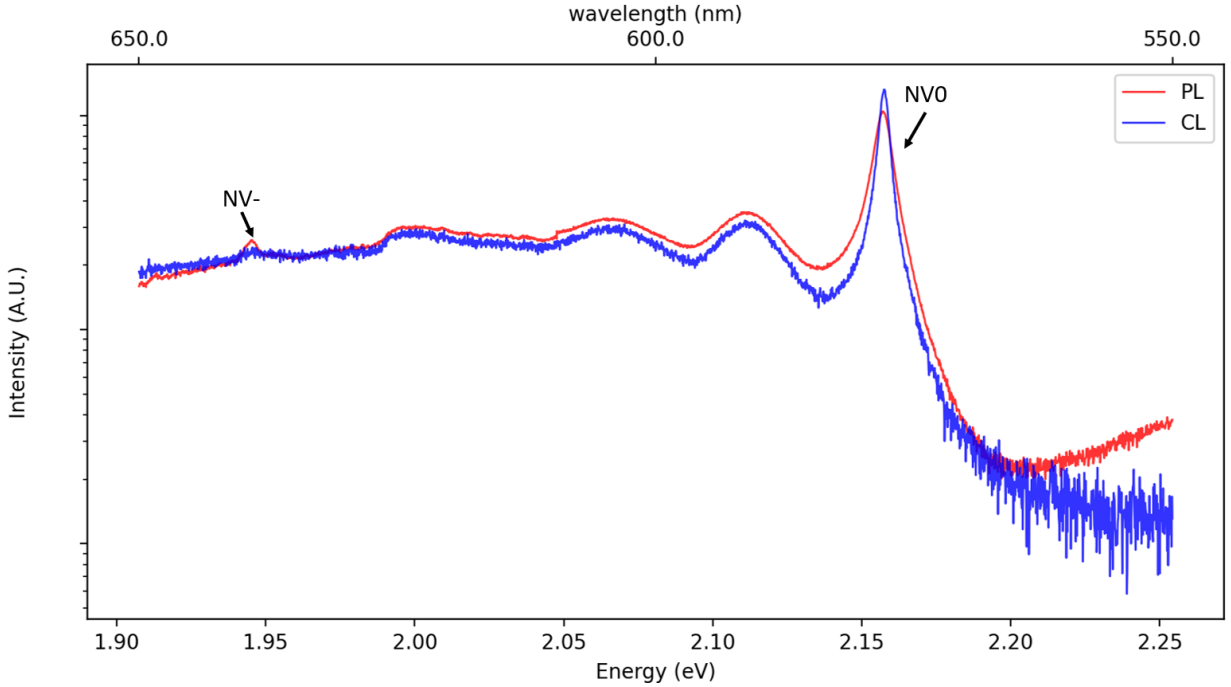


Figure 50: PL and CL signals from nitrogen-doped nanodiamonds at 50 K in the NV0 and NV- emission energy range. The intensity is in logarithmic scale, and both spectra have been rescaled for visual clarity.

6.2.2 Simultaneous photoluminescence and cathodoluminescence

To further study the photoluminescence signal of the NV0 defect in nanodiamonds, we decided to use the FESEM setup, as it allowed us to control the temperature and study its effect on the signal.

As discussed in section 3.3, the FESEM laser has a wavelength of 375 nm, more energetic than the 456 nm laser available in the fluorolog. FESEM PL measurements produced a much higher PL intensity in NV0 than those of the fluorolog, but we believe the main reason was not the difference in wavelength, but the extra activation of NV0 that can be achieved by irradiating diamond with an electron beam [109].

The FESEM had another advantage over the fluorolog: It enabled us to perform photoluminescence and cathodoluminescence simultaneously, and to compare the two techniques directly. However, an important consideration must be taken into account in order to perform this type of measurement: We need to ensure the laser spot and the electron beam are focused on the same region.

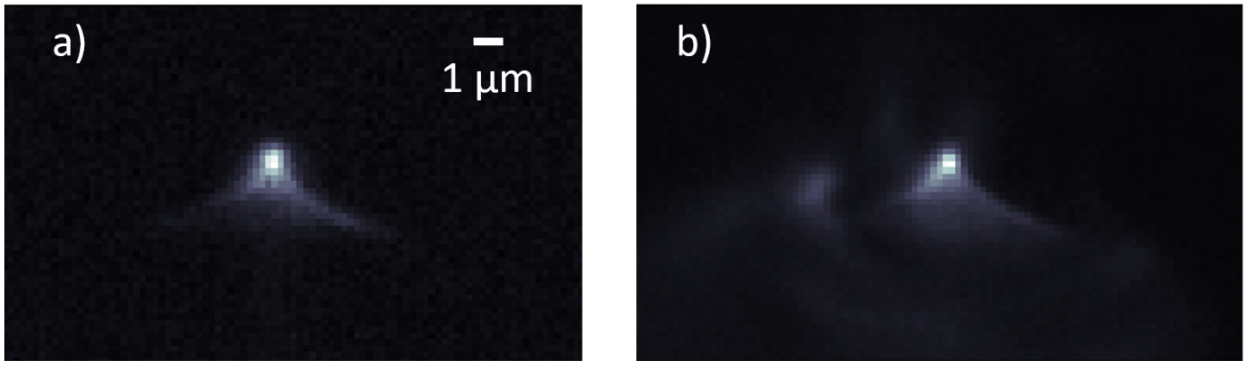


Figure 51: CCD image of produced light on a nanodiamond sample spread on top of a Silicon substrate under a) Cathodoluminescence Beam at 10 kV b) Photoluminescence laser of 375 nm at 10 kHz. Mirror position was the same in both cases

This simultaneous focus is achieved by carefully positioning the parabolic mirror described in section 3.2. The mirror both aims the laser spot and collects the PL and CL signals. Hence, the electron beam can not change position during a measurement. The acceleration voltage has to be chosen in such a way that the e-h pairs are created at the same depth in both PL and CL. We can test if these conditions are achieved simply by comparing the spatial distribution of both signals in the CCD camera. Figure 50 shows an example of a pair of these measurements.

Figure 51, shows these distributions for the final alignment used. We can see that both signals are concentrated on the same central spot, meaning that the electron beam and laser are focused on the same nanodiamond. The image 51 b), corresponding to the PL signal, has a series of secondary points out of alignment. These correspond to ND close to the studied sample. Since the laser spot is larger than the electron beam spot, the activation of secondary samples is unavoidable. Fortunately, these ND are so far from the original sample, and from alignment, that their signal can be treated as noise, and can be filtered out by adjusting the setup slit.

The results of these simultaneous PL and CL measurements reveal a behavior similar to that discussed in section 5.5 for bulk diamond: The shape of the peak can be fitted to a Voigt profile, and the full width at half maximum evolves strongly with temperature. However, a key difference between the two samples is the brightness. NV0 is much brighter in our nanodiamond samples, likely due to larger nitrogen doping. Thanks to the extra brightness, we have enough signal even at room temperature to fit the NV0 and extract the parameters. The PL and CL signals have

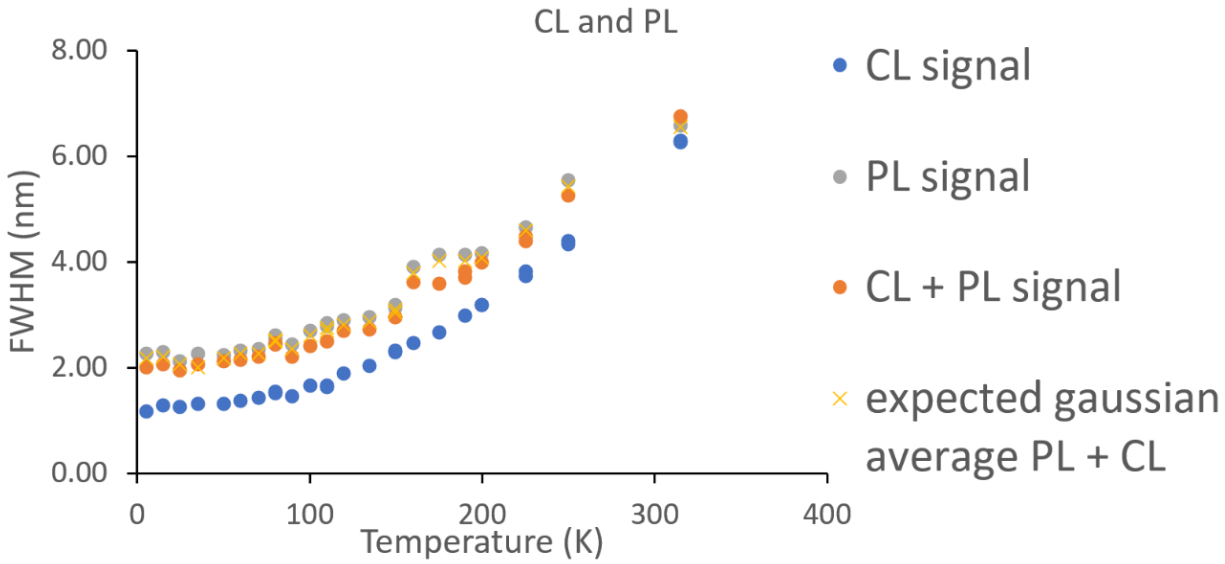


Figure 52: FWHM of the NV0 peak in ND on top of silicon, estimated with a Voigt profile fitting with linear noise. FWHM was measured with PL, CL and simultaneous PL and CL spectroscopy at multiple temperatures. The expected FWHM for the combinations of the PL and CL signal is also displayed.

similar brightness.

Figure 52 shows the results of the FWHM of NV0 inside the ND for PL, CL and simultaneous PL and CL. The evolution is similar to that of CL in bulk diamond, but is even more pronounced. The behavior is similar between PL and CL, except for the fact that PL FWHM is increased by 1 nanometer. PL signal is also more affected by noise, which is to be expected as a result of the out-of-focus nanodiamond samples discussed before.

The origin of the extra FWHM of NV0 in PL is unclear at the moment. It is not caused by laser heating, as the simultaneous PL and CL measurements show: The FWHM of the simultaneous PL and CL measurement is lower than the FWHM of the sum of the previous PL and CL measurements, as figure 52 shows. This means that the FWHM of the CL signal is not increasing under a laser beam, and it may actually be decreasing.

Figure 52 also shows that the evolution with temperature of the NV0 peak full width at half maximum under CL is similar to that of the bulk diamond, shown in figure 42. However, there are two significant differences between the respective CL emissions: Intensity is much higher in nanodiamond, likely due to the higher doping concentration, and the growth of FWHM with

temperature is also higher in ND. These differences point to NV0 cathodoluminescence as a better sensor in nanodiamond than in bulk diamond. Hence, we proceeded to study this peak in more detail.

6.3 Secondary peaks in nanodiamond cathodoluminescence spectra

As discussed in the previous section, the NV0 CL peak appears to have good properties for temperature sensing. However, the fact that there are significant differences between the properties of the peak in the two types of diamond means that there may exist other differences in the spectra.

Hence, we proceeded to repeat the study done in section 5.3, with a similar procedure: CL measurements were performed in two separate regions, from 200 to 350 nm using the 1800 gr/mm grating; and from 350 to 800 nm, using the 600 gr/mm grating, for a temperature range of 5-300 K.

Similarly to the case of bulk diamond, the minimal temperature was likely higher than 5 K, due to the black body radiation emitted by the mirror, as discussed in section 3.2.

There were also some differences between the three substrates used: Most notably, the SiO_2 capped wafer experienced strong charge accumulation, which limited the beam current we could use, and therefore the brightness. The InGaN LED showed the CL contributions of both the nanodiamond and the LED. Hence, for this initial discussion, we will focus on the CL spectra of nanodiamonds on silicon. We will also compare the spectra of the nanodiamond clusters with those of individual nanodiamonds.

The thermal sensing method we propose would be based on measuring the emission of a single nanodiamond. Hence, it may seem counterproductive to study nanodiamonds concentrated in clusters. However, the clusters can give averaged information on the behavior of our samples and, therefore, provide us with an understanding of how external factors, such as current, affect the nanodiamond. In addition, observing the differences between clusters and isolated samples led us to a better understanding of our system.

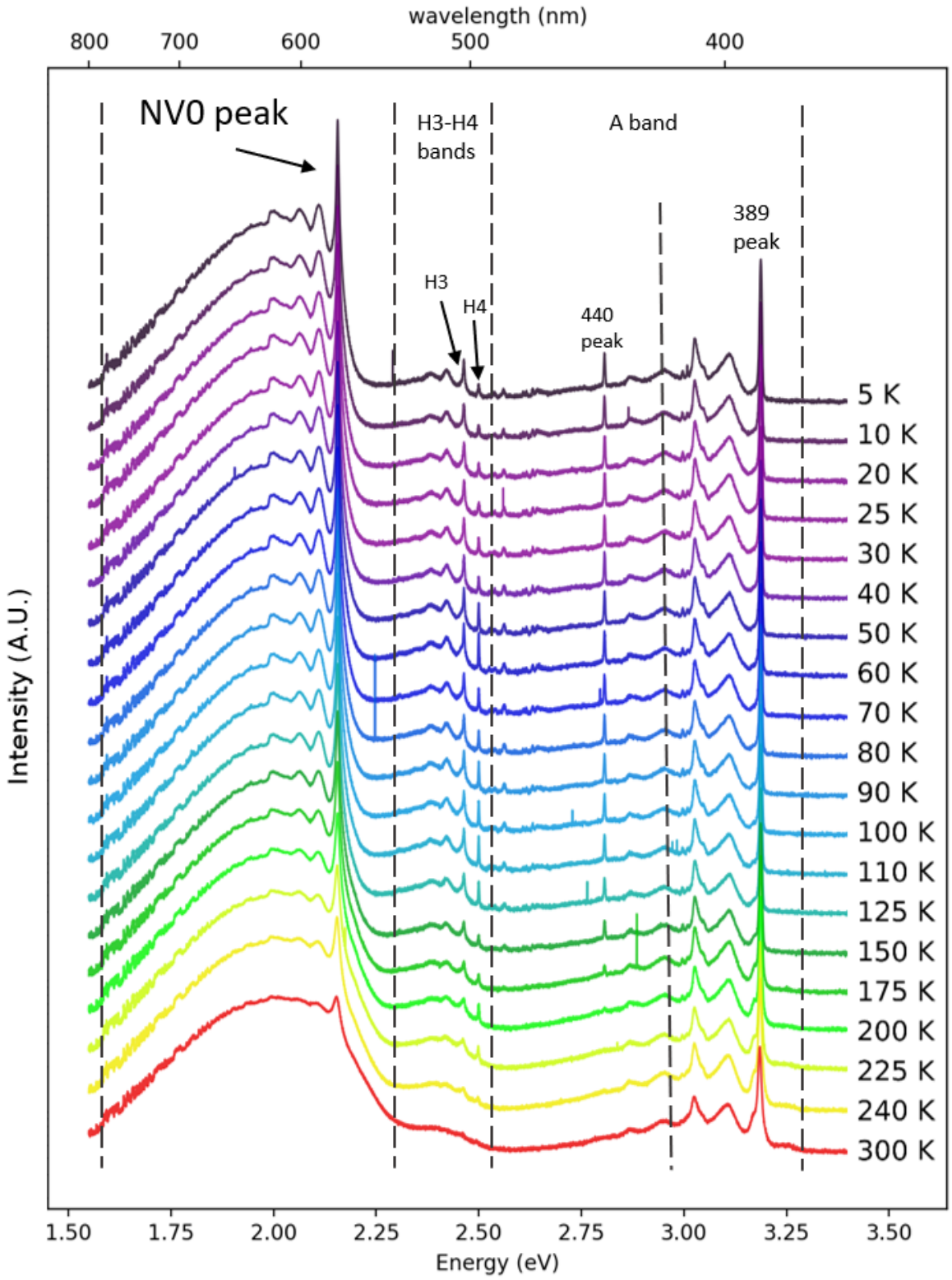


Figure 53: Full CL spectra of nanodiamonds deposited on Silicon for multiple temperatures. The intensity axis used a logarithmic scale. Measurements were done by irradiating a 5 µm x 5 µm region of a large nanodiamond cluster. The acceleration voltage was 3 kV, the probe current was set to 511 pA, and the exposure time was 5 s. The penetration volume in diamond for these conditions corresponds to a lateral width of 64 nm.

Figure 53 shows the cathodoluminescence spectra of a nanodiamond cluster on silicon in the visible range. The main peaks and their relative intensities were similar for all three substrates. We will proceed to describe the peaks and their differences, both between clusters and isolated samples, as well as those with the bulk diamond spectra discussed in section 5.3.

6.3.1 Phonon-assisted exciton peaks

One of our first observations was the complete lack of CL phonon-assisted exciton peaks in the nanodiamond sample. For this reason, the ultraviolet CL spectra are not shown here, as they did not contain any peaks useful to our study.

As discussed in section 5.6, the phonon-assisted exciton peaks had proven to be one of the best temperature sensors at low temperature. Hence, their absence supposes an obstacle to our work. However, since the kind of devices we are focused on studying operate mostly around room temperature, and the phonon peaks are not useful in that range, so this is far from an irrecoverable setback.

6.3.2 389 nm peak

As discussed in section 5.3, the 389 nm peak has an unknown origin, but appears to be related to nitrogen defects. The peak has been observed to be more intense in diamonds with lower concentration of nitrogen impurities [86], but in our case it was brighter in nanodiamond than in bulk. Since the concentration of nitrogen was higher in ND, as can be seen by the higher intensity of the NV0 peak, there is likely some other mechanism that enhances the 389 nm peak emission in our nanodiamond sample.

The behavior of the peak with temperature was very similar to that observed in bulk diamond, with the extra intensity being the only remarkable difference. The 389 nm peak had already shown some potential in bulk as a temperature sensor, so after observing the intensity increase, we decided to experiment with it.

However, the sensibility of the peak was still low, and in the case of single nanodiamonds intensity could vary enormously from sample to sample, being completely absent in about a fourth of them. As our goal requires single nanodiamonds to be standalone temperature sensors, we abandoned the 389 nm peak in the end.

6.3.3 A band

A spectral feature not present in the previously studied bulk sample, the A band is a broad but weak emission band that ranges from 380 to 480 nm. The band has been attributed to sp^2 defects in the network of sp^3 structures of diamond at incoherent grain boundaries and/or dislocations [127]. As the nanodiamond clusters are polycrystalline and have a large surface area, a much higher presence of the A band than in the bulk monocrystalline diamond is to be expected.

As a weak band that overlaps with other peaks, the A band does not help us in our purpose of thermal characterization. However, since it is associated to the crystalline interface, it can provide some insight into the sample structure.

Notably, the intensity of the A band was weaker in isolated ND compared to concentrated clusters. This points to isolated ND having a lower edge-to-surface ratio, which may hint to a tendency for more polycrystalline ND to concentrate in the clusters.

6.3.4 440 nm radiation peak

The 440 nm radiation peak has a very similar behavior in the nanodiamond cluster as it had in bulk diamond, with only a couple small differences: The intensity is slightly reduced at low temperature, and the peak remains up to higher temperatures, only disappearing above 200 K.

On individual nanodiamonds, the 440 nm peak disappeared at much lower temperatures, being completely absent at 20 K in some cases. The peak was also less intense in these isolated samples. This lack of a consistent presence, compounded with all the issues of the 440 nm peak already

discussed in bulk diamond, made us discard the peak for temperature sensing once again.

6.3.5 H3 and H4 band

The H4 band appears once again, now accompanied by the H3 band. The H3 band has a similar origin to the H4 band: Radiation damage on samples with nitrogen doping and vacancies. However, boron has been observed to suppress the H3 center [128]. This helps explain why we did not see this peak in the bulk diamond, since this sample had an opaque boron-doped layer, as shown in figure 29.

As seen in figure 53, the H3 peak is more intense than the H4 in nanodiamond clusters. This was not always the case for isolated samples, in which the relative intensities of H3 and H4 were not consistent. The intensity of both peaks was much lower in the isolated samples studied, potentially disappearing above temperatures as low as 20 K.

The radiation damage peaks do not show any potential for temperature sensing, similarly to the bulk case. However, the presence of the H3 band shows that these nanodiamonds have not received a treatment involving boron.

6.4 Nitrogen-Vacancy center cathodoluminescence in nanodiamond

As figure 53 shows, the evolution of the 575 nm neutral nitrogen-vacancy peak with temperature in nanodiamond is similar to that observed in bulk diamond, which was shown in figure 39.

However, as mentioned in section 6.2, there are two main differences between this CL peak in the two types of diamond: NV0 is brighter in the nanodiamond sample than in bulk, and the broadening with temperature is more pronounced.

The increase in emission intensity is expected due to the higher doping, and is an unambiguous positive for our goal: Higher intensity under the same beam conditions means a larger signal-to-noise ratio, and therefore higher accuracy. The extra broadening means higher sensitivity in

theory, but it could cause problems with accuracy if it is not homogeneous between samples. Compounding this issue is the lack of proper understanding of the theoretical origins of the NV0 thermal broadening in the first place. Hence, a careful experimental approach is required to properly determining the factors causing the broadening and the accuracy of any temperature model.

6.4.1 Peak fitting in nanodiamond

After some measurements in both isolated nanodiamonds and clusters spread on SiO_2 and Si wafers, we decided to focus our initial modeling attempts on the emission of nanodiamond clusters on top of silicon. Silicon was chosen over silicon oxide for the same reason discussed in section 6.3. The clusters were chosen over isolated nanodiamonds because, as will be discussed in section 6.4.5, offered a very homogeneous emission, with constant emission properties between different samples.

As the shape of the NV0 peak was similar in nanodiamonds and in bulk, we tested the same modeling approach for the energy distribution, discussed in section 5.5: A Voigt profile with a linear noise band. The results were similarly positive making this model a good starting point. Examples of this model fit can be seen in figure 54.

However, we decided to test other fitting models, partly to attempt to improve the thermal resolution of our model, but also because testing different models may help us elucidate the theoretical origin of the thermal broadening of NV0; or at the very least discard some potential origins.

Maxwell-Boltzmann distribution

Current understanding of the NV0 peak postulates that thermal broadening is related to thermal coupling via phonons [129]. Hence, we tried to connect the peak to the Maxwell-Boltzmann distribution. This function gives information of how energy carriers (phonons in our particular case) distribute said energy at different temperatures, with higher temperatures leading to larger variances and averages.

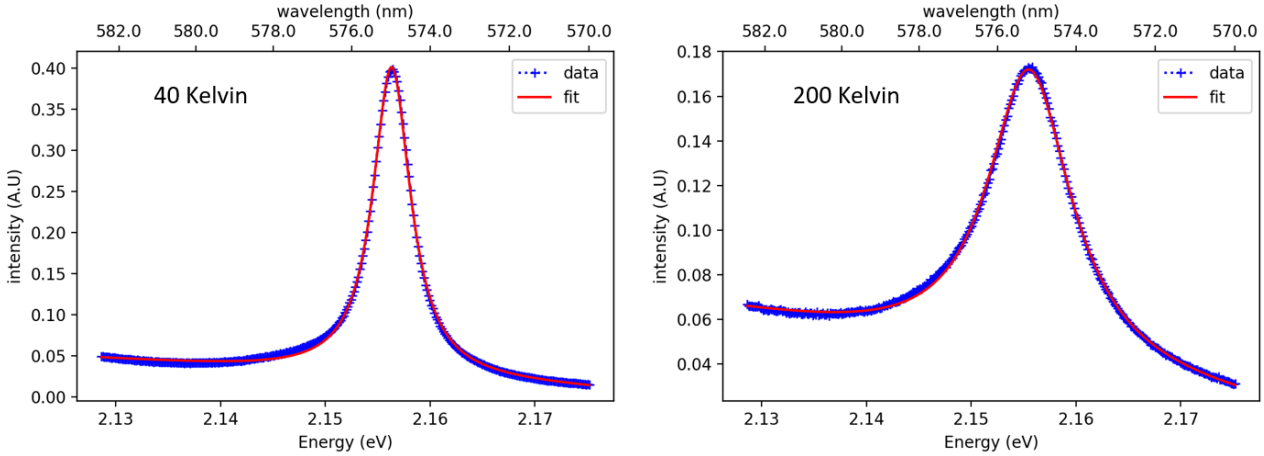


Figure 54: Neutral Nitrogen-Vacancy defect peaks and associated fits of Sigma-Aldrich Nitrogen doped nanodiamond at 40 and 200 K. Data was fitted to a Voigt profile with linear noise. The intensity axis used a linear scale, and each fit has been rescaled for visual clarity purposes. Fit was similarly accurate for all temperatures.

The original distribution was formulated to study the velocity of particles in a gas, with the following density function:

$$g(\vec{v})d^3\vec{v} = \left(\frac{m}{2\pi k_{\mathrm{B}}T}\right)^{\frac{3}{2}} \exp\left(\frac{-mv^2}{2k_{\mathrm{B}}T}\right)d^3\vec{v} \tag{8}$$

With k_{B} being Boltzmann constant, T the temperature of the system, and m the mass of the particle. By switching to kinetic energy, $E = \frac{1}{2}mv^2$, we obtain the following expression:

$$f(E)dE = g(v(E))v'(E)4\pi v^2 dE \tag{9}$$

$$f(E)dE = \left(\frac{m}{2\pi k_{\mathrm{B}}T}\right)^{\frac{3}{2}} \cdot \exp\left(\frac{-E}{k_{\mathrm{B}}T}\right) \cdot \sqrt{\frac{1}{2Em}} \cdot 4\pi\frac{2E}{m}dE \tag{10}$$

$$f(E)dE = 2\sqrt{\frac{E}{\pi}} \cdot \exp\left(\frac{-E}{k_{\mathrm{B}}T}\right) \cdot \left(\frac{1}{k_{\mathrm{B}}T}\right)^{\frac{3}{2}} \tag{11}$$

The term $4\pi v^2$ in the first expression comes from the Jacobian when changing to spherical coordinates: $dxdydz = \rho^2 \sin(\theta)d\rho d\theta d\sigma$. When integrating on the surface of a sphere of volume v, this Jacobian leads to the previous expression.

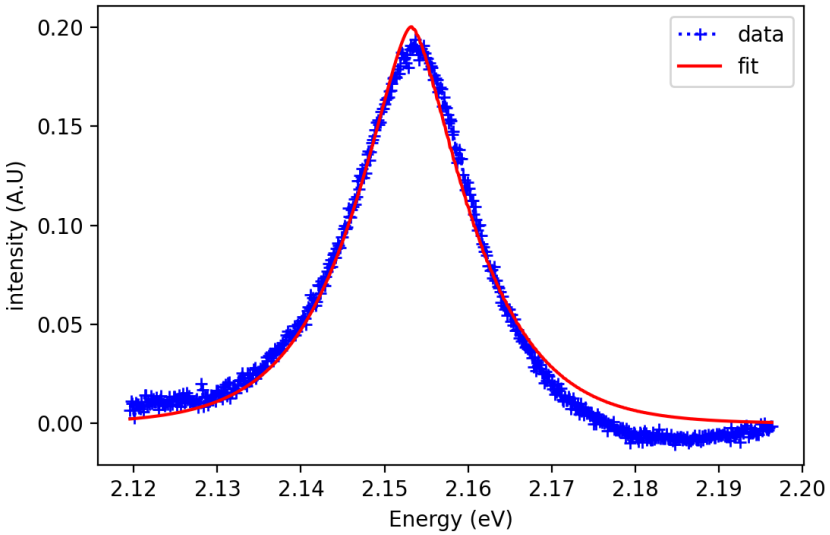


Figure 55: (Blue) NV0 peak of nanodiamond cluster on silicon at room temperature. (Red) Fit of said peak using a double Gaussian convolution, assuming NV0 state is directly interacting with a phonon during the decay. Temperature estimate by this method was 78 K

Equation 11 leads to an asymmetric energy distribution, which does not correspond to the behavior observed for the highly symmetrical NV0 peak, so the coupling is not as simple as a phonon-assisted decay. We hypothesized that, if phonon coupling was involved, the energy of said phonon could change, but still follow the same Maxwell-Boltzmann distribution. This would cause a symmetrical energy distribution for the NV0 state, centered at the transition energy, and with a probability distribution equal to the convolution of the Maxwell-Boltzmann distribution from equation 11 with a similar MB distribution, but negative. This would be equivalent to modeling the NV0 decay as absorbing and re-emitting a phonon.

We tested this model with a numerical convolution in python, since this convolution of two Gaussians had no analytical expression. Sadly, the model did not adequately match the shape of the NV0 peak, and the amplitude was associated with a much lower temperature than what the display shows. For example, the double Gaussian distribution reached the full width at half maximum of 22 meV, observed at room temperature in the nanodiamond sample, for a value of temperature below 100 K. This fit can be seen in figure 55

Hence, we can conclude that if the source of thermal broadening is a form of interaction between the NV0 peak and the energy distribution of the phonons, this interaction is not trivial or easy

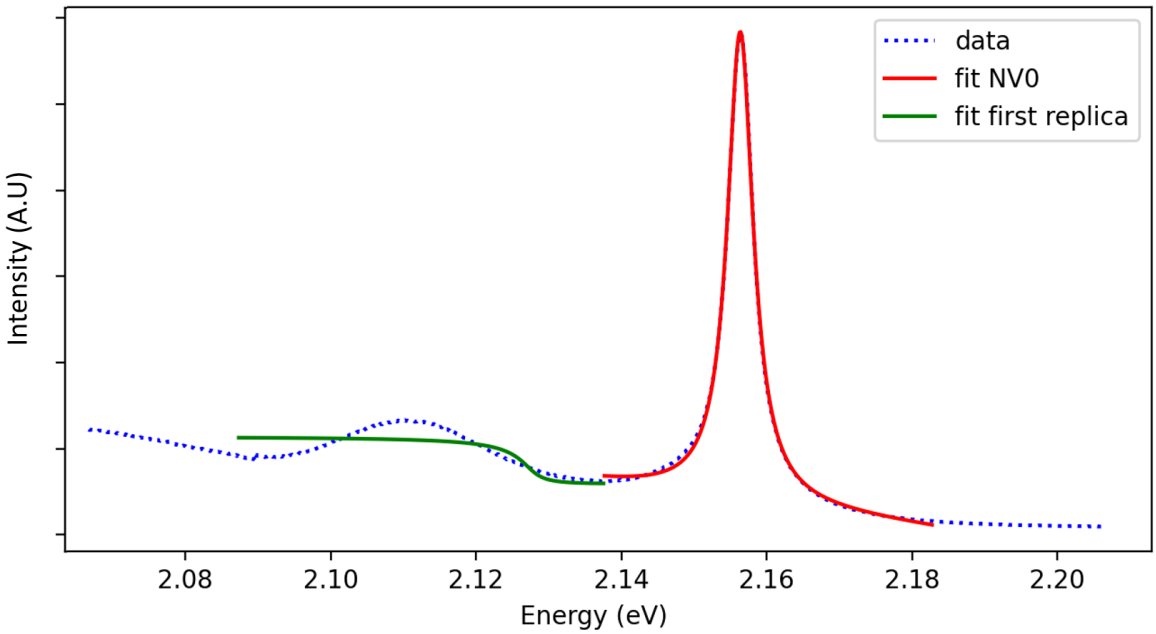


Figure 56: (Blue) CL signal of the NV0 peak and the fist replica in a nanodiamond cluster on silicon at 50 K. (Red) Fit of NV0 using a Voigt profile with linear noise. (Green) Fit of first replica via convolution of NV0 peak and Maxwell-Boltzmann distribution.

to model.

First phonon line in NV0

There exists a section of the NV0 peak that has not been discussed until now: The series of lower energy replicas that form a band all the way to 800 nm. These secondary peaks can be seen in figure 53. These replicas have been attributed to the interaction between NV0 and different phonon states, although the energy difference between NV0 and the first peak is roughly 45 meV, much smaller than the phonon energy in diamond at the Γ point (165 meV) [130]. The Γ point is the origin of the Brillouin zone, as discussed in section 2.1. Hence, similarly to the thermal broadening of the NV0, the relationship between the replicas and the vibrational modes is not straightforward.

Still, these replicas could help us access information on the phonon energy distribution, and hence the temperature. Therefore, we proceeded to study the behavior of the most intense of these peaks, the first NV0 replica at 585 nm.

We studied the possibility of a thermalized energy carrier being emitted during NV0 decay to be at the origin of the first replica. To test this hypothesis, we tried to model the first replica as the convolution of a Gaussian with the Voigt fit for the NV0 peak. The results of this peak at 50 K can be seen in figure 56.

This figure shows that this convolution is not adequate to explain the shape of the first NV0 replica. Hence, as was the case for NV0, the relationship between the first replica and the phonon states is not trivial, and we have no clear path to accessing the MB distribution of our phonon states.

Further study of the first replica revealed a much smaller change with temperature than NV0, with the main parameter evolving being intensity. This led us to compare the intensity of the two peaks and study how this ratio evolved with temperature.

As previously discussed, intensity is not usually a good thermal sensor in itself, as it is a parameter highly dependent on experimental conditions. However, as the ratio between two intensities is adimensional, we hoped that this magnitude would provide us with information about the temperature without the drawbacks normally associated with intensity. Unfortunately, as can be seen in figure 57, the ratio between the NV0 peak and the first replica was found to be dependent on beam conditions and non-injective with temperature. Hence, it was discarded as a potential temperature sensor.

Improving the Voigt fit of NV0

As the study of the first replica was unfruitful, we once again focused our efforts on the fit for the NV0 peak itself. As it was the case for Bulk diamond, the fit combining linear noise with a Voigt fit is in good agreement with the experimental data. However, there is a small disagreement between the two: The experimental peak has a slight asymmetry, that the Voigt profile cannot account for.

Our current hyphothesis is that the signal from first NV0 replica overlaps with the lower energy half of NV0, slightly disturbing it and breaking the symmetry ever so slightly. In order to address this issue, we tried to fit only the higher energy part of the NV0 signal to a Voigt peak, and

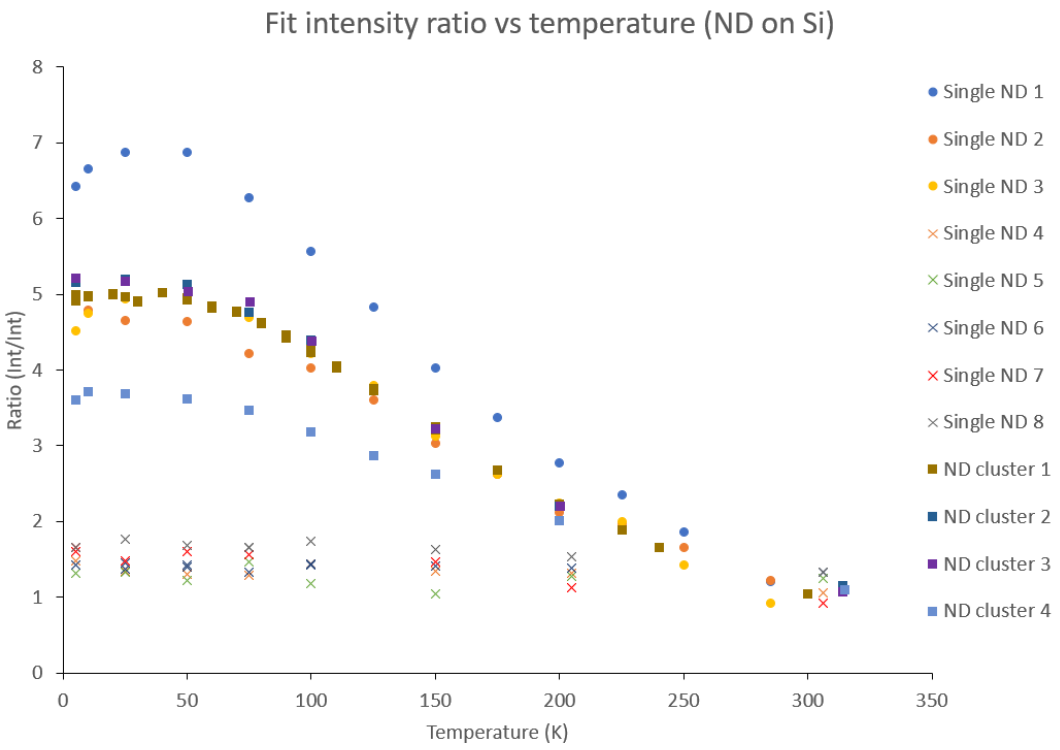


Figure 57: Ratio between the peak intensity of NV0 and its first replica versus temperature for different ND samples deposited on top of silicon.

compare the results between the two fits.

Overall, the fits were very similar for the two methods, with only significant variation between the two appearing at higher temperature, in which case the intensity is lower and the signal-to-noise ratio is higher. In these cases, the fit using only half a Voigt fit was more stable with noise, so we switched to this fit model to determine the FWHM of the peak.

As discussed in section 5.5, the Voigt profile is a convolution of a Gaussian and a Lorentzian, with the σ and γ parameters being those of the Gaussian and Lorentzian parts. If one of those parameters is close to 0, the associated distribution becomes a Dirac delta, leading to the Voigt profile becoming equivalent to the other distribution.

Interestingly, there was a notable difference in the way these relative contributions evolved in nanodiamond with respect to bulk diamond: In the cluster region, outside very low temperatures (50 K or below), the value of σ for the spectral fits is of the order of 10^{-8} nm.

Hence, computational cost could be reduced by fitting the peak to a simpler Lorentzian profile above these temperatures. However, in the case of the isolated ND, the Gaussian σ term was present at potentially any temperature. Since our end focus is single nanodiamond, we kept the Voigt profile for all temperatures.

6.4.2 Temperature evolution of NV0

After concluding that the Voigt profile is the most adequate profile to fit the main NV0 peak, and that said peak is the best potential candidate for a temperature sensor, the next step is to study the evolution of said fit with temperature.

As it was the case before, we will focus on the measurements on nanodiamonds on top of the silicon substrate. Three sets of measurements were performed, one of four isolated nanodiamonds, changing the beam spot between each other for each temperature, and another two measurements done by CL scanning on 5 µm by 5 µm areas, on two separate large clusters. One of these measurements corresponds to the one shown in figure 53. No noticeable differences were found between the two cluster spectra.

These measurements and their analysis were published in a special issue of Physica Status Solidi under the title *Temperature-sensing Cathodoluminescence spectroscopy of highly Nitrogen-doped nanodiamonds for a large spatial resolution thermal probe* [2].

As discussed in section 6.1.1, the size and shape of the individual nanodiamonds was significantly heterogeneous. For the measurement on isolated nanodiamonds, we chose four samples that were among the largest, with sizes between 250 and 300 nm. This was done to ensure a high enough CL brightness to properly measure the peak on a short time frame, and also ensure the excitation volume remain fully inside the studied sample. According to CASINO simulations, the excitation volume for these beam conditions has a width of 64 nm and a depth of 70 nm, so we can be confident that the CL signal will originate almost exclusively inside the chosen nanodiamond.

The individual nanodiamonds were significantly less bright than the cluster, which meant we had to double the measurement time, from 5 s to 10 s, to ensure enough signal to achieve an adequate

fit. The lower intensity is likely due to the saturation of the NV0 defect. For the chosen current of 511 pA, the electrons will be emitted at a rate of roughly 0.3 ns per electron, well below the NV0 lifetime, which as discussed in section 6.2.1 was about 15 ns at room temperature. Further discussion of the ND lifetime will be addressed in section 6.7.

As a single electron can excite multiple NV centers, the NV0 is likely saturating when studying the single ND samples, making the number of NV centers the limiting factor for the intensity for the isolated samples. Since we observed an increase in intensity of a factor of two between the least bright and the brightest nanodiamonds in our set of four measurements, we can conclude that the density of NV centers between different samples is also highly heterogeneous.

As discussed in section 6.4.1, the model for the CL signal of the NV0 peak was a Voigt profile of the higher energy half of the peak, combined with some linear noise. As a Voigt profile, we have access to three basic parameters: The center of the peak, the σ, and the γ, on top of the intensity of the peak itself. In order to be a good temperature probe, any parameter needs to follow predictable evolution with temperature that is consistent between samples.

Normalized intensity

The intensity of NV0 emission has already been demonstrated to be a good temperature sensor in PL measurements by Pedroza-Montero *et al.* [131]. However, as discussed in section 5.5, intensity has a big intrinsic limitation: It will depend on any factor that affect the number of counts in the detector, such as the density of NV0 defects in the nanodiamond, the electron beam conditions, and the collection efficiency of the spectrometer.

Separating the contribution of the temperature to the intensity from all those other factors is unfeasible. So, even though peak intensity evolves strongly with temperature, it cannot be used directly as a thermal sensor. Hence, we studied the intensity of the samples normalized to the highest value of each series. By normalizing the intensity, we remove all the secondary contributions, by assuming they remain constant for the duration of the measurement, and therefore the only change in normalized intensity is induced by temperature, enabling us to potentially use it as a relative temperature sensor.

Figure 58 a) shows this normalized intensity for each sample. Similarly to the bulk case, there appears to be a linear relationship between temperature and normalized intensity between 70 K and 200 to 300 K (depending on the sample). However, the slope is slightly different for each sample, so the normalized intensity does not even appear to be useful as a relative temperature sensor.

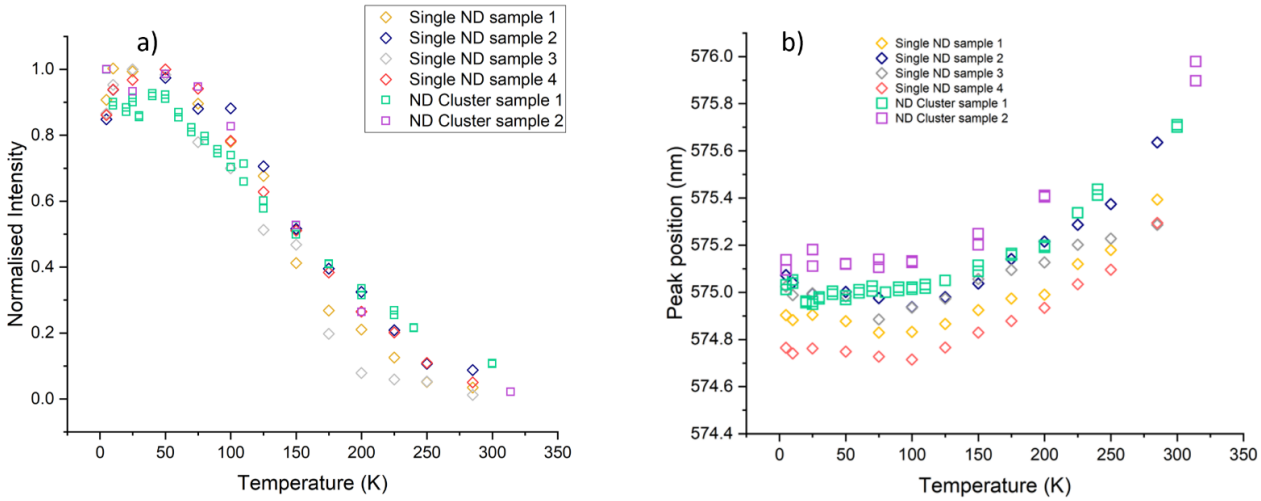


Figure 58: Parameters extracted from NV0 peak fit to a half Voigt profile with linear noise at different temperatures. The nanodiamonds were deposited on Silicon, the clusters were scanned on an area of 5 µm by 5 µm and the isolated samples had a size between 250 and 300 nm: a) Normalized intensity for each sample . b) Peak position.

Peak position

The next parameter we studied was the peak position, which can be seen in figure 58 b). Peak position is intrinsically a better parameter than intensity, since it does not depend of beam conditions and collection efficiency. And as the figure shows, there appears to be a consistent trend line for this parameter shared between all samples, and which is linear above 125 K. The main difference between the individual samples appears to be a displacement by a fixed value intrinsic to each measurement.

This type of fixed displacement of the wavelength can sometimes be caused by improper mirror alignment. However, this can not be our case, since for the study of the isolated nanodiamonds the mirror had to be realigned four times at each temperature to capture the signal of all the samples. Hence, the fixed displacement of the NV0 peak center appears to be intrinsic to each

sample.

Another limitation of the peak position is the small shift with temperature, less than one nm in wavelength between 5 K and room temperature. As such, the parameter will be quite sensitive to noise, requiring bright samples and long measurements to ensure proper thermal sensing.

Despite these issues, the peak position has some potential as a thermal sensor. However, a better parameter was found in the form of the full width at half maximum (FWHM), which was the one in which we focused the bulk of our efforts.

Full width at half maximum

Although the Voigt function has two remaining parameters σ and γ, none of them work well individually as a thermal sensors. This is because both contribute to the main parameter affected by temperature, the full width at half maximum. Similarly to what happened for the bulk case, combining σ and γ into the FWHM leads to a stronger and more consistent dependence with temperature than using the two parameters separately. The calculation of the FWHM was done once again using Olivero and Longbothum expression [98].

As it was discussed in section 5.5, for the case of bulk diamond, the full width at half maximum has a clear evolution with temperature, but as the intensity decreases with temperature, the signal-to-noise ratio decreases and the error rate grows.

For our nanodiamonds, the NV0 peak has a much larger total intensity, causing the error rate to remain low even at room temperature. The growth with temperature of the FWHM is also slightly more pronounced, and we can monitor it all the way to 6 nanometers, which allows for higher sensitivity. Similarly to the case of bulk diamond, the evolution of the parameter is very slow at lower temperatures, limiting thermal sensing in this range, but the slope similarly becomes significant enough above 150 K.

Figure 59 shows the evolution of this FWHM with temperature for all of our samples. As the growth of this parameter with temperature is much more pronounced than in the bulk case, we need a different model than the one described in section 5.5. After some experimentation, we

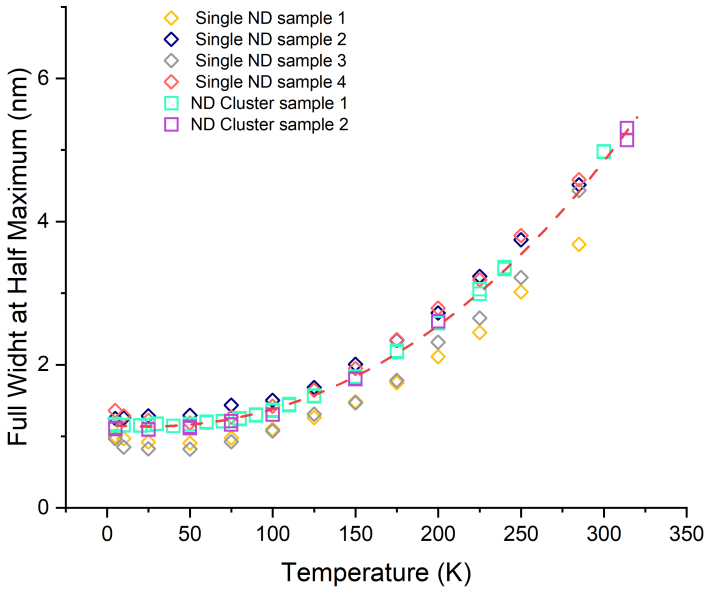


Figure 59: Full width at half maximum extracted from NV0 peak fit to a half Voigt profile with linear noise at different temperatures. The nanodiamonds were deposited on Silicon, the clusters were scanned on an area of 5 by 5 µm and the isolated samples had a size between 250 and 300 nm.

found that a simple cubic polynomial, shown in the figure as the red dashed line, allowed for a good fit of the clusters behavior.

Similarly to the case for the peak position, the FWHM follows the same trend with temperature in all samples, but appears is displaced by a different fixed value for each ND. However, unlike peak position, FWHM behaves differently between single ND and large clusters. For isolated nanodiamonds, there is a common trend line, but each sample appears to displace from it by a fixed value. In the case of the clusters, the trend is exactly the same for the two measurements, without any unique displacement. To ensure this was not just due to chance, we performed a similar measurement on a third cluster on top of silicon. The result was identical confirming that unlike peak position, FWHM is stable on different clusters. The results of the FWHM for this third cluster at different temperatures will be shown in section 6.4.5, in Figure 61.

The thermal resolution of the model can be estimated from the standard deviation between the (normalized) spectral data and the half-Voigt fit. This estimation gives us a thermal resolution of about $\pm$ 5 K at room temperature for the clusters, and $\pm$ 10 K for the isolated nanodiamonds.

The systemic deviation from the model of the isolated samples shown in figure 59 is larger than this error rate, hence the fixed displacement from the model of the isolated nanodiamonds is not due to the increase in error rate, but appears to be an intrinsic property of the sample.

The polynomial function used for the fit was:

$$f(T) = \beta_3 T^3 + \beta_2 T^2 + \beta_1 T^1 + \beta_0 \tag{12}$$

With $\beta_3 = 4.53 \cdot 10^{-9}$, $\beta_2 = 5.78 \cdot 10^{-5}$, $\beta_1 = -3.76 \cdot 10^{-3}$ and β_0 being sample dependent, but for the particular case of the clusters on top of silicon having value of 1.24.

As the isolated nanodiamonds are significantly less bright than the cluster, the exposure time and therefore thermal resolution will differ significantly between the two. As the exposure time of the clusters was only 0.5 s, the thermal resolution of these samples will be 3.5 $\mathrm{K}/\sqrt{\mathrm{Hz}}$. In comparison, the exposure time was 10 seconds for isolated samples, leading to a thermal resolution of 32 $\mathrm{K}/\sqrt{\mathrm{Hz}}$.

Our analysis shows the potential of the NV0 FWHM as a thermal probe, but leaves an important question unanswered: The origin of the fixed shift from the trendline in individual nanodiamonds. As our potential method requires us to be able to extract the temperature from a single nanodiamond, answering this question is crucial for our work. Hence we proceeded to study the difference between isolated samples and clusters.

6.4.3 Evolution of NV0 lifetime with temperature

The study of the CL spectra versus temperature of the NV0 peak in ND shown in section 6.4.2 granted us access to multiple peak parameters and their evolution with temperature. However, the CL spectra by itself does not allow us to access the lifetime of the defect, a potentially temperature-sensitive parameter. In order to access its value, we used the setup described in section 3.5. To ensure only the lifetime from the NV0 center was being measured, two filters were used: A long-pass filter of 550 nm, and a short-pass filter of 600 nm, both part of Thorlabs hard-coated edgepass filters series [132].

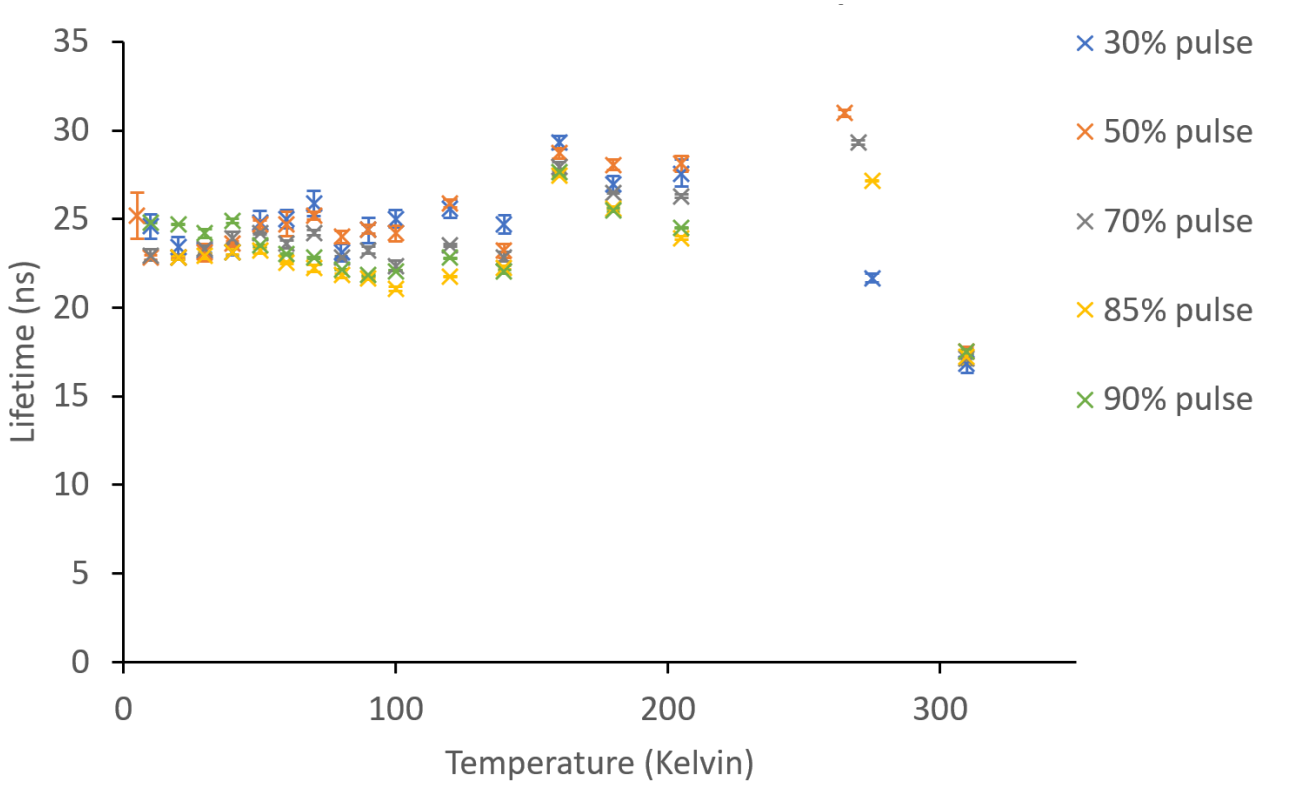


Figure 60: Lifetime of a 5 µm by 5 µm area on a ND cluster spread on top of the Silicon substrate. Measurement was performed using the setup described in section 3.5, for different values of the beam blanker active percentage duty time. A higher percentage means a lower total current.

The measurements were done on a 5 by 5 µm area on a ND cluster spread on top of the silicon substrate. The electron beam was set at 5 keV and 3 nA, and the exposure time was 120 seconds per measurement. The beam blanker was operated in continuous mode to ensure a high intensity, and therefore a low error rate. The pulse connected to the beam blanker had a total period of 1 µs. The measurements were repeated for different values of beam blanker active percentage duty time to study the effect of the beam current on the lifetime. For example, an active percentage duty time of 50% means the beam is blanked in intervals of 0.5 µs, causing half the current to be loss. Meanwhile, an active percentage duty time of 90% means the beam is blanked in intervals of 0.9 µs, and the total current is ten times lower than the non-blanked beam.

The lifetime vs temperature for the different active percentage duty times can be seen in figure 60. The estimated lifetime at room temperature obtained by combining all measurements was 17 ± 1 ns. This value confirms the results of room temperature PL lifetime obtained in section 6.2.1, showing that NV0 lifetime is indeed shorted for the nanodiamonds that for bulk diamonds.

Interestingly, the lifetime of the NV0 is not only larger at lower temperatures, but also appears to grow with temperature until it quickly decays above 260 K.

Figure 60 also shows that lifetime changes with the pulse active percentage time, a parameter that only affects the total current. Since all the measurements are performed on the exact same collection of ND, and the change in lifetime with pulse is larger than the error rate, the only possible explanation for this change is that NV0 lifetime is dependent on beam current.

NV0 lifetime in ND is know to be affected by multiple parameters, and even the same nanodiamond can change its lifetime over time, or by slight changes to the beam position [126, 133]. This lack of stability, combined with the current dependence and small evolution with temperature made us discard the NV0 lifetime as a potential temperature sensor.

6.4.4 Effect of ND size on NV0 emission

The result obtained in section 6.4.2 show that isolated ND are not as good as clusters for the goal of thermal sensing, due to a fixed deviation of unknown origin on each sample from the FWHM temperature model. However, this study was focused on very large nanodiamonds, much larger than those that would be used for thermal sensing. Hence, we performed similar measurements on smaller samples to see if this fixed deviation was also present.

In order to properly study the effect of ND size and shape on the emission, we need to image the nanodiamonds with high spatial resolution, since as discussed in section 6.1.1, the smallest samples are only a few nanometers in size, and the shape of the samples is also very heterogeneous. Hence, we performed a high resolution image with a second FESEM, a ZEISS Ultra Plus. The microscope was chosen for its higher spatial resolution of 1 nm, which allowed us to discern the shape of the ND properly. Since this new FESEM had no CL capabilities, we then found the same area in the original setup, and performed CL scanning on some of those samples. Although the samples could be seen in both SEM setups, the better resolution on the new FESEM allowed us to measure the size and shape of the nanodiamonds with better accuracy.

Figure 61 a) shows the higher resolution SEM image and indicates the samples that were later scanned in CL. Figure 61 b) shows the evolution with temperature of the FWHM of these samples, and compares it to the theoretical model and the results on the other clusters on silicon.

From figure 61 is clear that, despite working very well on the ND clusters, our model does not accurately predict the evolution of small isolated samples. Unlike what was observed in section 6.4.2 for large isolated nanodiamonds, the smallest samples shown in figure do not simply deviate from the model by a fixed value, but fail to adscribe to it. In fact, the smaller the samples are, the more they deviate from equation 12.

Still, there may be hope for our method if we can understand the origin of the deviation, as even a small sample such as sample six (of about $1.86 \cdot 10^4$ nm^2) follows the model, albeit with a larger fixed deviation than the larger isolated nanodiamonds of figure 59.

The smaller samples had a lower CL intensity, which was expected due to the lower amount of NV0 centers. This lower intensity led to a worse thermal resolution, which was estimated once again from the deviation between the CL data and the half Voigt fit. The thermal resolution of the smallest isolated nanodiamonds was $\pm$ 30 K at room temperature. This lower resolution can explain why the adjustment to the curve show in figure 61 b) is not as good as with the larger samples of figure 59, but does not explain why the fixed deviation is larger than in bigger nanodiamonds. Hence, we need a better understanding of this fixed deviation and its origin.

6.4.5 Effect of cluster morphology on NV0 emission

As the results shown in sections 6.4.2 and 6.4.4 reveal, there are differences in the behavior of the CL NV0 peak between isolated nanodiamonds and clusters. ND clusters closely follow our theoretical model, while the isolated samples deviate proportionally to their size. Since the NV0 peak is the best candidate for a thermal sensor by a large margin, a great effort was made to understand the origin of these differences.

The most obvious potential explanation for this discrepancy would be the fact that the CL signal

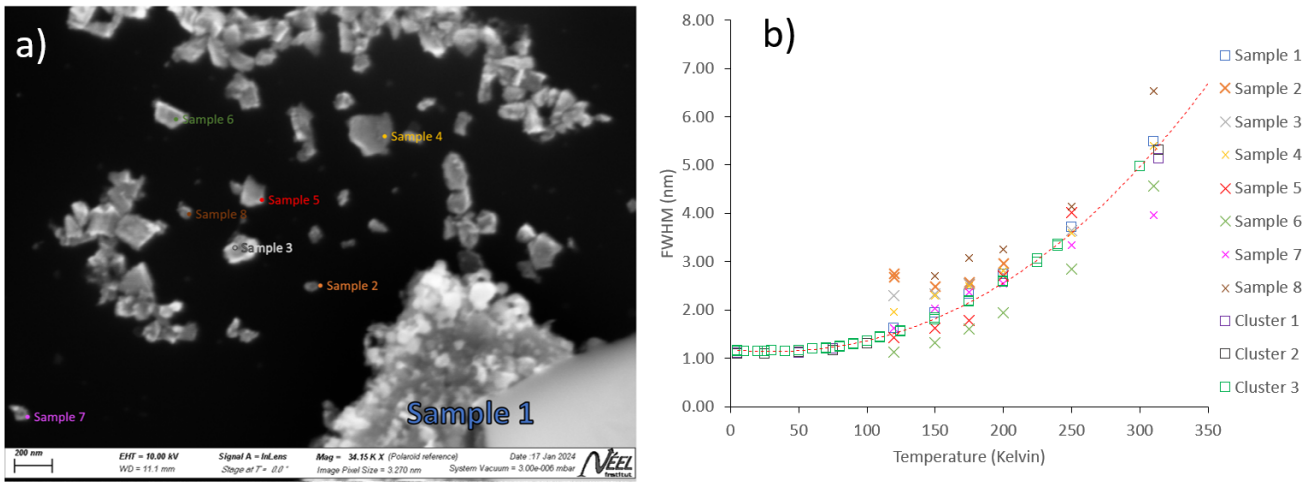


Figure 61: a) SEM image of a ND spread on top of silicon in a region with a large concentration of isolated samples. b) Evolution with temperature of the FWHM of the NV0 peak of nanodiamond samples on top of a silicon substrate. The SEM image shows the sizes and shapes of the isolated samples displayed in the graph. The signal from the clusters was obtained by scanning over a 5 µm size square. Beam energy was 3 kV.

from clusters is an average of a large collection of single samples, leading to a much more stable emission than a single isolated ND. In order to test this hypothesis, we once again performed spatially resolved CL mappings, similar to those used for the characterization of µLEDs in chapter 4.

In particular, we performed spatially resolved mappings of a medium size cluster in a 25 µm by 25 µm region at different temperatures. As this kind of measurement takes a potential long time, we worked under a higher current, 735 pA, while maintaining the acceleration voltage at 3 kV. This lead to a higher intensity, allowing us to lower the exposure time to 0.5 seconds per pixel. As could be seen in figure 6, back in chapter 3, this acceleration voltage in diamond corresponds with an excitation volume in which 95% of the electron beam energy will remain in an area of roughly 65 nm of width and 75 nm in depth.

In order to properly interpret the results of the measurements, we need to be able to estimate the number of ND excited on a pixel. Knowing the dimensions of the excitation volume, we can make a gross simplification and assume the ND in the cluster are perfectly spherical, have a diameter of 70 nm (the average size according to Sigma-Aldrich), and are distributed to maximum compactness, following a FCC lattice.

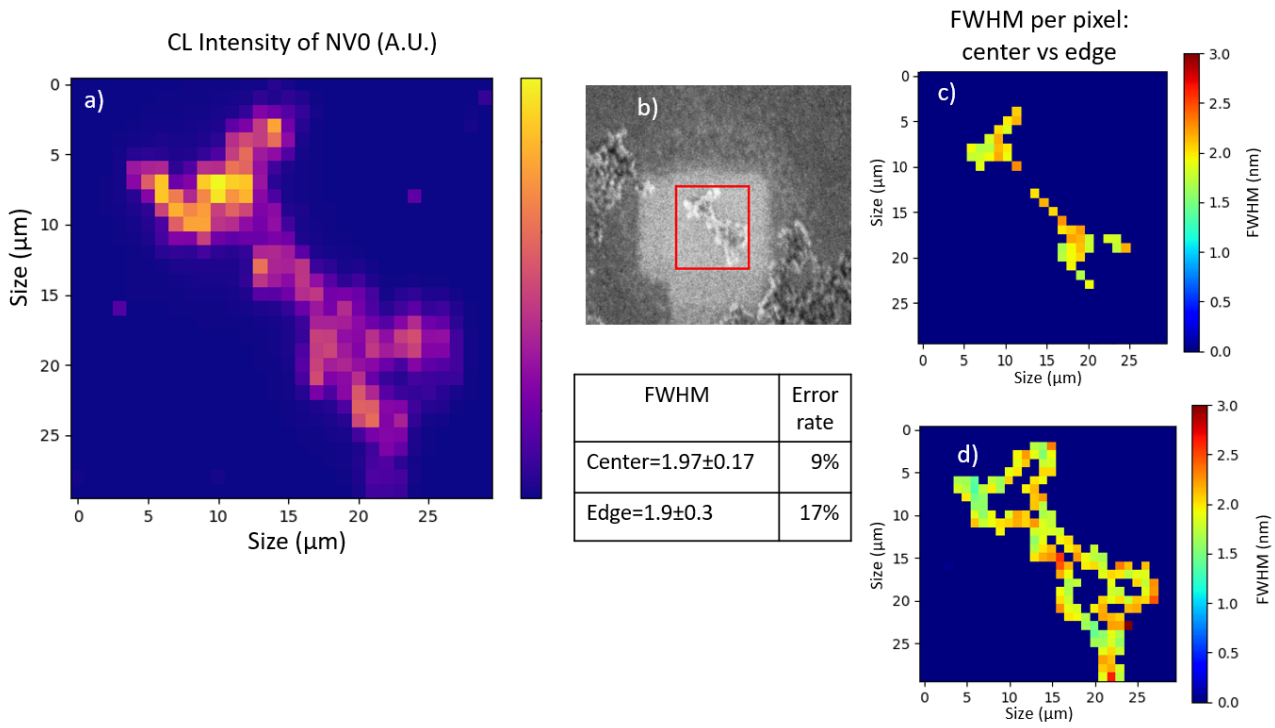


Figure 62: CL mapping of a medium size nanodiamond cluster on top of GaN. Measurement was performed at 150 K, under as beam of 3 keV and 735 pA. The exposure time was 0.5 seconds per pixel a) CL intensity of the NV0 peak. b) FESEM image of the cluster, with a red square showing the area studied by CL. c) Full width at half maximum of each pixel at the interior and d) edge of the cluster.

Performing simulations based on this approximation leads to an average excitation of 1.6 ND in each beam position on the cluster. Even though this is only a rough approximation, it allows us to estimate what the average standard deviation from the model will be of a single nanodiamond from the average standard deviation of a CL pixel. As we can assume the signal of a pixel is an average of all the nanodiamond excited for a beam in the pixel position, we can calculate the standard deviation from the model of a single nanodiamond in the cluster to be $\sqrt{1.6}$ times the standard deviation from the model of a CL pixel.

Figure 62 shows one of these spatially resolved CL measurements, at 150 K. The spatially resolved measurements were done on the LED substrate, as this substrate gave us access to the ND layer depth, as it will be discussed in section 6.4.6. The differences induced by this new substrate will be discussed in section 6.4.7.

Figure 62 shows that the averaging hypothesis is only partially complete. When studying the deviation from the model, we found that the behavior of the nanodiamond was different between

the edges and the center of the cluster. The (normalized to the mean) standard deviation of a single nanodiamond in the interior of the cluster is about 9%, while at the edge this standard deviation is almost doubled. Similar results were obtained at all temperatures for this cluster.

This result shows there is some effect at the edges of the ND clusters that is detrimental to the stability of our model. In order to confirm these results, we performed a new thermal series of spatially resolved CL measurements on a second ND cluster on top of GaN. This new cluster was observed under a much smaller area of just 3 µm by 3 µm. The imaged region of the cluster was also away from the edges, to eliminate their potentially detrimental effect. The result was an estimated standard deviation from the model of 7% for an average ND inside the cluster, confirming the negative effect of the edge.

Performing a similar study on the single nanodiamonds shown in figure 61 gives an average deviation from the model of 21% per nanodiamond, somewhat higher than the deviation at the edge of the cluster. These similar values for the deviation seem to hint at a common origin.

6.4.6 Using an InGaN LED substrate to study ND cluster depth

The explanation of why the edge of ND clusters leads to such a drastic increase in deviation from the model was found by studying the vertical depth of said clusters. This is not a value that could be accessed directly from a FESEM image, at least not without making a vertical cut of the sample, which would carry the risk of altering the cluster structure we were trying to study.

Instead, we took a different approach to measure this depth: we used the third deposition we prepared, the ND on top of an InGaN LED. As the deposition was performed similarly in all three substrates, we can operate under the assumption that the morphology of the clusters will be similar between this deposition and the silicon one.

The LED structure was the exact same as that discussed in section 4.1, as it was the exact type of commercial LED that Corentin Le Maoult used for his PhD. Hence, the only difference between this sample and the one studied during chapter 4 was the lack of etched µLEDs and

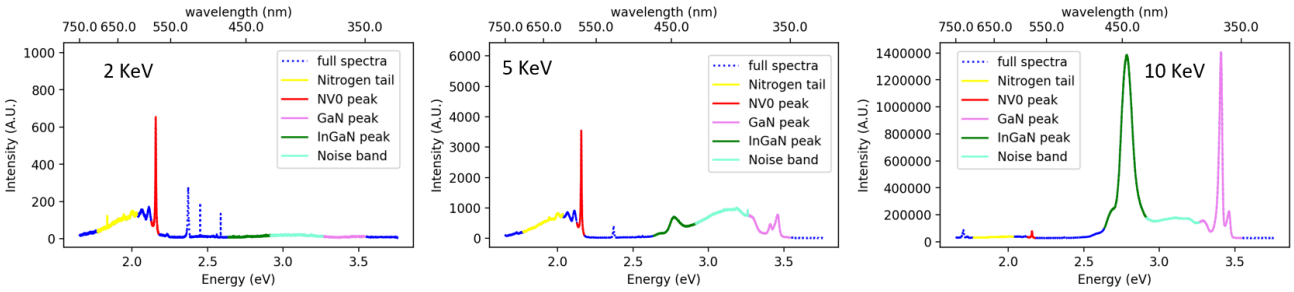


Figure 63: Full CL spectra at 5 K of a 5 µm square region of a ND cluster deposited on top of an InGaN LED for different acceleration voltages. As the penetration volume grows, the relative contribution of the InGaN layer to the total intensity goes from virtually zero to almost the entirety of the signal.

the surface passivation treatment.

The reason for using this substrate was the CL brightness of both the uppermost layer of GaN and the QW, which emit at 360 and 450 nm respectively. These are regions of the spectra with little to no ND CL signal at room temperature, as figure 53 illustrates. Hence, we can use this sample to test if we could simultaneously perform CL on the ND and the underlying sample. Not only that, by modifying the acceleration voltage, we can study how the proportions of the LED peaks change in respect to the diamond signal.

Figure 63 shows an example of one such measurement for different voltages. The figure shows it is possible to excite only the nanodiamond by using a low acceleration voltage, or to excite both ND and LED using a higher voltage. This means that, by performing spatial CL mappings on the LED wavelength at various acceleration voltages, and combining them with the CASINO simulations of the excitation volume in diamond for those voltages, shown in figure 6, we could calculate the thickness of the ND cluster at each point in the mapping.

Figure 64 shows an example of this kind of measurement at an acceleration voltage of 4 kV. As Figure 64 a) shows, most of the points in the mapping have an intensity above the noise level, which means that except for a small narrow area to the left of the imaged cluster, the ND layer has a width below the corresponding penetration depth in diamond of 130 nm.

Their estimated average width was 90 nm, but this width was highly inhomogeneous, with some clusters reaching more than 200 nm, and others staying below 50 nm.

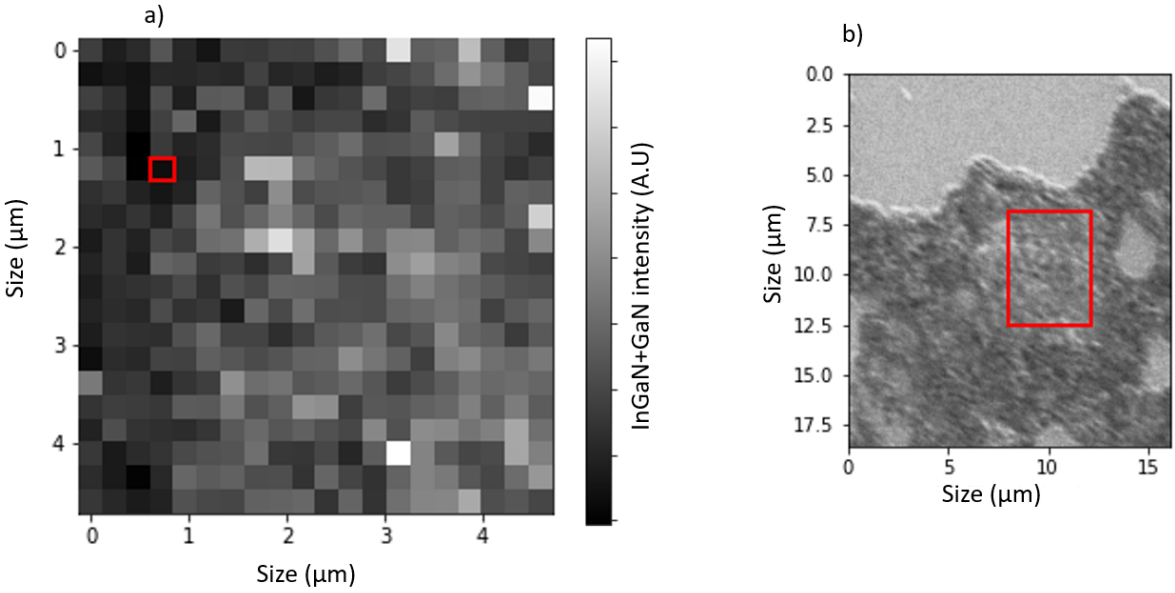


Figure 64: a) CL mapping of LED peak intensity and b) FESEM image of a ND cluster on top of InGaN LED sample. Measurement was done for an acceleration voltage of 4 kV, which corresponds to a penetration depth in diamond of 130 nm.

Notably, the edges of the clusters were very thin, reaching even below 14 nm, much smaller than the average diamond size. Hence, the smallest nanodiamonds seem to concentrate on said edges. This explains the previous results showing the higher deviation from cluster edges. The reason appears to be entirely the ND size, since as observed in section 6.4.4 smaller nanodiamonds lead to higher deviation.

6.4.7 Nanodiamond surface chemistry as the source of model deviation

The results discussed in section 6.4.4 show that the small ND do not follow our theoretical temperature evolution model as properly as large ones, displaying a much bigger variance in FWHM. The most direct explanation for this behavior would be the lower total amount of NV centers inside the smaller samples, leading to a total signal that is the result of averaging over a smaller amount of emitters, which causes to more variance. However, no correlation between deviation from the model and emission intensity was found, even between measurements under the same beam conditions, which contradicts this hypothesis, as a larger concentration of NV0 centers should lead to both lower variance and higher intensity.

This deviation can be better explained by the results from section 6.4.5. In said section, it was shown that regions inside the clusters with a higher concentration of small ND deviate from the theoretical model by a similar value than small isolated samples. Hence, there must exist an intrinsic difference in the CL emission of individual NV0 defects between small and larger nanodiamonds.

As it was discussed in section 6.1.2, ND surface chemistry has been known to impact the emission properties of NV centers, with surface oxidation harming their stability. This led us to hypothesize that Sigma-Aldrich may have developed a surface treatment which enhances NV luminescence. As smaller samples have a larger surface-to-volume ratio than larger ones, they would be more strongly impacted by this treatment. And due to the shape heterogeneity of the studied samples, the effect of any surface treatment would not only be more pronounced in smaller samples, but would also be more heterogeneous between samples.

In order to study the potential effect of this surface treatment on the ND spectra, we decided to remove it from one of the samples deposited on silicon. The removal was achieved by applying a drop of acetone to the surface after the ND were deposited, which was then removed with argon gas flow. Acetone is sometimes used to destroy the surface chemistry in ND [134]. Studying the sample after this procedure showed that the ND remained attached to the surface, but the CL and PL signal of the NV center had decreased by three orders of magnitude, almost completely disappearing, as can be seen in figure 65.

This result shows that the surface chemistry has a very strong impact on NV luminosity in nanodiamond, even for the largest ones (>200 nm). Acetone was chosen because is commonly used to clean bulk diamond, as it does not have an effect on its crystalline structure. Hence, the disappearance of intensity must be entirely due to changes in surface chemistry.

A strong confirmation of the effect of nanodiamond surface chemistry on the NV0 CL was obtained by comparing the emission properties of nanodiamond clusters on top of the silicon versus those on top of the galium nitride LED.

The behavior of the NV0 peak FWHM changed in the GaN deposition, but only for ND that were in direct contact with the surface. Figure 66 shows this effect clearly. ND on thin clusters

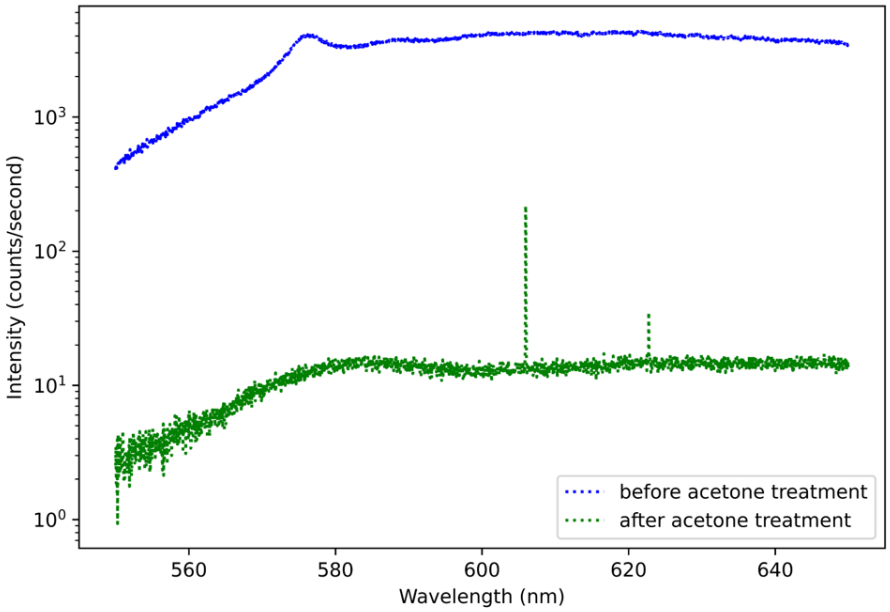


Figure 65: Comparison of CL spectra of the NV0 defect in ND sample on silicon before and after acetone treatment, under the same beam condition. Both spectra were obtained by scanning a 5µm by 5 µm area of a large cluster.

(between 40 and 90 nm, hence single or double layer) have their FWHM shifted 0.3 nm versus the silicon ones. ND in a thick cluster (mostly between 200 and 400 nm, although there were some depressions reaching 150 nm) have a behavior closer to the Si layer when probing them with lower energy electrons, as the signal comes mostly from the upper layers. These upper layers of the ND cluster will be composed almost entire of nanodiamonds that do not contact the GaN surface, since as figure 6 shows, for an acceleration voltage of 3 kV, 95% of the beam energy will enter the sample at 75 nm or less from the top of the cluster. This explains why the thick cluster in figure 66 behaves differently at 3 kV voltages than the thin cluster, as the ND in the thick cluster will not have their surface chemistry altered by the GaN surface.

The change in surface chemistry that led to a change in FWHM in Figure 66 could only be caused by the different substrates. The only other potential source of chemical changes at the surface would be oxidation due to air exposure, and we know from our results of section 6.4.4 that this is not the case. The measurements on ND clusters shown in figure 61 b) have identical FWHM behavior, despite being measured months apart, and the first one was performed the day after deposition. Hence, the difference in air exposure does not affect the FWHM.

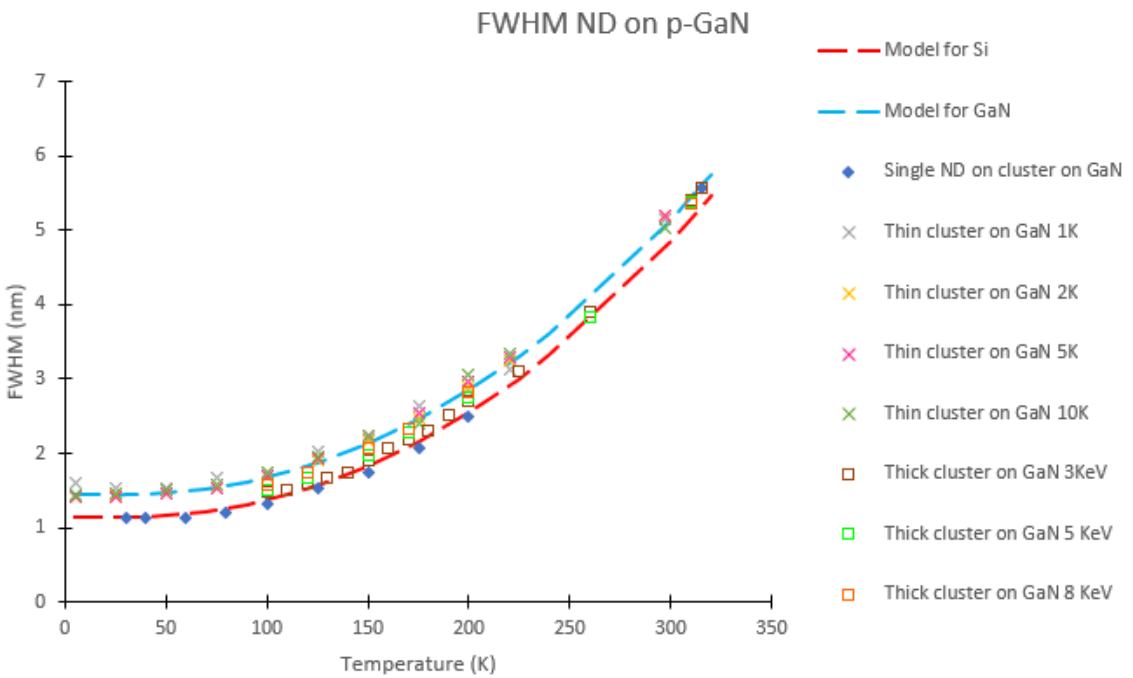


Figure 66: Evolution of NV0 FWHM with temperature for different ND samples deposited of top of GaN. The CL was performed on a 5 µm area for the clusters. The thin cluster ranged between 40 and 90 nm in width, while the thick cluster ranged between 200 and 450 nm. The single ND was very large, about 200 nm. The trendlines are the expected FWHM for ND deposited on GaN and Si.

However, as we raise the beam acceleration voltage, and increase the amount of photons coming from ND closer to the GaN surface, the FWHM shifts to match that of the thin GaN cluster. We know the electron acceleration voltage does not affect the FWHM of the ND, as we can see in the signal from the thin cluster, so the difference in surface chemistry are the only explanation for this change.

The reason for this surface effect may be related to electrical potential. Si wafers are expected to have a negative surface potential [135], while the surface of the LED was positively doped. The ND themselves have a weak positive surface potential, as seen from the negative zeta potential discussed in section 6.1.2.

As seen in figure 66 when probing a single large ND on top of a thick cluster deposited on GaN, the behavior is the same as ND on Si. This indicates the effect of other ND and Si is the same. As the ND have inhomogeneous shapes and sizes, the effect of surface chemistry on isolated samples is also inhomogeneous, and much more pronounced in the smaller ones due to the larger surface to volume ratio.

6.5 Thermal sensing on LED using nanodiamond

6.5.1 Joule heating measured from CL NV0 signal

As discussed in section 6.4.7, the main obstacle for our temperature sensing model is the effect of nanodiamond surface chemistry on the NV0 emission properties. Not only does the chemistry of the surface in which the ND are deposited causes a fixed displacement of FWHM, which is the parameter we employ to estimate the temperature, but also due to the inhomogeneous shape of the ND, each individual sample deviates by a unique value.

However, before working on addressing this limitation, it would be important to test beforehand if our method can actually capture Joule heating in an electrical circuit.

Fortunately, there is a relatively simple solution to our issue: The fixed deviation is stable for a given ND or collection of ND, and the FWHM of the NV0 is very stable below 50 K, not being

dependent on the temperature, but only on the surface-induced deviation. Hence, the process we can follow to measure the Joule heating using our method is as follows:

- We set the sample of ND on top of the InGaN LED on the FESEM chamber with the electroluminescence setup discussed in 3.6.
- We choose a region of an ND cluster that is thin enough to achieve proper thermalization. We can estimate the width of ND clusters on top of GaN via the method discussed in section 6.4.6.
- We reduce the temperature down to 5 K using the cryostage and we calibrate the value of β_0 in our model based on equation 12 for the chosen cluster.
- We go back to room temperature and we use the electroluminescence setup to operate the LED in which the ND cluster is deposited, causing Joule heating.
- We measure the NV0 CL signal for different voltages and apply our model to estimate the temperature.

As the InGaN LED is in operation, it will emit an electroluminescence signal at a wavelength of roughly 450 nm. In theory this signal should not affect the ND CL emission properties, and due to the difference in wavelength between the InGaN peak and the 575 nm NV0 peak, it should not cause an increase in noise. In order to ensure this is the case, we performed measurements for the LED in both forward and reverse bias. An LED operating in reverse bias does not produce electroluminescence, but it will still have current for a low enough voltage, and therefore Joule heating.

Figure 67 a) shows an image of the sample taken during the electrical characterization performed previously to CL measurements. As we can see, the ND on top of the LED do not interfere with normal operation.

The NV0 CL signal was measured for all voltages between -20 and 9 V, although the current was capped to 100 mA to avoid burning the LED. The reason we did not measure above 9 Volts was the LED signal itself. As figure 63 shows, the InGaN peak has some broadness, and since

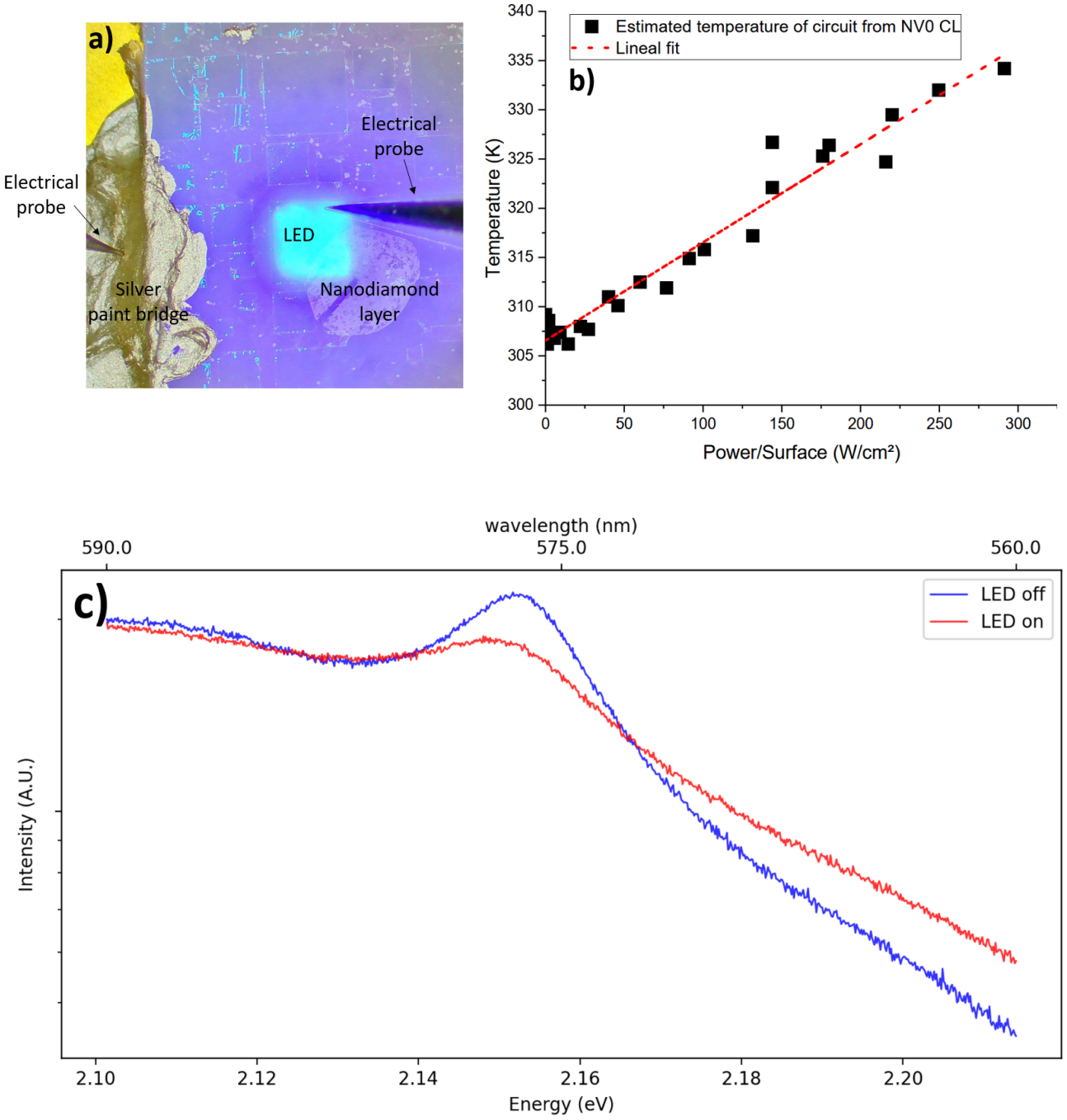


Figure 67: a) InGaN LED sample with Sigma-Aldrich ND spread on top. The LED circuit is operated by the electrical probes shown in the image. b) Estimated temperature of the LED surface vs power per surface, and expected linear model according to Joule's law of electrical heating. c) CL spectra of ND layer for the LED with no current (blue) and in a reverse bias of -16 V and a current of 100 mA (red). Intensity is in log scale, and both spectra have been rescaled for visual clarity.

the LED electroluminescence signal is much more bright than the NV0 CL signal, for a voltage above 9 Volts the upper wavelength tail end of the InGaN peak overlapped with the NV0 peak, preventing us to properly measure the CL signal. However, apart for this small issue, we did not detect any difference between forward and reverse bias, showing that the NV0 signal was unaffected by the light emitted from the LED.

Figure 67 b) shows the estimated temperature for the different values of circuit power/area. Circuit power can be obtained by multiplying current and voltage, and the surface area of the studied LED is 0.5 mm by 0.5 mm. As the figure shows, our model was able to capture the effect of Joule heating, which as expected was linear with circuit power. The error rate was reduced to 3 K, thanks to a longer exposure time of one minute per measurement.

6.5.2 Spatially resolved CL thermal sensing

The results from section 6.5.1 show that, despite the limitations imposed by the heterogeneous surface chemistry of the ND, it was possible for us to measure the effect of Joule heating in the LED using the FWHM of the NV0 CL peak. Therefore, the next logical step is to test the spatial resolution of our temperature sensing method.

The main obstacle for spatially resolved thermal sensing is the calibration step, since by the nature of the measurement multiple ND samples will be scanned, each one with a different value for the term β_0 of equation 12. However, we also know that for the case of Silicon, this surface chemistry effect homogenizes when scanning over 5 µm ×5 µm clusters, as shown in figure 61.

Unfortunately, only the InGaN LED sample enables us to achieve Joule heating, and as shown in section 6.4.6, the calibration is different for each ND cluster, as depending on their thickness, the percentage of ND in contact with the GaN surface will be different, which leads to a different value of β_0.

Despite this issue, we decided to attempt spatially resolved measurements, since as shown in figure 67, the Joule heating at high power can cause an increase in temperature of up to 30 K, which may go above the noise induced by the change in β_0.

Hence, we connected the same 0.5 mm by 0.5 mm LED to the electroluminescent probes described in section 3.6, applied a reverse bias of -15 Volts, which led to a circuit current of 2.6 mA. We then proceeded to measure the CL signal in a series of 5 by 5 µm sections on clusters at various distances from the LED, and estimate the temperature using the model for thin ND clusters of GaN shown in figure 66. A similar measurement was performed by operating the CL in spot mode, in order to study the accuracy gain by averaging over a region.

Unfortunately, the results of these measurements were quite inconclusive. Neither of the two types of measurements showed a temperature gradient, or any correlation between position and estimated temperature, as can be seen in figure 68.

There are two likely causes that contribute to this negative result:

The first cause is the thermalization of the sample being faster than our measurement time. Each of the measurements from figure 68 required the mirror to be realigned, a process that took a couple minutes per measurement, which was enough time for the sample to reach thermal stability. We calculated the stable solution for the thermal equation of a single LED active in our sample, on top of a sample holder at a stable temperature of 300 K inside a vacuum. The result was a surface with a homogeneous temperature equal to that of the LED. Hence, if the sample is given enough time between measurements to achieve thermal stability, no thermal gradient can be detected.

The second cause is the enhanced effect of ND surface chemistry heterogeneity. The surface around the LED was a non-grow p-GaN layer. As can be seen in figure 68 There are significant differences in FESEM brightness in different regions of this p-GaN compared to the LED, which highlight the lack of surface homogeneity. This can also be seen in the lower precision of single spot measurements compared to area measurements. As established by section 6.4.7, the source of increased NV0 emission heterogeneity in spot mode is the effect of the substrate on the ND surface chemistry. This causes the β_0 of equation 12 to be significantly different at each measurement.

As the surface temperature is likely homogeneous, the differences in estimated temperature for each measurement in figure 68 are likely caused by local differences in β_0 induced by the

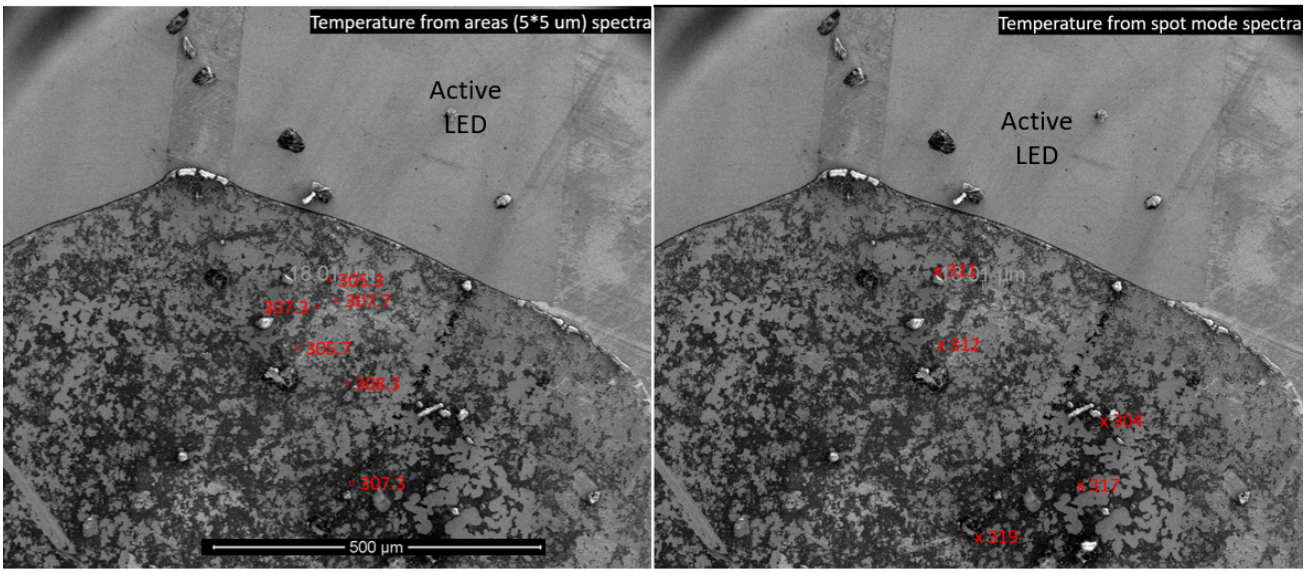


Figure 68: Temperature estimation at different points calculated by studying the CL signal from different ND according to the model for GaN shown in figure 66. The active LED was connected to a continuous circuit current of -15 Volts and -2.6 mA. Measurement was done in for both 5 µby 5 µm areas and spots, which are shown below.

heterogeneous surface chemistry.

Hence, a second measurement was performed with the same setup. The process was similar, but instead of single measurements at a large distance from the LED, we measured 40 points in a 20 µm line starting at the very edge of the LED. The custom software of the FESEM enables us to automate the process. By choosing a measurement time of 0.1 seconds per point, the entire measurements could be achieved in 4 seconds, which at the time we believed would have been a short enough time to detect a gradient. The measurements were repeated at multiple lines and for multiple circuit voltages.

An example of these measurements can be seen in figure 69. The line with more points reveals the temperature to be homogeneous along the line, the effect of the surface chemistry induced noise being much higher than any potential gradient.

Particularly cold or hot points are usually associated to specific nanodiamond structures, like the edge of a cluster of a sharp step, so these supposed temperature differences could be explained once again by differences in diamond surface chemistries. This was confirmed by repeating the measurement in the same line for a different circuit voltage, which led to the same structures

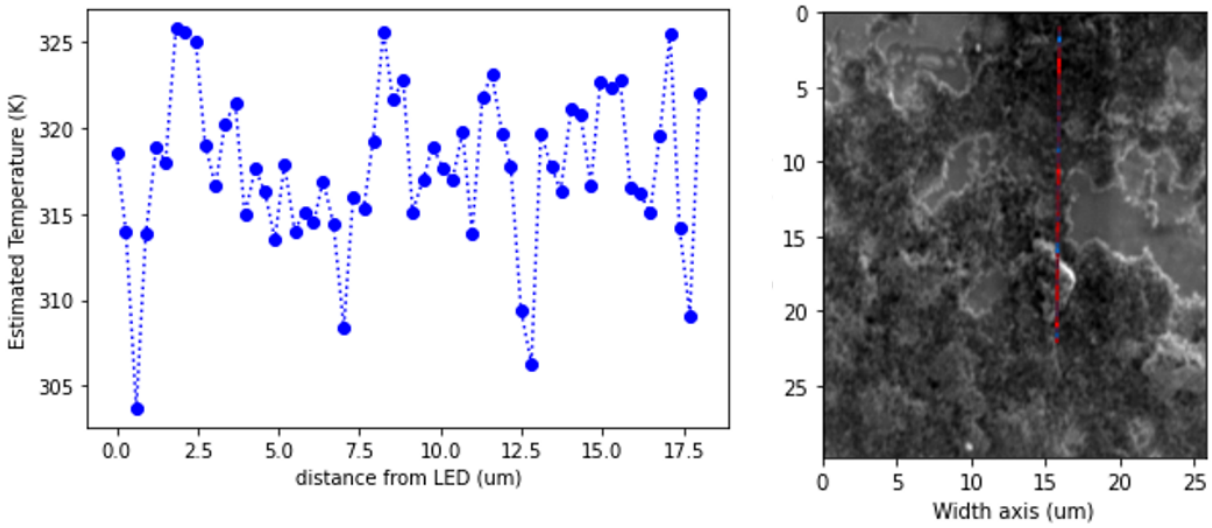


Figure 69: Temperature estimation as a function of active LED distance calculated by studying the CL signal from different points in a 20 µm line according to the model for GaN shown in figure 66.

inducing the same shift in the estimated temperature.

These results show that the chosen measurement time was not long enough to observe a temperature gradient. Hence, we performed some simulations of heat diffusion in the LED sample. The thermal conductivity of GaN is very high, 253 ± 8.8% W/mK at room temperature [136], which leads to an extremely short thermalization time. According to our simulations, the surface temperature would become fully homogeneous in a few microseconds for even the highest circuit voltages possible.

6.5.3 Time resolved CL thermal sensing

As discussed in section 6.5.2 the Joule heating of the LED sample was a very fast process, taking only a few micro seconds according to our python simulations. Hence, it could be potentially interesting to study the heating of the LED sample with ND on top using our model in a time resolved way. Strenaer *et al.* have recently developed a method to perform time-resolved Raman [137] that could be adapted to our setup.

The measurement process was as follows: The beam blanker described in section 3.4.1 was connected to a square pulse that oscillated between 5 and 0 Volts. The active time was 10 µs

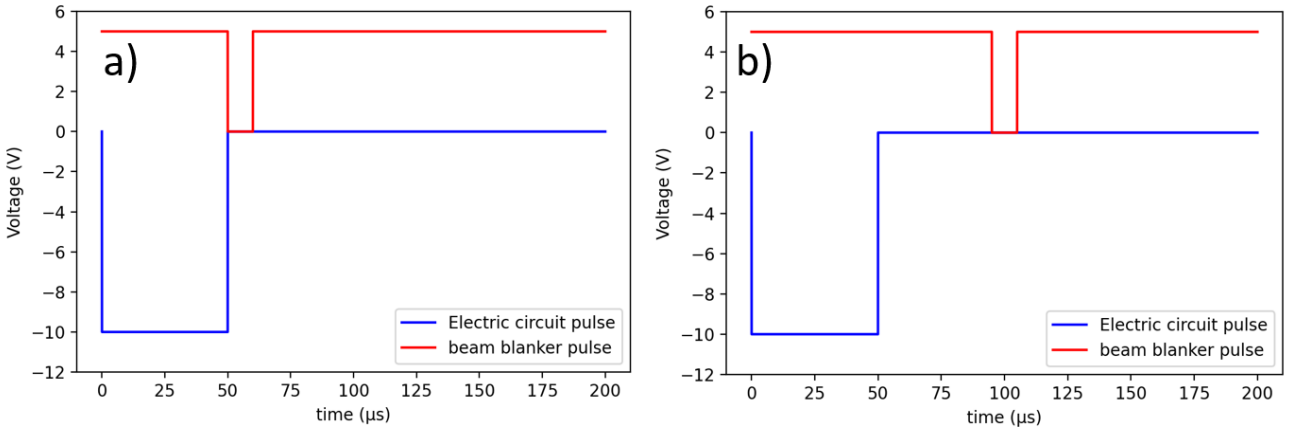


Figure 70: Example of pulses used to perform time resolved CL measurement. The blue pulse was applied to the LED circuit using the electrical probes described in section 3.6. The red pulse was applied to the beam blanker described in section 3.4.1. The delay between the two pulses was 50 µs in a) and 100 µs in b).

and the total period was 200 µs. A second square pulse of between -10 and 0 Volts, with an active time of 50 µs and total period of 200 µs was connected to the electrical probes described in section 3.6. The delay between the two pulses could be controlled by the pulse generator.

The negative voltage of the circuit pulse was used to operate the LED in reverse bias, so that we would have Joule heating but no electroluminescence, to avoid the potentially detrimental effect of the LED signal in the study of the ND CL.

By changing the delay between the pulses, we can ensure the beam blanker is only inactive during 10 µs windows that all correspond to a certain time after the activation of the LED. Figure 70 shows examples of the two pulses used for different delay values. The delay used in Figure 70 a) leads to a CL signal from just after the LED circuit has been turned off, while the delay figure 70 b) causes the CL signal to originate 50 µseconds after the LED off time.

We performed a series for all delays between 0 and 200 µs, in steps of 10 µs, which would theoretically enable us to study the effect of Joule heating and re-thermalization cooling in real time. However, as the beam blanker is active for most of the duration of the measurement, the e-h pair creation was severely limited, and therefore intensity of the sample emission was very low. This was compounded by the fact that the ND region chosen for the study was not very bright. This measurement was made roughly one year after the preparation of the sample, so

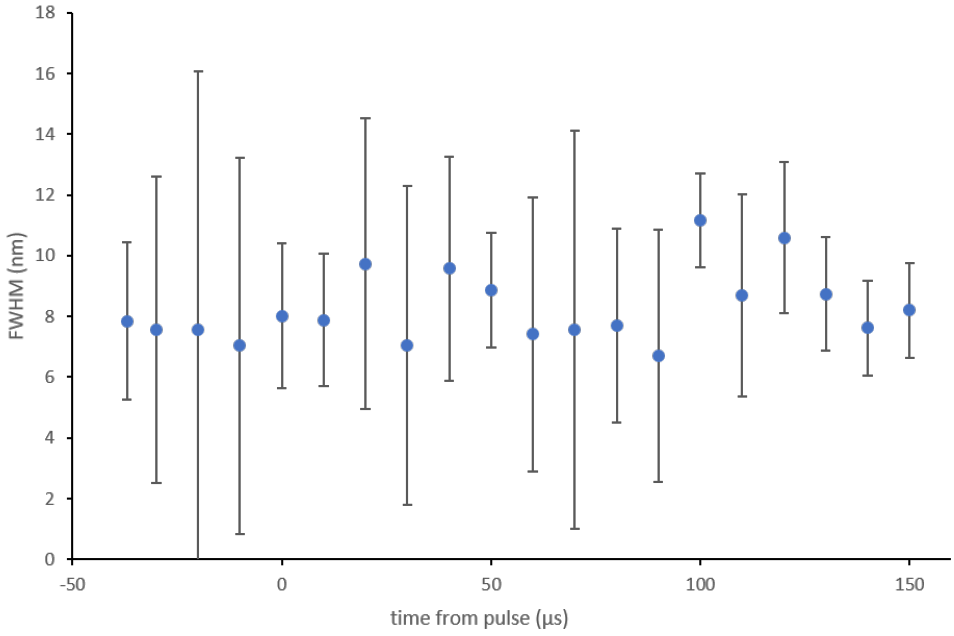


Figure 71: FWHM for time resolved CL measurements of ND on top of LED versus time since LED activation. Noise rate was too high to give a temperature estimation.

the natural oxidation had likely reduced the total emission significantly. As it will be shown in section 6.7, the properties of the samples changed over time likely due to the effect of air oxidation on the ND surface chemistry, which caused a decrease in NV0 emission intensity for these particular ND.

This low emission led to an error rate of about 20%, as can be seen in figure 71, which was too high to make any statements about the evolution of temperature. This was despite operating the electron beam at the very high current of 763 pA and using an exposure time per measurement of three minutes. Increasing the exposure time could improve accuracy, although the main limitation appears to be signal-to-noise ratio, but it would have led to another issue: There is a limit on how much heat the sample holder can absorb from the LED. Hence, as the measurements are performed, the temperature of the entire structure gradually grows as the sample holder heats up, and the LED stops thermalizing to room temperature when the circuit is off. This issue becomes worse as the measurement times are increased.

Theoretically, we could attempt to use the cryogenic stage in order to stabilize the temperature around an chosen value. However, this would mean any possible fluctuations in the helium flow would drown the effect of Joule heating, requiring us to maintain the same cooling conditions

for the entire time it takes to perform the full measurements.

Hence, for the moment we were unable to perform time-resolved thermal characterization of our sample, but we have still shown that thermally resolved CL measurements can be performed with our setup, although they require a very bright sample.

6.6 Surface UV treatment on ND

As it was discussed in section 6.4.7, the main obstacle to our thermal sensing method is the ND surface chemistry treatment. The treatment is what enables NV0 cathodoluminescence, but it also induces a fixed deviation in the FWHM that is different for each sample.

We can not simply destroy the surface chemistry treatment, since as discussed in section 6.4.7, removing it with acetone destroyed the NV0 signal. Hence, we need to instead ensure the effect of surface chemistry is more homogeneous between samples.

A potential solution comes in the form of diamond size sorting. As the results from section 6.4.4 illustrate, ND size is a big factor in the precision and accuracy of our method. And ND of similar sizes also have a similar surface to volume ratio, which should lead to a more homogeneous effect of the surface treatment.

Hugues Girard and Jean-Charles Arnault, our collaborators at Universite-Paris Saclay have developed a size sorting method [138], but were unsuccessful in applying it to our particular samples. The reason appears to be the very low -20 mV zeta potential of the ND discussed in section 6.1.2. A possible solution would be oxidizing the samples in order to raise the Zeta potential. However, full oxidation is not desirable, as it would destroy the NV0 CL emission.

Hence, we recently tested a UV treatment in order to achieve partial oxidation. The technique is based on the work of Klauser *et al.* [139]. According to their work, surface oxygen content can be raised in monocrystalline ND samples up to 10 % by an exposure of 20 minutes to a mercury UV lamp.

Mercury UV lamps emit in two wavelengths: 184.9 and 253.7 nm. The machine available at Néel emits at 365 nm, so we decided to increase the exposure time to ensure maximal oxidation. We prepared a new ND spread on top of a silicon substrate, and we exposed it to the 365 nm UV treatment for 25 minutes. We then characterized the NV0 signal at multiple temperatures. despite a loss of about 33% of intensity, no change in the FWHM behavior with temperature was detected. Hence, this treatment may be able to raise the zeta potential enough to enable size sorting without destroying NV0 emission.

6.7 Lifetime measurements of different surface chemistries

One of the last experiments we performed during the development of this PhD was the measurement and comparison of the lifetime at room temperature of the NV0 peak of all three surface treatments we tested. Full oxidation with acetone, partial oxidation with ultraviolet (UV), and untreated samples. The goal of these measurements was to understand the mechanism that enables the interaction between surface chemistry and NV0 emission.

The measurements were performed using the setup described in section 3.5. In fact, figure 11 a) is one of the lifetime decays obtained during this measurement. We scanned all three samples at different regions to examine the effect of the surface treatment on the lifetime, as different areas would have different surface properties. However, apart from the lower intensity of the isolated samples leading to a higher error rate, we did not detect a meaningful difference in the lifetimes of the different structures. The pulse period was 1 µs, and measurements were done for active percentage duty times of 50% and 80%.

The average lifetime was 18 ± 1.7 ns for the untreated sample, 29 ± 2 ns for the UV treated sample, and 26 ± 5 ns for the acetone treatment. The full results are shown in table 1. As both the acetone and UV treatments lead to a lower intensity and a longer lifetime, it appears that their effect on NV0 involves enhancing the half-life of the excited state. The acetone treatment also appears to be less homogeneous than the UV treatment, as seen from the larger variation in lifetime.

Another interesting observation is the high luminosity of the acetone samples, being at times

greater than the untreated sample. This is contradictory with the previous result show in section 6.4.7. The most likely explanation for the discrepancy is the time interval between the two measurements. Measurements on the acetone sample in section 6.4.7 were performed the day after treatment, while the measurements of this section were performed more than a year after said treatment took place. Hence, the chemical properties of the ND surface have likely changed as a result of exposure to air, and subsequent surface oxidation.

The effect of this oxidation seems to push the NV0 emission of the different ND towards a particular intensity. In the case of the untreated sample, the intensity went down by a factor of about 5, while the acetone treated sample increased its own emission by two orders of magnitude since the treatment took place, making the two intensities close in value, a far cry from the result shown in Figure 65. The UV sample was a new spread, and had an intensity about 3 times lower compared to before the treatment. The fact that the UV treated sample has a similar intensity to that of the other two types of ND after a year of air exposure supports the hypothesis that the effect of air exposure is surface oxidation. This makes particularly interesting that the lifetime of the samples remained very different, despite emission intensity becoming similar.

These results show that the relationship between the NV0 properties and the surface treatment is complex, and further studies in more homogeneous samples will be required to properly understand and utilize this relation.

Treatment	Counts per second (50%)	ND type	Lifetime 50%
None	17.1	Thick cluster	16.84±0.02
None	38.0	Thick cluster	22.3±0.4
None	15.7	Thick cluster	16.9±0.7
None	10.2	Thin cluster	18.7±0.6
None	2.8	Cluster edge	18.3±0.6
None	18.3	Cluster	18.8±0.14
None	16.9	Cluster	16.73±0.01
None	14.8	Cluster	16.8±0.4
None	10.4	Cluster	18.40±0.07
UV	35.0	Thin cluster	28.6±0.4
UV	17.0	Cluster edge	29.2±0.1
UV	60.2	Single ND on Si	30.0±0.1
UV	21.74	Cluster	28.62±0.02
UV	47.0	Thick cluster	29.7±0.4
UV	32.0	Cluster	29.5±0.1
UV	27.6	Single ND on cluster	25.4±0.3
UV	50.8	Large ND	29.17±0.03
UV	39.3	Single ND on cluster	30.1±0.4
UV	61.2	Single ND on Si	32.0±0.2
UV	48.8	Cluster	31.3 ±0.2
UV	44.1	Cluster	31.0 ±0.2
UV	8.7	Single ND on Si	31.68 ±0.03
UV	4.5	Single ND on Si	25.22±0.07
Acetone	57.1	Cluster	19.95±0.01
Acetone	5.4	Single ND on Si	36.5±0.7
Acetone	54.4	Single ND on Si	27.1±0.2
Acetone	6.8	Single ND on Si	29.2±0.2
Acetone	20.2	Cluster	22.5±0.7
Acetone	12.1	Single ND on Si	34.1 ±0.8
Acetone	36.3	Cluster	22.38±0.03
Acetone	36.9	Cluster	24.5±0.1
Acetone	33.2	Cluster	23.1 ±0.1
Acetone	5.2	Single ND on Si	26.4 ±0.4

Table 1: Number of counts, estimated lifetime and ND structure type for all lifetime measurements.

6.8 Conclusion

Although they are the same material, the results on ND have been significantly different that those in bulk diamond. However, despite this limitation, we were able to carry the methodology developed for the study of the NV0 defect in bulk to the nano samples, albeit with some changes. The high brightness of the samples is a good sign for thermal resolution, and the FWHM of the defect was even more sensitive to temperature that in bulk.

But despise those positives, the ND also presented us with new challenges. As the study of the spectra revealed, the phonon-assisted exciton peaks are not present in these samples, which removes the potential of this method for low temperature sensing. Despite not being our main goal, this is undeniably a setback.

Most notably, the strong variation in the NV0 signal between individual samples, particularly very small ones, represents a much more worrying implication for our goals, as spatial resolution in our proposed method is mainly limited by ND size. After studying this heterogeneity in detail, we are confident in attributing it to variations in ND surface chemistry. In this chapter, we have shown the results that lead us to this conclusion, including a global shift in FWHM when ND are in contact with a GaN surface.

The NV0 heterogeneity forces us to average the CL signal of multiple samples for the moment, which severely limits spatial resolution. But despite this setback, thermal sensing on an active LED circuit has been achieved with a thermal resolution of 3 K. And by finding the source of the heterogeneity, we have enabled future research aimed at mitigating it.

7 Conclusions and perspectives

As discussed in the introduction chapter, the original goal of this PhD was to develop a technique for the simultaneous characterization of carrier dynamics and sample temperature sensing of electronic devices with a very high spatial resolution.

We quickly settled for CL as the backbone of this technique due to the high spatial resolution it can provide, which despite being sample dependent, can be in the range of tens of nanometers as discussed in chapter 3. CL also has the advantage of being a well established technique, which makes further applications our method easier to implement and develop, as they are build on top of existing equipment and procedures.

The exploration of CL as a carrier characterization technique was the focus of chapter 4. In said chapter, we performed spatially and time-resolved CL measurements on a series of µLED samples, which allowed us to sense heterogeneous behavior between samples and determine its origin to be structural defects known as V-pits. V-pits had a lateral size of only 200 nm, so fact that we were able to detect this structures using only CL shows the high resolution power that this techniques enables.

Apart from detecting the presence and effect of these V-pit defects, chapter 4 also discussed some other carrier behaviors and properties inside the µLED samples. For example, surface recombination, was detected and analyzed via time-resolved CL measurements, as the new paths created by the surface reduced carrier lifetime, illustrating the power of this technique.

Once the first goal of our novel methodology was achieved, we switched focus towards thermal sensing using the CL signal of diamond. Hence, we studied the thermal evolution of the diamond CL spectrum, beginning with bulk samples in chapter 5, and then progressing to nanodiamond samples in chapter 6.

The results on bulk diamond are discussed in chapter 5. By carefully analyzing the CL spectrum of this material for a wide range of temperatures, we found two sections of this spectrum that seem to adjust to our requirements: The first are the phonon-assisted exciton peaks, which provide excellent temperature resolution at low temperature, owing to the known

thermal dependence of the exciton energy. The second is the peak associated to the neutral nitrogen vacancy center or NV0. Said peak can be modeled with a Voigt profile, and its full width at half maximum was shown to be a good temperature sensor above 150 Kelvin.

With those good results on bulk diamond, we moved on to nanodiamond samples in chapter 6. Our thermal sensor method will be limited by the size of the diamond used, so even though starting from bulk samples made sense from an experimental perspective, the results on nanodiamond will be the determining factor for the effectiveness of our method.

The first results discussed in the last chapter were mixed: On the one hand, the phonon-assisted exciton peaks were not present in the new measurements, meaning that our low-temperature probe has been lost. On the other hand, the peak associated to the NV0 peak behaves similarly to the bulk case, except for a much larger intensity and stronger thermal dependence. These results mean that accuracy at room temperature will be better than in bulk, but we will not be able to measure low temperature changes. As our interest lay in room temperature electronic devices, this is overall good news.

However, further studies on the nanodiamonds revealed some issues with our method. Most notably, both the nanodiamond size and the material they were deposited on had an impact on the NV0 emission properties, distorting the expected value of the peak full width at half maximum. We have found compelling evidence that both of these effects are caused by modifications of the nanodiamond surface chemistry between different samples. Despite this issue, we were able to mitigate the heterogeneity of individual samples by averaging signal over a region, and we could compensate for the effect of the deposition surface with a calibration step.

Although we have not fully develop our technique to achieve the desired high spatial resolution due to the need to average the signal of multiple samples, we were able to demonstrate thermal sensing of Joule heating in a LED sample. Hence, in this work we have not only demonstrated the potential CL has in providing high spatial and even temporal resolution, but we have also laid down a potential path to overcome the effects of surface chemistry, in the form of size sorting and chemical treatments. We have even tested some treatments ourselves, obtaining results that despite being very preliminary, give room for optimism.

Hence, the next avenues for research in NV0 CL thermometry will likely involve the synthesis of new size-controlled samples and the testing of a large variety of surface chemistries, in order to mitigate the effect of ND surface properties on the NV0 CL emission. This will ensure that NV0 CL properties are only dependent on ND temperature, and therefore will remove the need for averaging and grant access to the high spatial resolution CL can provide. Different surface chemistries may also help with the long term stability of the ND emission, which despite not being a top priority, is nonetheless a field with room for improvement.

At the moment, we believe in the potential of nanodiamond CL as a powerful tool for high spatial resolution thermal characterization, and we hope that with this work, we can help in the realization of this potential.

References

1. Sáenz de Santa María Modroño, P., Le Maoult, C., Bernier, N., Vaufrey, D. & Jacopin, G. Investigation of Emission Heterogeneity in InGaN/GaN Micro-Light-Emitting Diodes by Photon-Correlation Cathodoluminescence Spectroscopy. *ACS Photonics* **11,** 2406–2412. eprint: https://doi.org/10.1021/acsphotonics.4c00300. https://doi.org/10.1021/acsphotonics.4c00300 (2024).

2. Sáenz de Santa María Modroño, P., Girard, H., Arnault, J.-C. & Jacopin, G. High-Resolution Thermal Sensing Using Temperature-Sensitive Cathodoluminescence Spectroscopy in Nitrogen-Doped Nanodiamonds. *physica status solidi (a)* **222** (Oct. 2024).

3. Bloch, F. Über die quantenmechanik der elektronen in kristallgittern. *Zeitschrift für physik* **52,** 555–600 (1929).

4. Thompson, D. The reciprocal lattice as the Fourier transform of the direct lattice. *American Journal of Physics* **64,** 333–334. ISSN: 0002-9505 (Mar. 1996).

5. Werpachowska, A. *Spin waves and the anomalous Hall effect in ferromagnetic (Ga,Mn)As* PhD thesis (Jan. 1, 2011).

6. Carrier, P., Rohra, S. & Goerling, A. General treatment of the singularities in Hartree-Fock and exact-exchange Kohn-Sham methods for solids. *Physical Review B* **75** (Mar. 23, 2006).

7. Fritsch, D., Schmidt, H. & Grundmann, M. Band dispersion relations of zinc-blende and wurtzite InN. *Phys. Rev. B* **69,** 165204. https://link.aps.org/doi/10.1103/PhysRevB.69.165204 (16 Apr. 2004).

8. Sudarsan, V. in *Materials Under Extreme Conditions* (eds Tyagi, A. & Banerjee, S.) 129–158 (Elsevier, Amsterdam, 2017). ISBN: 978-0-12-801300-7. https://www.sciencedirect.com/science/article/pii/B9780128013007000048.

9. Zhang, S. *et al.* Efficient emission of InGaN-based light-emitting diodes: toward orange and red. *Photon. Res.* **8,** 1671–1675. https://opg.optica.org/prj/abstract.cfm?URI=prj-8-11-1671 (Nov. 2020).

10. Rossi, F. *et al.* Influence of short-term low current dc aging on the electrical and optical properties of InGaN blue light-emitting diodes. *Journal of Applied Physics* **99,** 053104. ISSN: 0021-8979. eprint: https://pubs.aip.org/aip/jap/article-pdf/doi/10.1063/1.2178856/14743305/053104_1_online.pdf. https://doi.org/10.1063/1.2178856 (Mar. 2006).

11. Kim, K. S. *et al.* Investigation of dominant effect on efficiency droop in InGaN light emitting device. *Applied Physics Letters* **97,** 031113. ISSN: 0003-6951. eprint: https://pubs.aip.org/aip/apl/article-pdf/doi/10.1063/1.3467451/14433803/031113_1_online.pdf. https://doi.org/10.1063/1.3467451 (July 2010).

12. Iveland, J., Martinelli, L., Peretti, J., Speck, J. S. & Weisbuch, C. Direct Measurement of Auger Electrons Emitted from a Semiconductor Light-Emitting Diode under Electrical Injection: Identification of the Dominant Mechanism for Efficiency Droop. *Phys. Rev. Lett.* **110,** 177406. https://link.aps.org/doi/10.1103/PhysRevLett.110.177406 (17 Apr. 2013).

13. Hajdel, M. *et al.* Dependence of InGaN Quantum Well Thickness on the Nature of Optical Transitions in LEDs. *Materials* **15.** ISSN: 1996-1944. https://www.mdpi.com/1996-1944/15/1/237 (2022).

14. Viswan, V. A review of silicon carbide and gallium nitride power semiconductor devices. *IJRESM* **1,** 224–225 (2018).

15. Park, J., Baek, W., Geum, D.-M. & Kim, S. Understanding the Sidewall Passivation Effects in AlGaInP/GaInP Micro-LED. *Nanoscale Research Letters* **17,** 29. ISSN: 1556-276X. https://doi.org/10.1186/s11671-022-03669-5 (Mar. 2022).

16. Wong, M. S. *et al.* Size-independent peak efficiency of III-nitride micro-light-emitting-diodes using chemical treatment and sidewall passivation. *Applied Physics Express* **12,** 097004. https://dx.doi.org/10.7567/1882-0786/ab3949 (Aug. 2019).

17. Baek, W. J. *et al.* Ultra-low-current driven InGaN blue micro light-emitting diodes for electrically efficient and self-heating relaxed microdisplay. *Nature Communications* **14,** 1386. ISSN: 2041-1723. https://doi.org/10.1038/s41467-023-36773-w (Mar. 2023).

18. Pavlidis, G., Hilton, A. M., Brown, J. L., Heller, E. R. & Graham, S. Monitoring the Joule heating profile of GaN/SiC high electron mobility transistors via cross-sectional thermal imaging. *Journal of Applied Physics* **128,** 075705. ISSN: 0021-8979. eprint: https:

//pubs.aip.org/aip/jap/article-pdf/doi/10.1063/5.0014407/13258035/075705_1_online.pdf. https://doi.org/10.1063/5.0014407 (Aug. 2020).

19. Latorre-Rey, A. D., Merrill, K., Albrecht, J. D. & Saraniti, M. Assessment of Self-Heating Effects Under Lateral Scaling of GaN HEMTs. *IEEE Transactions on Electron Devices* **66,** 908–916 (2019).

20. Ferry, D. K. *Semiconductors* ISBN: 978-0-750-31044-4. https://dx.doi.org/10.1088/978-0-750-31044-4 (IOP Publishing, 2013).

21. Altuntas, P. *et al.* Power Performance at 40 GHz of AlGaN/GaN High-Electron Mobility Transistors Grown by Molecular Beam Epitaxy on Si(111) Substrate. *IEEE Electron Device Letters* **36,** 303–305 (2015).

22. Chen, K. J. *et al.* GaN-on-Si Power Technology: Devices and Applications. *IEEE Transactions on Electron Devices* **64,** 779–795 (2017).

23. *Thermodynamics in the Quantum Regime: Fundamental Aspects and New Directions* (eds Binder, F., Correa, L. A., Gogolin, C., Anders, J. & Adesso, G.) ISBN: 978-3-319-99045-3 (Springer, 2018).

24. Teixidó-Bonfill, A., Ortega, A. & Martín-Martínez, E. First law of quantum field thermodynamics. *Physical Review A* **102** (Nov. 2020).

25. Jain, A. *et al.* Commentary: The Materials Project: A materials genome approach to accelerating materials innovation. *APL Materials* **1,** 011002. ISSN: 2166-532X. eprint: https://pubs.aip.org/aip/apm/article-pdf/doi/10.1063/1.4812323/13163869/011002_1_online.pdf. https://doi.org/10.1063/1.4812323 (July 2013).

26. Bar-Cohen, A. & Wang, P. On-chip Hot Spot Remediation with Miniaturized Thermoelectric Coolers. *Microgravity Science and Technology* **21,** 351–359. ISSN: 1875-0494. https://doi.org/10.1007/s12217-009-9162-4 (Aug. 2009).

27. Zhao, G. *et al.* Thermo-optical nonlinearity of GaN grown by metalorganic chemical- vapor deposition. *Applied Physics Letters* **73,** 22–24 (July 1998).

28. Muth, J. *et al.* Absorption coefficient, energy gap, exciton binding energy, and recombination lifetime of GaN obtained from transmission measurements. *Applied Physics Letters* **71,** 2572– (Nov. 1997).

29. Titkov, I. *et al.* Temperature-Dependent Internal Quantum Efficiency of Blue High-Brightness Light-Emitting Diodes. *IEEE Journal of Quantum Electronics* **50,** 911–920 (Sept. 2014).

30. Lee, M.-W., Twu, H., Chen, C.-C. & Chen, C.-H. Optical characterization of wurtzite gallium nitride nanowires. *Applied Physics Letters* **79,** 3693–3695 (Nov. 2001).

31. Bradac, C., Lim, S. F., Chang, H.-C. & Aharonovich, I. Optical Nanoscale Thermometry: From Fundamental Mechanisms to Emerging Practical Applications. *Advanced Optical Materials* **8,** 2000183. eprint: https://onlinelibrary.wiley.com/doi/pdf/10.1002/adom.202000183. https://onlinelibrary.wiley.com/doi/abs/10.1002/adom.202000183 (2020).

32. Okabe, K. *et al.* Intracellular temperature mapping with a fluorescent polymeric thermometer and fluorescence lifetime imaging microscopy. *Nature Communications* **3,** 705. ISSN: 2041-1723. https://doi.org/10.1038/ncomms1714 (Feb. 2012).

33. Jaque, D. & Vetrone, F. Luminescence nanothermometry. *Nanoscale* **4,** 4301–4326. http://dx.doi.org/10.1039/C2NR30764B (15 2012).

34. V.Barbosa, I., Maia, L. J., Ibanez, A. & Dantelle, G. Recent developments on BW-II and BW-III ratiometric luminescent nanothermometers for in vivo thermal sensing. *Optical Materials: X* **18,** 100236. ISSN: 2590-1478. https://www.sciencedirect.com/science/article/pii/S2590147823000104 (2023).

35. Wang, C.-C., Lin, J.-Y. & Lee, C.-H. Membrane ripples of a living cell measured by non-interferometric widefield optical profilometry. *Opt. Express* **13,** 10665–10672. https://opg.optica.org/oe/abstract.cfm?URI=oe-13-26-10665 (Dec. 2005).

36. Hell, S. W., Schmidt, R. & Egner, A. Diffraction-unlimited three-dimensional optical nanoscopy with opposing lenses. *Nature Photonics* **3,** 381–387. ISSN: 1749-4893. https://doi.org/10.1038/nphoton.2009.112 (July 2009).

37. Neumann, P. *et al.* High-Precision Nanoscale Temperature Sensing Using Single Defects in Diamond. *Nano Letters* **13,** 2738–2742. ISSN: 1530-6984. https://doi.org/10.1021/nl401216y (June 2013).

38. Zhang, Y. *et al.* A Review on Principles and Applications of Scanning Thermal Microscopy (SThM). *Advanced Functional Materials* **30,** 1900892. eprint: https://onlinelibrary.wiley.com/doi/pdf/10.1002/adfm.201900892. https://onlinelibrary.wiley.com/doi/abs/10.1002/adfm.201900892 (2020).

39. Aigouy, L., Lalouat, L., Mortier, M., Löw, P. & Bergaud, C. Note: A scanning thermal probe microscope that operates in liquids. *The Review of scientific instruments* **82,** 036106 (Mar. 2011).

40. Luo, T. & Chen, G. Nanoscale heat transfer – from computation to experiment. *Phys. Chem. Chem. Phys.* **15,** 3389–3412. http://dx.doi.org/10.1039/C2CP43771F (10 2013).

41. Tovee, P. *et al.* Ultra High Thermal Resolution Scanning Probe Microscopy via Carbon Nanotube Tipped Thermal Probes (May 2013).

42. Takada, K., Katsumi, R. & Yatsui, T. Sensitivity improvement of a single-NV diamond magnetometer using a chiral waveguide. *Opt. Express* **32,** 795–802. https://opg.optica.org/oe/abstract.cfm?URI=oe-32-1-795 (Jan. 2024).

43. Solà-Garcia, M. *et al.* Photon Statistics of Incoherent Cathodoluminescence with Continuous and Pulsed Electron Beams. *ACS Photonics* **8.** PMID: 33763505, 916–925. eprint: https://doi.org/10.1021/acsphotonics.0c01939. https://doi.org/10.1021/acsphotonics.0c01939 (2021).

44. Yu, Y.-H. *et al.* Optically detected magnetic resonance of nitrogen-vacancy centers in diamond under weak laser excitation. *Phys. Rev. Appl.* **21,** 044051. https://link.aps.org/doi/10.1103/PhysRevApplied.21.044051 (4 Apr. 2024).

45. Liu, G.-Q., Liu, R.-B. & Li, Q. Nanothermometry with Enhanced Sensitivity and Enlarged Working Range Using Diamond Sensors. *Accounts of Chemical Research* **56.** PMID: 36594628, 95–105. eprint: https://doi.org/10.1021/acs.accounts.2c00576. https://doi.org/10.1021/acs.accounts.2c00576 (2023).

46. Stehlik, S. *et al.* Size and Purity Control of HPHT Nanodiamonds down to 1 nm. *The Journal of Physical Chemistry C* **119,** 27708–27720. ISSN: 1932-7447. https://doi.org/10.1021/acs.jpcc.5b05259 (Dec. 2015).

47. Chauhan, A. *Deformation and damage mechanisms of ODS steels under high-temperature cyclic loading* PhD thesis (Feb. 2018).

48. Drouin, D. *et al.* CASINO V2.42—A Fast and Easy-to-use Modeling Tool for Scanning Electron Microscopy and Microanalysis Users. *Scanning* **29,** 92–101. eprint: https://onlinelibrary.wiley.com/doi/pdf/10.1002/sca.20000. https://onlinelibrary.wiley.com/doi/abs/10.1002/sca.20000 (2007).

49. Hon., A. The Relation of Aperture and Power in the Microscope (continued). *Journal of the Royal Microscopical Society* **2,** 460–473. eprint: https://onlinelibrary.wiley.com/doi/pdf/10.1111/j.1365-2818.1882.tb04805.x. https://onlinelibrary.wiley.com/doi/abs/10.1111/j.1365-2818.1882.tb04805.x (1882).

50. Morimoto, H., Hazama, Y., Tanaka, K. & Naka, N. Exciton lifetime and diffusion length in high-purity chemical-vapor-deposition diamond. *Diamond and Related Materials* **63.** 9th International Conference on New Diamond and Nano Carbons – NDNC 2015, 47–50. ISSN: 0925-9635. https://www.sciencedirect.com/science/article/pii/S0925963515300893 (2016).

51. *Scientific Cameras, Microscopy Systems & Spectrographs - Andor* Oxford Instruments. https://andor.oxinst.com/ (2022).

52. De la Peña, F. *et al. hyperspy/hyperspy: v2.3.0* version v2.3.0. Mar. 2025. https://doi.org/10.5281/zenodo.14956374.

53. *Fluorolog-QM with FelixFL* HORIBA Scientific. https://www.horiba.com/int/scientific/products/detail/action/show/Product/fluorolog-qm-1997/ (2024).

54. Chesi, G., Allevi, A. & Bondani, M. *Quantum Measurements and Quantum Metrology* **6,** 1–6. https://doi.org/10.1515/qmetro-2019-0001 (2019).

55. Meuret, S. *Expérience de Hanbury Brown et Twiss dans un microscope électronique à transmission à balayage : sa physique et ses applications* Theses (Université Paris Saclay (COmUE), Nov. 2015). https://theses.hal.science/tel-01281402.

56. Meuret, S. *et al.* Photon Bunching in Cathodoluminescence. *Phys. Rev. Lett.* **114,** 197401. https://link.aps.org/doi/10.1103/PhysRevLett.114.197401 (19 May 2015).

57. Yuge, T., Yamamoto, N., Sannomiya, T. & Akiba, K. Superbunching in cathodoluminescence: A master equation approach. *Phys. Rev. B* **107,** 165303. https://link.aps.org/doi/10.1103/PhysRevB.107.165303 (16 Apr. 2023).

58. Donatini, F. & Pernot, J. Exciton diffusion coefficient measurement in ZnO nanowires under electron beam irradiation. *Nanotechnology* **29,** 105703. https://dx.doi.org/10.1088/1361-6528/aaa638 (Jan. 2018).

59. Matioli, E. & Weisbuch, C. Impact of photonic crystals on LED light extraction efficiency: approaches and limits to vertical structure designs. *Journal of Physics D: Applied Physics* **43,** 354005. https://dx.doi.org/10.1088/0022-3727/43/35/354005 (Aug. 2010).

60. Le Maoult, C. *tude et optimisation de l ' étape de passivation des µLED bleues GaN-InGaN* PhD thesis (Université Grenoble Alpes, 2021). https://www.theses.fr/2021GRALT073.

61. Haller, C. *et al.* Burying non-radiative defects in InGaN underlayer to increase InGaN/GaN quantum well efficiency. *Applied Physics Letters* **111,** 262101. ISSN: 0003-6951. eprint: https://pubs.aip.org/aip/apl/article-pdf/doi/10.1063/1.5007616/19782390/262101_1_online.pdf. https://doi.org/10.1063/1.5007616 (Dec. 2017).

62. Lopez, M. *et al. Simulation of random alloy effects in InGaN/GaN LEDs* in (Aug. 2013), 113–114. ISBN: 978-1-4673-6309-9.

63. Finot, S. *Cathodoluminescence lifetime spectroscopy for efficient III-nitride LEDs* PhD thesis (Université Grenoble Alpes, 2022). https://www.theses.fr/2022GRALY064.

64. Finot, S., Le Maoult, C., Gheeraert, E., Vaufrey, D. & Jacopin, G. Surface Recombinations in III-Nitride Micro-LEDs Probed by Photon-Correlation Cathodoluminescence. *ACS Photonics* **9,** 173–178. eprint: https://doi.org/10.1021/acsphotonics.1c01339. https://doi.org/10.1021/acsphotonics.1c01339 (2022).

65. Olivier, F., Daami, A., Licitra, C. & Templier, F. Shockley-Read-Hall and Auger non-radiative recombination in GaN based LEDs: A size effect study. *Applied Physics Letters* **111,** 022104 (July 2017).

66. Xie, E. *et al.* Strain relaxation in InGaN/GaN micro-pillars evidenced by high resolution cathodoluminescence hyperspectral imaging. English. *Journal of Applied Physics* **112.** ISSN: 0021-8979 (July 2012).

67. Zhang, C. *et al.* Strain Relaxation Effect on the Peak Wavelength of Blue InGaN/GaN Multi-Quantum Well Micro-LEDs. *Applied Sciences* **12.** ISSN: 2076-3417. https://www.mdpi.com/2076-3417/12/15/7431 (2022).

68. Choi, H. W. *et al.* Mechanism of enhanced light output efficiency in InGaN-based microlight emitting diodes. *Journal of Applied Physics* **93,** 5978–5982. ISSN: 0021-8979. eprint: https://pubs.aip.org/aip/jap/article-pdf/93/10/5978/12243945/5978_1_online.pdf. https://doi.org/10.1063/1.1567803 (May 2003).

69. Cao, X. A., LeBoeuf, S. F., Rowland, L. B., Yan, C. H. & Liu, H. Temperature-dependent emission intensity and energy shift in InGaN/GaN multiple-quantum-well light-emitting diodes. *Applied Physics Letters* **82,** 3614–3616. ISSN: 0003-6951. eprint: https://pubs.aip.org/aip/apl/article-pdf/82/21/3614/18578612/3614_1_online.pdf. https://doi.org/10.1063/1.1578539 (May 2003).

70. González-Izquierdo, P. *et al.* Influence of Shape and Size on GaN/InGaN µLED Light Emission: A Competition between Sidewall Defects and Light Extraction Efficiency. *ACS Photonics* **10,** 4031–4037. eprint: https://doi.org/10.1021/acsphotonics.3c00971. https://doi.org/10.1021/acsphotonics.3c00971 (2023).

71. Dhar, S. & Ghosh, S. Low field electron mobility in GaN. *Journal of Applied Physics* **86,** 2668–2676. ISSN: 0021-8979. eprint: https://pubs.aip.org/aip/jap/article-pdf/86/5/2668/19204985/2668_1_online.pdf. https://doi.org/10.1063/1.371108 (Sept. 1999).

72. Moreno, I. & Sun, C.-C. Modeling the radiation pattern of LEDs. *Opt. Express* **16,** 1808–1819. https://opg.optica.org/oe/abstract.cfm?URI=oe-16-3-1808 (Feb. 2008).

73. David, A. Long-Range Carrier Diffusion in (In, Ga)N Quantum Wells and Implications from Fundamentals to Devices. *Phys. Rev. Appl.* **15,** 054015. https://link.aps.org/doi/10.1103/PhysRevApplied.15.054015 (5 May 2021).

74. Liu, W., Carlin, J.-F., Grandjean, N., Deveaud, B. & Jacopin, G. Exciton dynamics at a single dislocation in GaN probed by picosecond time-resolved cathodoluminescence. *Applied Physics Letters* **109,** 042101. ISSN: 0003-6951. eprint: https://pubs.aip.org/aip/apl/article-pdf/doi/10.1063/1.4959832/14483112/042101_1_online.pdf. https://doi.org/10.1063/1.4959832 (July 2016).

75. Hangleiter, A. *et al.* Suppression of Nonradiative Recombination by V-Shaped Pits in GaInN/GaN Quantum Wells Produces a Large Increase in the Light Emission Efficiency. *Phys. Rev. Lett.* **95,** 127402. https://link.aps.org/doi/10.1103/PhysRevLett.95.127402 (12 Sept. 2005).

76. Chen, S.-W., Li, H., Chang, C.-J. & Lu, T.-C. Effects of Nanoscale V-Shaped Pits on GaN-Based Light Emitting Diodes. *Materials* **10,** 113. ISSN: 1996-1944. https://www.mdpi.com/1996-1944/10/2/113 (2017).

77. Song, T. L. Strain relaxation due to V-pit formation in InxGa1-xN GaN epilayers grown on sapphire. *Journal of Applied Physics* **98,** 084906. ISSN: 0021-8979. eprint: https://pubs.aip.org/aip/jap/article-pdf/doi/10.1063/1.2108148/13408390/084906_1_online.pdf. https://doi.org/10.1063/1.2108148 (Oct. 2005).

78. Ajia, I. A. *et al.* Generated Carrier Dynamics in V-Pit-Enhanced InGaN/GaN Light-Emitting Diode. *ACS Photonics* **5,** 820–826. https://doi.org/10.1021/acsphotonics.7b00944 (Mar. 2018).

79. Wang, H., Wang, X., Tan, Q. & Zeng, X. V-defects formation and optical properties of InGaN/GaN multiple quantum well LED grown on patterned sapphire substrate. *Materials Science in Semiconductor Processing* **29.** Special Topical Issue on Wide-Bandgap Semiconductor Materials, 112–116. ISSN: 1369-8001. https://www.sciencedirect.com/science/article/pii/S1369800113003545 (2015).

80. Alreshidi, F. *et al.* Enhanced Efficiency InGaN/GaN Multiple Quantum Well Structures via Strain Engineering and Ultrathin Subwells Formed by V-Pit Sidewalls. *ACS Applied Optical Materials* **2,** 220–229. https://doi.org/10.1021/acsaom.3c00406 (Jan. 2024).

81. Zhu, T., Cheng, L. & Zeng, X. Effect of V-pits size on the reliability of InGaN/GaN light emitting diodes. *Superlattices and Microstructures* **157,** 106990. ISSN: 0749-6036. https://www.sciencedirect.com/science/article/pii/S0749603621001889 (2021).

82. Ho, C.-H., Speck, J. S., Weisbuch, C. & Wu, Y.-R. Efficiency and Forward Voltage of Blue and Green Lateral LEDs with V-shaped Defects and Random Alloy Fluctuation in Quantum Wells. *Phys. Rev. Appl.* **17,** 014033. https://link.aps.org/doi/10.1103/PhysRevApplied.17.014033 (1 2022).

83. Konishi, K. & Naka, N. Phonon-assisted excitonic absorption in diamond. *Phys. Rev. B* **104,** 125204. https://link.aps.org/doi/10.1103/PhysRevB.104.125204 (12 Sept. 2021).

84. *DiamFab : la technologie diamant au service de la haute puissance* DIAMFAB la Technologie Diamant. https://diamfab.com/.

85. Barjon, J. *et al.* Silicon incorporation in CVD diamond layers. *physica status solidi (a)* **202,** 2177–2181. ISSN: 1862-6319 (2005).

86. Zaitsev, A. M. *Optical Properties of Diamond* ISBN: 978-3-662-04548-0 (Springer Berlin Heidelberg, Berlin, Heidelberg, 2001).

87. Eaton-Magaña, S. & Shigley, J. E. *Observations on CVD-Grown Synthetic Diamonds: A Review — Gems & Gemology* http://www.gia.edu/sites/Satellite?c=Page&cid=1495238004024&childpagename=GIA/Page/GGArticleDetail&pagename=GIA/Wrapper&WRAPPERPAGE=GIA/Wrapper.

88. Gucsik, A. *et al.* Cathodoluminescence Microscopy and Spectroscopy of Micro- and Nanodiamonds: An Implication for Laboratory Astrophysics. *Microscopy and microanalysis : the official journal of Microscopy Society of America, Microbeam Analysis Society, Microscopical Society of Canada* **18,** 1–7 (Dec. 5, 2012).

89. Hainschwang, T., Notari, F. & Pamies, G. A Defect Study and Classification of Brown Diamonds with Deformation-Related Color. *Minerals* **10,** 903 (Oct. 12, 2020).

90. Dischler, B. *et al.* Resolved donor-acceptor pair-recombination lines in diamond luminescence. *Physical Review B* **49,** 1685–1689. https://doi.org/10.1103/PhysRevB.49.1685 (Jan. 1994).

91. Yagyu, H. *et al.* Ion implantation in CVD diamond and plasma treatment effect. *Diamond and Related Materials* **4.** Diamond Films '94, 575–579. ISSN: 0925-9635. https://www.sciencedirect.com/science/article/pii/0925963594052913 (1995).

92. J. E. Field (ed.). The Properties of Natural and Synthetic Diamond. Academic Press, London 1992. £ 90.00. ISBN 0-12-255352-7. *Crystal Research and Technology* **28,** 602–602. eprint: https://onlinelibrary.wiley.com/doi/pdf/10.1002/crat.2170280504. https://onlinelibrary.wiley.com/doi/abs/10.1002/crat.2170280504 (1993).

93. Walker, J. Optical absorption and luminescence in diamond. *Reports on progress in physics* **42,** 1605 (1979).

94. Davies, G., Lawson, S. C., Collins, A. T., Mainwood, A. & Sharp, S. J. Vacancy-related centers in diamond. *Phys. Rev. B* **46,** 13157–13170. https://link.aps.org/doi/10.1103/PhysRevB.46.13157 (20 Nov. 1992).

95. Robins, L. H., Cook, L. P., Farabaugh, E. N. & Feldman, A. Cathodoluminescence of defects in diamond films and particles grown by hot-filament chemical-vapor deposition. *Phys. Rev. B* **39,** 13367–13377 (18 June 1989).

96. Malykhin, S. *et al.* Luminescent Characteristics of Needle-Like Single Crystal Diamonds. *physica status solidi (b)* **255,** 1700189 (Jan. 2018).

97. Heiderhoff, R. *Analyse der elektronischen Eigenschaften von Diamant mittels rastermikroskopischer Methoden* PhD thesis (Verlag nicht ermittelbar, 1997).

98. Olivero, J. & Longbothum, R. Empirical fits to the Voigt line width: A brief review. *Journal of Quantitative Spectroscopy and Radiative Transfer* **17,** 233–236. ISSN: 0022-4073. https://www.sciencedirect.com/science/article/pii/0022407377901613 (1977).

99. Jahnke, K. D. *et al.* Electron–phonon processes of the silicon-vacancy centre in diamond. *New Journal of Physics* **17,** 043011. ISSN: 1367-2630 (Apr. 2015).

100. Hepp, C. *et al.* Electronic Structure of the Silicon Vacancy Color Center in Diamond. *Physical review letters* **112,** 036405 (Jan. 24, 2014).

101. Clark, C. D., Kanda, H., Kiflawi, I. & Sittas, G. Silicon defects in diamond. *Phys. Rev. B* **51,** 16681–16688. https://link.aps.org/doi/10.1103/PhysRevB.51.16681 (23 June 1995).

102. Yamamoto, T. *et al.* Extending spin coherence times of diamond qubits by high-temperature annealing. *Phys. Rev. B* **88,** 075206. https://link.aps.org/doi/10.1103/PhysRevB.88.075206 (7 Aug. 2013).

103. Gaebel, T. *et al.* Photochromism in single nitrogen-vacancy defect in diamond. *Applied Physics B* **82,** 243–246 (Feb. 2006).

104. Ishii, S. *et al.* Ensemble Negatively-Charged Nitrogen-Vacancy Centers in Type-Ib Diamond Created by High Fluence Electron Beam Irradiation. *Quantum Beam Science* **6.** ISSN: 2412-382X. https://www.mdpi.com/2412-382X/6/1/2 (2022).

105. Waldermann, F. *et al.* Creating diamond color centers for quantum optical applications. *Diamond and Related Materials* **16,** 1887–1895. ISSN: 0925-9635. https://www.sciencedirect.com/science/article/pii/S0925963507003834 (2007).

106. Grotz, B. *et al.* Charge state manipulation of qubits in diamond. *Nature Communications* **3,** 729. ISSN: 2041-1723. https://doi.org/10.1038/ncomms1729 (Mar. 2012).

107. Hong, S. *et al.* Nanoscale magnetometry with NV centers in diamond. *MRS Bulletin* **38** (Feb. 2013).

108. Neumann, P. *et al.* High-Precision Nanoscale Temperature Sensing Using Single Defects in Diamond. *Nano Letters* **13.** PMID: 23721106, 2738–2742. eprint: https://doi.org/10.1021/nl401216y. https://doi.org/10.1021/nl401216y (2013).

109. Solà-Garcia, M., Meuret, S., Coenen, T. & Polman, A. Electron-Induced State Conversion in Diamond NV Centers Measured with Pump–Probe Cathodoluminescence Spectroscopy. *ACS Photonics* **7.** PMID: 31976357, 232–240. eprint: https://doi.org/10.1021/acsphotonics.9b01463. https://doi.org/10.1021/acsphotonics.9b01463 (2020).

110. Larsson, A. & Delaney, P. The Electronic Structure of the Nitrogen-Vacancy Center in Diamond From First-Principles Theory. *Physical Review B* **77,** 165201 (Apr. 2008).

111. Storteboom, J., Dolan, P., Castelletto, S., Li, X. & Gu, M. Lifetime investigation of single nitrogen vacancy centres in nanodiamonds. *Opt. Express* **23,** 11327–11333. https://opg.optica.org/oe/abstract.cfm?URI=oe-23-9-11327 (May 2015).

112. Doherty, M. W. *et al.* The nitrogen-vacancy colour centre in diamond. *Physics Reports* **528.** The nitrogen-vacancy colour centre in diamond, 1–45. ISSN: 0370-1573. https://www.sciencedirect.com/science/article/pii/S0370157313000562 (2013).

113. Barson, M. S., Krausz, E., Manson, N. B. & Doherty, M. W. *Nanophotonics* **8,** 1985–1991. https://doi.org/10.1515/nanoph-2019-0142 (2019).

114. Fu, K.-M. C. *et al.* Observation of the Dynamic Jahn-Teller Effect in the Excited States of Nitrogen-Vacancy Centers in Diamond. *Phys. Rev. Lett.* **103,** 256404. https://link.aps.org/doi/10.1103/PhysRevLett.103.256404 (25 Dec. 2009).

115. Olver, F., Lozier, D., Boisvert, R. & Clark, C. *The NIST Handbook of Mathematical Functions* en (Cambridge University Press, New York, NY, Dec. 2010).

116. *SciPy* https://scipy.org/ (2024).

117. Barjon, J. Luminescence Spectroscopy of Bound Excitons in Diamond. *physica status solidi (a)* **214,** 1770169 (Nov. 2017).

118. Hazama, Y., Naka, N. & Stolz, H. Mass-anisotropy splitting of indirect excitons in diamond. *Physical Review B* **90,** 045209 (July 30, 2014).

119. Popov, I. V., Görne, A. L., Tchougréeff, A. L. & Dronskowski, R. Relative stability of diamond and graphite as seen through bonds and hybridizations. *Phys. Chem. Chem. Phys.* **21,** 10961–10969. http://dx.doi.org/10.1039/C8CP07592A (21 2019).

120. Sigma-Aldrich. https://www.sigmaaldrich.com/FR/fr/product/aldrich/798169 (2024).

121. Saoudi, L. *et al.* Colloidal stability over months of highly crystalline high-pressure high-temperature hydrogenated nanodiamonds in water. *Carbon* **202,** 438–449. ISSN: 0008-6223. https://www.sciencedirect.com/science/article/pii/S0008622322009058 (2023).

122. Kumar, R., Singh, D. K., Kumar, P., Kumar, R. & Dhakate, S. Influence of degree of air oxidation and functionality on ensemble emission from nitrogen vacancy centers in nano-diamonds. *Diamond and Related Materials* **97,** 107431. ISSN: 0925-9635. https://www.sciencedirect.com/science/article/pii/S0925963519301712 (2019).

123. Beha, K., Batalov, A., Manson, N. B., Bratschitsch, R. & Leitenstorfer, A. Optimum Photoluminescence Excitation and Recharging Cycle of Single Nitrogen-Vacancy Centers in Ultrapure Diamond. *Phys. Rev. Lett.* **109,** 097404. https://link.aps.org/doi/10.1103/PhysRevLett.109.097404 (9 Aug. 2012).

124. Laube, C. *et al.* Controlling the fluorescence properties of nitrogen vacancy centers in nanodiamonds. *Nanoscale* **11,** 1770–1783 (2019).

125. Bommidi, D. K. & Pickel, A. D. Temperature-dependent excited state lifetimes of nitrogen vacancy centers in individual nanodiamonds. *Applied Physics Letters* **119,** 254103. ISSN: 0003-6951. eprint: https://pubs.aip.org/aip/apl/article-pdf/doi/10.1063/5.

0072357/14555700/254103_1_online.pdf. https://doi.org/10.1063/5.0072357 (Dec. 2021).

126. Meuret, S. *et al.* Time-resolved cathodoluminescence in an ultrafast transmission electron microscope. *Applied Physics Letters* **119,** 062106. ISSN: 0003-6951. eprint: https://pubs.aip.org/aip/apl/article-pdf/doi/10.1063/5.0057861/14552605/062106_1_online.pdf. https://doi.org/10.1063/5.0057861 (Aug. 2021).

127. Takeuchi, D. *et al.* Origin of band-A emission in diamond thin films. *Physical review B* **63,** 245328 (2001).

128. Steeds, J., Davis, T., Charles, S., Hayes, J. & Butler, J. 3H luminescence in electron-irradiated diamond samples and its relationship to self-interstitials. *Diamond and Related Materials* **8,** 1847–1852. ISSN: 0925-9635. https://www.sciencedirect.com/science/article/pii/S0925963599001442 (1999).

129. Plakhotnik, T., Doherty, M. W. & Manson, N. B. Electron-phonon processes of the nitrogen-vacancy center in diamond. *Phys. Rev. B* **92,** 081203. https://link.aps.org/doi/10.1103/PhysRevB.92.081203 (8 Aug. 2015).

130. Kane, E. O. Phonon spectra of diamond and zinc-blende semiconductors. *Phys. Rev. B* **31,** 7865–7876. https://link.aps.org/doi/10.1103/PhysRevB.31.7865 (12 June 1985).

131. Pedroza-Montero, F. A., Santacruz-Gomez, K. J., Meléndrez-Amavizca, R. & Barboza-Flores, M. Commercial nanodiamonds for precise fluorescence-based temperature sensing. *Applied Physics Letters* **125,** 073701. ISSN: 0003-6951. eprint: https://pubs.aip.org/aip/apl/article-pdf/doi/10.1063/5.0219532/20108534/073701_1_5.0219532.pdf. https://doi.org/10.1063/5.0219532 (Aug. 2024).

132. *Thorlabs: Hard-Coated Edgepass Filters* https://www.thorlabs.com/newgrouppage9.cfm?objectgroup_id=6082&pn=FELH0550 (2025).

133. Meuret, S. *Intensity interferometry experiments in a scanning transmission electron microscope : physics and applications* 2015SACLS112. PhD thesis (Université Paris-Saclay, 2015). http://www.theses.fr/2015SACLS112/document.

134. Liang, Y., Ozawa, M. & Krueger, A. A General Procedure to Functionalize Agglomerating Nanoparticles Demonstrated on Nanodiamond. *ACS Nano* **3.** PMID: 19601635, 2288–2296. eprint: https : / / doi . org / 10 . 1021 / nn900339s. https://doi.org/10.1021/nn900339s (2009).

135. Mui, D. S. L., Lenz, E. H., Cyterski, C., Venkataraman, K. & Kawaguchi, M. Wafer Surface Charging Model for Single-Wafer Wet-Spin Processes. *IEEE Transactions on Semiconductor Manufacturing* **24,** 552–558 (2011).

136. Shibata, H. *et al.* High Thermal Conductivity of Gallium Nitride (GaN) Crystals Grown by HVPE Process. *MATERIALS TRANSACTIONS* **48,** 2782–2786 (2007).

137. Strenaer, R., Guhel, Y., Gaquière, C. & Boudart, B. Time-resolved self-heating temperature measurements of AlInN/GaN HEMTs using CeO2 Raman micro-thermometers. *Microelectronics Reliability* **150.** Special issue of 34th European Symposium on Reliability of Electron Devices, Failure Physics and Analysis, ESREF 2023, 115156. ISSN: 0026-2714. https://www.sciencedirect.com/science/article/pii/S0026271423002561 (2023).

138. Finas, M., Girard, H. A. & Arnault, J.-C. How to efficiently isolate multiple size ranges of oxidized or hydrogenated milled nanodiamonds. *Nanoscale Adv.* **6,** 5375–5387. http://dx.doi.org/10.1039/D4NA00487F (21 2024).

139. Klauser, F. *et al.* Comparison of different oxidation techniques on single-crystal and nanocrystalline diamond surfaces. *Diamond and Related Materials* **19.** Proceedings of Diamond 2009, The 20th European Conference on Diamond, Diamond-Like Materials, Carbon Nanotubes and Nitrides, Part 1, 474–478. ISSN: 0925-9635. https://www.sciencedirect.com/science/article/pii/S092596350900329X (2010).